UNIVERSITY OF OKLAHOMA

GRADUATE COLLEGE

MULTIPLE-POROSITY AND MULTIPLE-PERMEABILITY POROELASTICITY

A DISSERTATION

SUBMITTED TO THE GRADUATE FACULTY

in partial fulfillment of the requirements for the

Degree of

DOCTOR OF PHILOSOPHY

By

AMIN MEHRABIAN
Norman, Oklahoma
2013

MULTIPLE-POROSITY AND MULTIPLE-PERMEABILITY POROELASTICITY

A DISSERTATION APPROVED FOR THE
MEWBOURNE SCHOOL OF PETROLEUM AND GEOLOGICAL ENGINEERING

BY

_____
Dr. Younane Abousleiman, Chair

_____
Dr. Gerald Miller

_____
Dr. Yucel Akkutlu

_____
Dr. Maysam Pournik

_____
Dr. Ahmad Jamili

Dedicated to:

Milka Todorova Bekova

Acknowledgements

I express my deep gratitude to Dr. Younane N. Abousleiman. His support, patience, sympathy and passionate supervision over the course of my PhD career, which at times went beyond the norms of duty, will keep my depts to him everlasting.

Dr. Gerald Miller, Dr. Yucel Akkutlu, Dr. Maysam Pournik, and Dr. Ahmad Jamili are gratefully acknowledged for serving on my advisory committee.

I wish to thank my colleagues for providing me with a professional and friendly environment at *integrated* PoroMechanics Institute.

Table of Contents

List of Tables

List of Figures

Abstract

Since the advent of basic ideas in the theory of fluid seepage in fissured porous media, much effort has been placed in engineering and science departments of various disciplines in trying to foster the concept of dual-porosity continua. In keeping with these efforts, this dissertation aims to extend the existing theories of single and dual-porosity, fluid saturated, homogenous, isotropic and linearly elastic materials to account for higher levels of pore structure complexity, namely the multiple-porosity and multiple-permeability poroelasticity.

An illustrative and inductive methodology is taken in presenting the natural extensions from fundamental concepts associated with constitutive modeling of dual-porosity materials to this new case. However, deductive proof and reasoning is provided when derivation of terms and equations was required. In particular, a closure to the problem of material property coefficients of a multiple-porosity mixture, whose constituents follow Biot's formulations of stress-strain relation, is presented. Results are compared and validated with related documentations on the topic for dual-porosity mixtures, while possible variations are thoroughly discussed and rationalized.

A Complete and integrated analytical solution to a class of generalized plane-strain multiple-poroelastic problems featuring rectangular, cylindrical or spherical geometries is developed. Again, this solution is compared and validated with currently published solutions of its dual-porosity counterparts. Results indicate that the problem's time scales, and consequently, the associated coupled phenomenon –

known as the *Mandel-Cryer effect* in poromechanics literature – would proliferate when the number of distinct porosity networks in the analytical model is increased.

Further along this dissertation, field applications of these solutions, according to a number of related petroleum-industry problems are presented. Variations of the multiple-porosity/multiple-permeability Cryer's and axisymmetric Mandel's problems are developed to account for additional boundary conditions due to an inner concentric cavity within their geometry. The former solution applies to investigation of sealing capacity and integrity of caprocks during CO_2 geo-sequestration operations, while the latter is used to derive formulas for compaction (porosity reduction) and transient analysis of depleting multiple-porosity/multiple-permeability reservoirs.

Findings indicate that neglecting or over-simplifying the complex effect of distinguishable pore structures within the rock matrix, such as fractures and vugs, might produce errors which often tend to underestimate either flow or deformation aspects of its response to application of external stresses or pore pressure. In some other cases, however, the results suggest that proper and consistent selection of effective properties of *lumped-porosity models* can return practically accurate results.

This dissertation is the first comprehensive documentation on the theory of multiple-porosity and multiple-permeability poroelasticity. It certainly holds a number of simplifying assumptions which include but are not limited to the model's homogeneity and isotropy, linearity of constitutive relations, as well as constraints on the ongoing physical exchange phenomena within its porous structure. Relaxing any of

these restrictive assumptions would indeed bring about an entirely new area of research and study on the topic.

Chapter 1: Introduction

Compressibility, in its general definition, is identified with the ratio of a fractional volume change with respect to a pressure change (Wang 2000). In case of porous fluid saturated materials, it can be the bulk, pore, fluid or solid grain volume. Alternatively, the pressure or stress can be due to either the pore fluid perturbations *p* or variation in confining stress p_c. Figure 1 shows schematic illustration of these compressibilities, along with relations, which identify the volumetric deformations of solid skeleton and pore fluid of a porous mixture, as functions of variations in the pore pressure and/or confining stress.

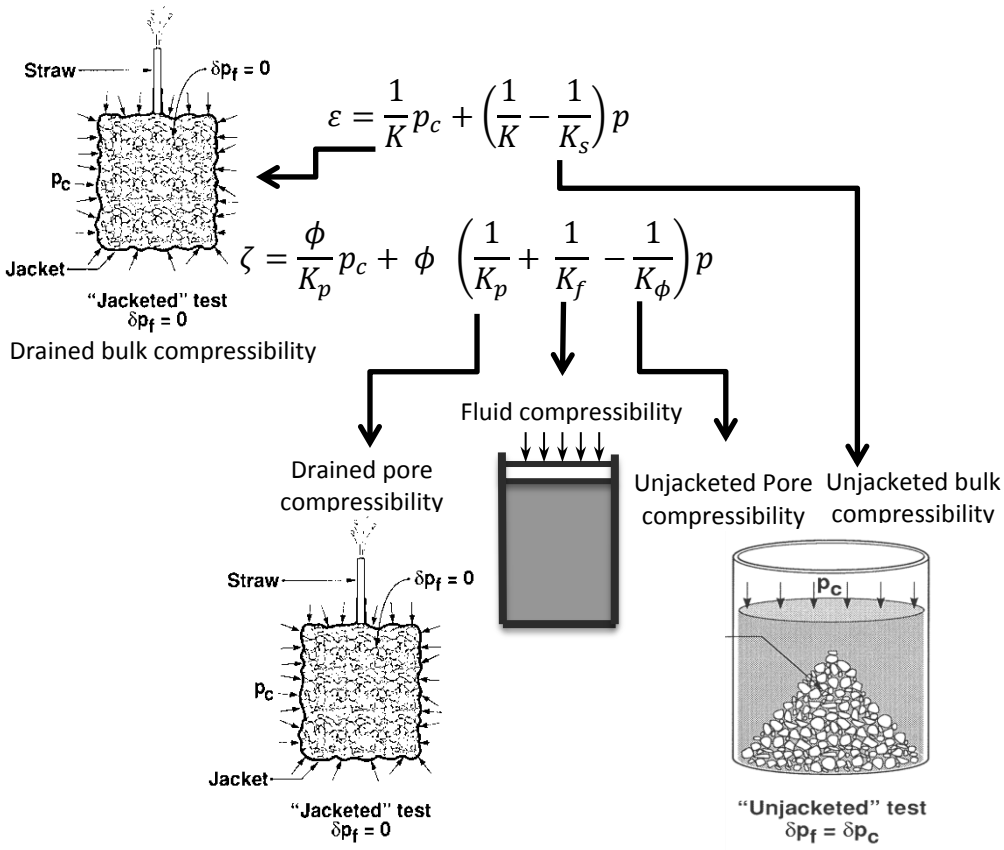

Figure 1. Schematic illustration of various compressibilities, relating the volumetric deformations of solid matrix and pore fluid to perturbations in pore pressure and/or confining stress. Part of this figure is adopted from Berryman (2006).

1.1. Introduction to poromechanics

> "Consider a small cubic element of the consolidating soil, its sides being parallel with coordinate axes. This element is taken to be large enough compared to the size of the pores so that it may be treated as homogenous, and at the same time small enough, compared to the scale of the macroscopic phenomena in which we are interested, so that it may be considered as infinitesimal in mathematical treatment" (Maurice A. Biot, Feb 1941, Journal of Applied Physics)

The above paragraph rewrites Biot's description of a porous medium's Representative Elementary Volume (REV), in establishing what nowadays is known as poroelasticity theory. This theory (Biot 1941, 1955) manifests the volumetric deformations of a porous, fluid saturated, linearly elastic, homogenous, and isotropic medium (see Figure 2) through 3 independent material properties. The corresponding constitutive relations can be written in terms of drained matrix bulk modulus $\bar{K}$, Skempton's (1954) pore pressure coefficient $\bar{B}$, and Biot-Willis (1957) coefficient $\bar{\alpha}$ as follows:

$$\begin{pmatrix} \varepsilon \\ \zeta \end{pmatrix} = \frac{1}{K}\begin{pmatrix} 1 & \bar{\alpha} \\ \bar{\alpha} & \bar{\alpha}/\bar{B} \end{pmatrix}\begin{pmatrix} \sigma \\ p \end{pmatrix} \tag{1-1}$$

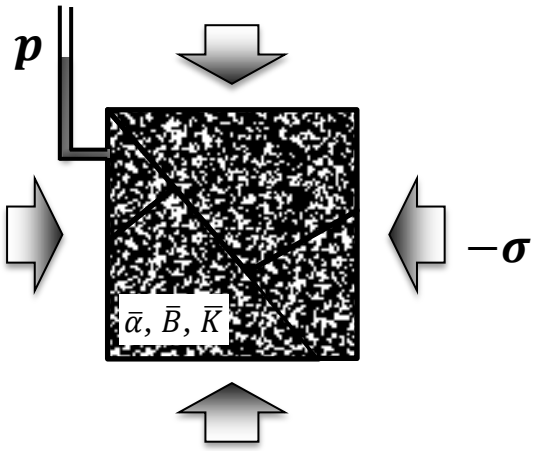

Figure 2. Schematic of a porous, fluid saturated homogenous isotropic and linearly elastic material element with illustration of confining stress σ and pore pressure p.

where $\sigma = {\sigma_{kk}}/{3}$ and p stand for the average normal stress (tensile positive) and the excess pore pressure, and ε and ζ denote the volumetric strain (Positive in expansion) and increment of fluid content (positive when fluid added to porous space), respectively[1].

Equation (1-1) characterizes a *Gassmann material* (Berryman 1999, 2002). A key implication in identifying a substance as such is that any development of shear stress or deformation within its matrix would be independent of the saturating fluid pressure, content or properties.

1.2. Dual-porosity/dual-permeability poroelasticity

Since the advent of basic concepts in the theory of fluid seepage in fissured rocks (Barenblatt *et al*. 1960; Warren & Root 1963; Aifantis 1980), much effort has been made in engineering and science departments of various disciplines in trying to foster the concept of dual-porosity continua. In keeping with these efforts, extensions of Biot's theory to dual-porosity and dual-permeability poroelasticity of isotropic (Elsworth & Bai 1992; Berryman 2002a; Nguyen and Abousleiman 2010) or anisotropic materials (Nguyen 2010), have been the focus of studies which attempt to treat the fully-coupled fluid flow and deformation processes in porous media.

A class of related studies deals with the problem of dual-porosity material characterization. The series of publications by Berryman and his associates within late 1990s and early 2000s, present models for finding the mechanical properties of dual-porosity mixtures (Berryman & Wang 1995; Berryman & Berge 1996; Berryman & Pride

[1] Unless otherwise specified, the above-mentioned sign conventions for stress and strain will be consistently followed throughout this dissertation.

1998, 2002). On the basis of these models, expressions for *effective mechanical properties* of such dual-continua in terms of the *intrinsic properties* of their constituents were derived (Berryman 2002). Berryman's postulate for characterizing dual-porosity poroelastic materials incorporates a natural extension of Equation (1-1) as follows:

$$\begin{pmatrix} \varepsilon \\ \zeta_1 \\ \zeta_2 \end{pmatrix} = \begin{pmatrix} a_{11} & a_{12} & a_{13} \\ a_{21} & a_{22} & a_{23} \\ a_{31} & a_{32} & a_{33} \end{pmatrix} \cdot \begin{pmatrix} \sigma \\ p_1 \\ p_2 \end{pmatrix} \tag{1-2}$$

This postulate inherits the assumption that both the mixture and its constituents would behave as Gassmann materials, rendering two distinct pore pressures p_1 , p_2 corresponding to the two co-existing porosity networks, as shown in Figure 3.

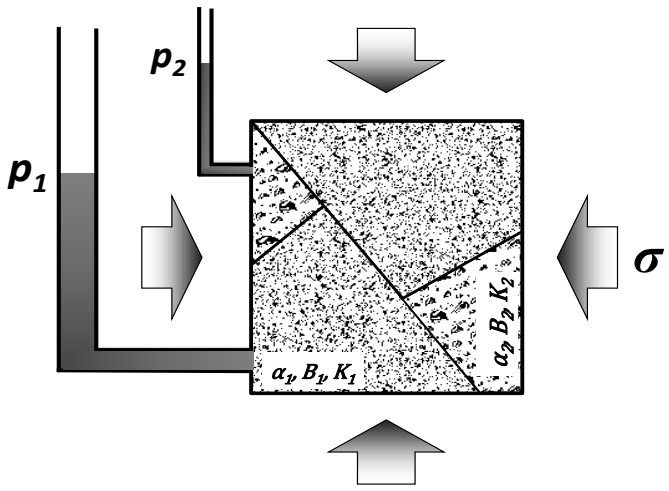

Figure 3. Schematic of the double-porosity model at microscopic level, with external confining pressure σ and distinct instantaneous pore pressures p_1, p_2. It should be noted that despite its seemingly non-homogenous demonstration, any REV of this model would be a homogenous double-porosity continuum, comprising the properties of both porous networks. This principle is consistent with Biot's original statement on the scales of investigation within the framework of poroelasticity theory.

When combined with the associated dual-permeability and inter-porosity fluid exchange effects, the dual-porosity poroelastic model is capable of handling certain applied poromechanics problems. Using the dual-porosity/dual-permeability model, a time-dependent analytical solution to the wellbore stress of fractured fluid-saturated rock formations is successfully developed by Abousleiman and Nguyen (2005). Their solution stems from an earlier heuristic methodology taken by Cui, Abousleiman and Cheng (1997), in which the general state of far-field stresses is decomposed into its components in a *well-aligned* coordinate system, in such a way that each sub-problem can be regarded as a generalized plane strain condition. Their dual-porosity/dual-permeability model of a naturally fractured rock, along with illustrations of the wellbore geometry and the far-field stress condition, is presented in Figure 4.

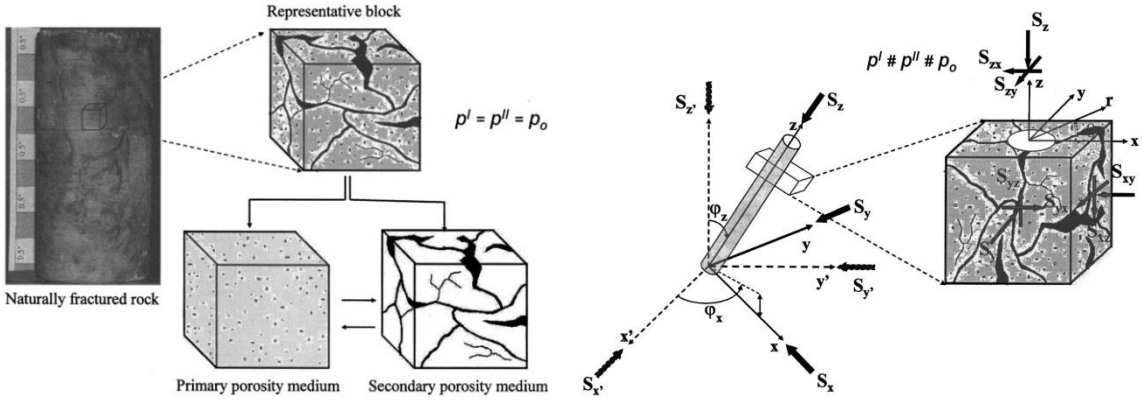

Figure 4. (a) Representation of dual-porosity/dual-permeability model. (b) Geometry of an inclined wellbore with respect to 3D state of far field stresses. Copy from Abousleiman and Nguyen 2005.

1.3. Multiple-porosity poroelasticity

Despite its elegant and natural approach in extending Biot's theory to account for two distinct pore structures in an elastic medium, the dual-porosity/dual-permeability model may fall short in capturing some crucial aspects of flow and/or deformation in many fluid saturated porous materials.

Naturally fractured shale reservoirs, for instance, have often been analyzed using dual-porosity models, comprising the shale matrix with high porosity and low permeability, and a fracture network with low total porosity and high permeability (Carlson & Mercer 1991; Ozkan *et al*. 2010). High rates of production at some shale reservoirs indicate that a significant amount of the produced hydrocarbon comes from the shale matrix. The matrix permeability, however, is too low to justify the transfer of observed amount of hydrocarbon to fracture networks based on dual-porosity models. A number of hypotheses have been proposed in trying to explain the unexpectedly high rates of gas transfer from shale matrix to macro-fracture networks, such as Knudson diffusion and slip flow of shale nano-pores (Civan *et al*. 2011) or the existence of highly permeable organic flakes and natural micro-fractures (Wang 2009). These efforts have recently led to the emergence of triple (Wang 2009; Dehghanpour & Shirdel 2011) and quad-porosity shale models (Hudson et al. 2012), supposedly enhancing the accuracy of their dual-porosity counterparts by increasing the assumed number of distinct porosity networks within the shale matrix.

Applications of multiple-porosity/multiple-permeability models do not restrict to earth sciences. Biomaterials such as bone and brain tissues are also well-known for

their multiple pore structure. For example, *Russian doll poroelasticity* (Gailani & Cowin 2009) and *Hierarchial poroelasticity* (Cowin *et al*. 2009) are general terms attributed to the specific models that these investigators conceived for the interstitial fluid exchange between vascular and lacunar–canalicular porosities of bone tissues. On the basis of such models, which in effect, classify the mechanical interaction and fluid transport between smaller and larger size porosity levels, Benella *et al*. 2012 developed solutions for hollow poroelastic cylinders under cyclic loadings. These solutions were later used for interpretation of cyclic and ramp loading experiments on bone samples of same geometry, in order to estimate the permeability of the above-mentioned porosity networks.

Brain tissue is also known to feature a multiple-pore structure. *Multiple-Network Poroelasticity Theory* (MPET) is the term used by Tully *et al*. (2011) and Vardakis *et al.* (2013), for a model which describes complexities associated with the brain tissue's mechanical deformation, arising from fluid transport and exchange through four porosity networks. These networks comprise the extracellular space (matrix), as well as three distinct porosities related to arteries, veins and capillary blood vessels within the brain, as shown in Figure 5.

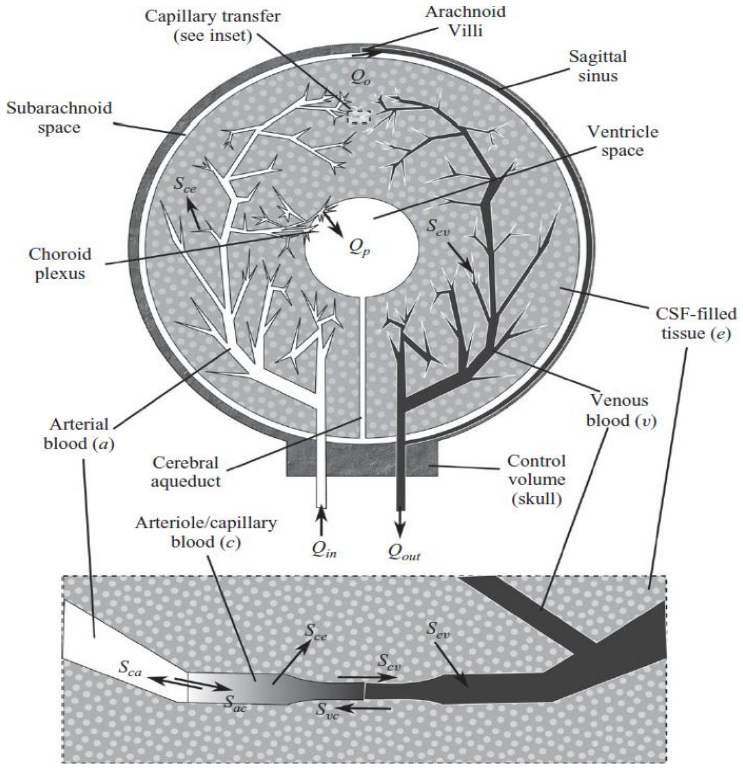

Figure 5. A four-network MPET description of the brain (copy from Tully et al. 2011): Directional transfer can occur from the arteriole/capillary network to the CSF and venous networks and from the CSF to the venous network. Flow is prohibited between the CSF and arterial network, or directionally from the venous network to the CSF or arteriole/capillary networks.

Figure 6 presents schematics of a material element comprising *N* distinct porous networks. It can be considered as a natural extension to dual-porosity/dual-permeability illustrations in Figure 3. An external confining pressure σ would generate *N* distinct instantaneous pore pressures $p_1, p_2, \ldots, p_N$ within such a material. Following Berryman's postulate for characterizing dual-porosity poroelastic materials, a generalized form of Equation (1-2) can be written as:

$$\begin{pmatrix} \varepsilon \\ \zeta_1 \\ \vdots \\ \zeta_N \end{pmatrix} = \begin{pmatrix} a_{11} & \cdots & a_{1(N+1)} \\ \vdots & \ddots & \vdots \\ a_{(N+1)1} & \cdots & a_{(N+1)(N+1)} \end{pmatrix} \cdot \begin{pmatrix} \sigma \\ p_1 \\ \vdots \\ p_N \end{pmatrix} \tag{1-3}$$

Investigation of the properties a_{ij} and coupled flow/deformation processes of a material characterized by Equation (1-3) is the subject matter of this dissertation.

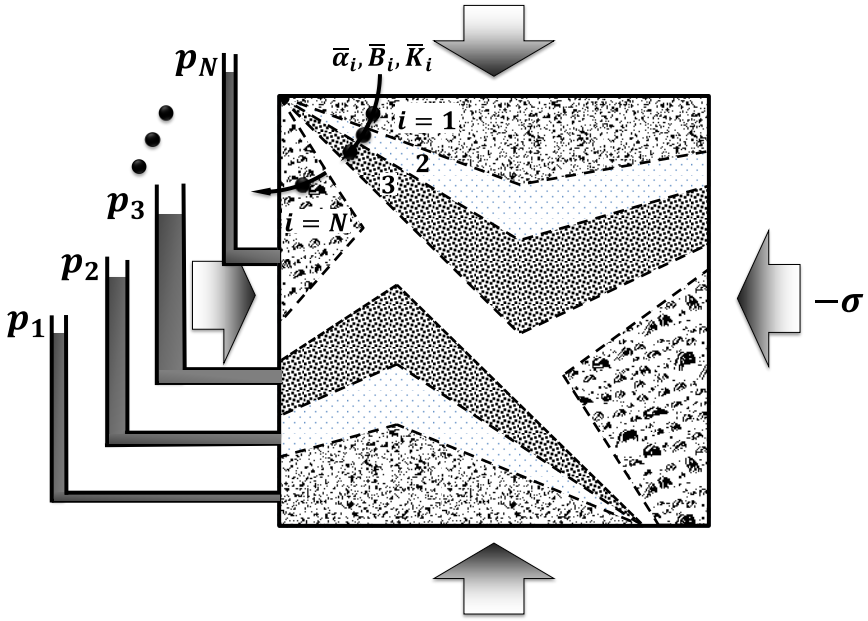

Figure 6. Schematics of the multiple-porosity model at microscopic level, with external confining pressure σ and *N* distinct instantaneous pore pressures $p_1, p_2, \dots, p_N$. It should be noted that, here, the scale of investigation is consistent with poroelasticity of single and dual-porosity continua. Therefore, despite its seemingly non-homogenous demonstration, any REV of this model is a homogenous multiple-porosity continuum, comprising all considered porous networks.

1.4 Fundamental consolidation-type problems of two-dimensional poroelasticity

Abundance of research on the mechanics of dual-porosity/dual-permeability materials provides the engineering and research communities with very little number of analytical solutions to the associated applied problems. The record becomes even smaller when it comes to multiple-porosity/multiple permeability models, and in fact to the author's knowledge, there is no documentation on this subject in literature. Nevertheless, analytical dual-porosity/dual-permeability solutions of fundamental

poromechanics problems, such as consolidation of a rectangular strip - known as Mandel's problem in poromechanics literature - are developed (Nguyen & Abousleiman 2010). In the same publication, a Mandel-type problem corresponding to consolidation of a cylindrical disk was addressed and solved. Later, Nguyen (2010) developed solutions for dual-porosity/dual-permeability of hollow cylinders. These solutions can be used as benchmarks for solutions to the corresponding multiple-porosity/multiple permeability poroelastic media which are developed in this study. Table 1-1 presents a list of fundamental two-dimensional and transient problems in poromechanics.

Table 1. Two-dimensional (Quasi-1D) transient problems of poromechanics.

Problem	Geometry	Existing Analytical Solutions		
		Porosity Level		
		Single	**Double**	**multiple**
Mandel	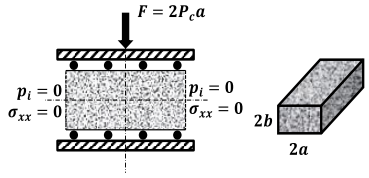	Mandel, 1955 Abousleiman *et al*. 1996a Hoang & Abousleiman. 2009	Nguyen & Abousleiman, 2010	This study Chapter 3
Axi-Symmetric Mandel	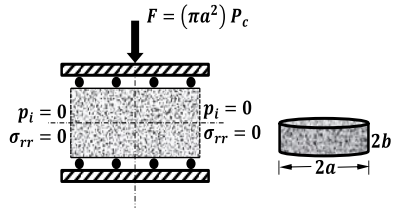	Abousleiman & Cui, 1998	Nguyen & Abousleiman, 2010	This study Chapter 3
Hollow Cylinder	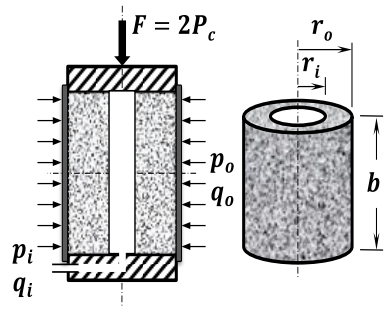	Abousleiman & Kanj, 2004 Kanj & Abousleiman, 2004 Huang *et al*. 2001 Cowin *et al*. 2009	Nguyen, 2010	This study Appendix D
Cryer	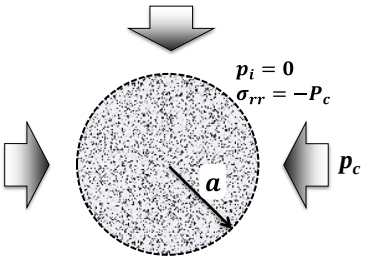	Cryer, 1963	This study	This study Chapter 3
Hollow Sphere	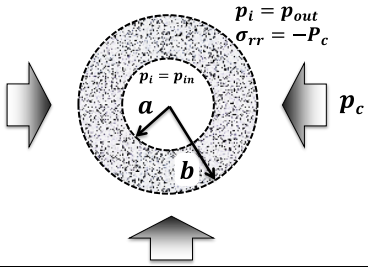	Nowinski & Davis, 1970 (non-symmetric case) Mehrabian & Abousleiman, 2009	This study Appendix C	NA

1.4. Objectives and overview

This dissertation aims to improve the existing theory of dual-porosity, fluid saturated and isotropic elastic materials to account for higher levels of pore structure complexity, namely the *multiple-porosity/multiple-permeability poroelasticity*. Induction is the overall approach taken in extension of fundamental concepts associated with the dual-porosity poroelastic theory to this new case. However, deductive proof and reasoning is provided in cases where derivation of terms and equations were required.

Consistent and complete mechanical characterization of multiple-porosity mixtures is still an open problem in poromechanics society (Berryman 2002). Chapter 2 addresses this problem within the framework of poroelasticity theory. For this purpose, constitutive relations corresponding to individual constituents, as well as the whole mixture are written. A series of *thought experiments* are designed in order to find the mixture's mechanical properties a_{ij} as functions of $\bar{\alpha}_i, \bar{B}_i, \bar{K}_i$, corresponding to its constituents properties (Figure 7).

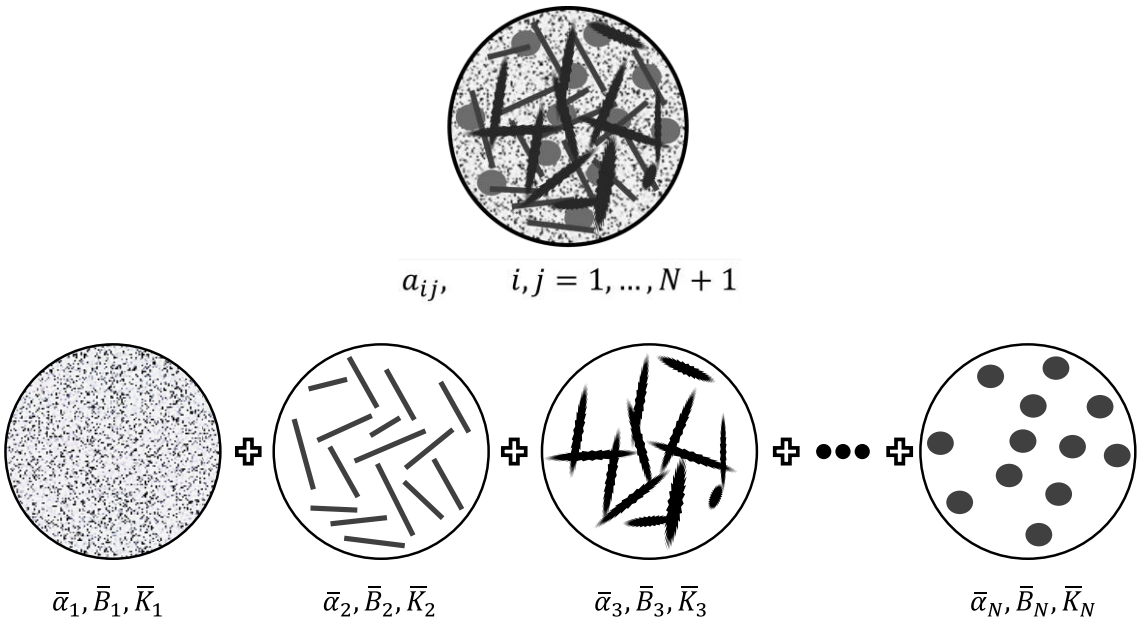

Figure 7. *N* poroelastic constituents characterized by $\bar{\alpha}_i, \bar{B}_i, \bar{K}_i$ comprising an N-porosity poroelastic mixture with mechanical properties a_{ij}.

When combined with the associated multiple-permeability and inter-porosity fluid exchange effects, the multiple-porosity poroelastic model is capable of handling certain applied poromechanics problems. Chapter 3 presents an illustrative step-by-step methodology based on physical intuition, which derives the multiple-porosity/multi-permeability constitutive relations. Owing to their generality and broad applications, the two-dimensional and transient problems listed in Table 1, are thoroughly investigated throughout this dissertation. A generalized analytical solution to the class of these problems is developed further along Chapter 3. An integrated methodology is taken for this purpose, so that the solutions corresponding to each geometry (i.e. rectangular, axisymmetric or spherical) can be extracted from the presented general solution by simple permutation of their corresponding Sturm-Liouville functions.

Field applications of the above-mentioned solutions are the subject matter of Chapter 4. Variations of the multiple-porosity/multiple-permeability Cryer's and axisymmetric Mandel's problems are developed to account for additional boundary conditions due to an inner concentric hollow space within their geometry. The former solution applies to investigation of the sealing capacity and integrity of caprocks during CO_2 geo-sequestration operations, while the latter is used to derive formulas for compaction (porosity reduction) and transient pressure analysis of multiple-porosity depleting reservoirs.

To the author's knowledge, this dissertation is the first comprehensive documentation on the theory of multiple-porosity and multiple-permeability poroelasticity. While drawing a number of concluding remarks, chapter 5 presents a broader perspective to this theory by highlighting the restrictive assumptions which have been taken in development of the related models and solutions. These assumptions include but are not limited to the model's homogeneity, isotropy and linearity of constitutive relations, as well as the number of ongoing exchange phenomena within its porous texture. Relaxing any of these constraints would indeed bring about an entirely new area of research and study on the topic.

Chapter 2: Multiple-Porosity Poroelasticity

Following the rationale for dual-porosity theory presented in chapter 1, a multiple-porosity fluid saturated porous medium is considered to comprise *N* distinct porous continuum networks, with a porous matrix of specific volume $v_1 = {}^{V_1}/_{V}$ and intrinsic material properties $\overline{K}_1, \bar{B}_1, \bar{\alpha}_1$, as well as (*N*-1) additional porous constituents embedded within the matrix, having volume fractions $v_i = {}^{V_i}/_{V}$ and intrinsic material properties $\overline{K}_i, \bar{B}_i, \bar{\alpha}_i$. A natural extension from Equation (1-2) to such a linearly elastic multiple-porosity material can be written as follows:

$$\begin{pmatrix} \varepsilon \\ \zeta_1 \\ \vdots \\ \zeta_N \end{pmatrix} = \begin{pmatrix} a_{11} & \cdots & a_{1(N+1)} \\ \vdots & \ddots & \vdots \\ a_{N1} & \cdots & a_{N(N+1)} \end{pmatrix} \cdot \begin{pmatrix} \sigma \\ p_1 \\ \vdots \\ p_N \end{pmatrix} \tag{2-1}$$

where σ and ε stand for the total normal stress (tensile positive) and the volumetric strain (positive in expansion), and p_i, ζ_i respectively denote the excess pore pressures and increment of fluid content (positive when fluid added to porous space) in pore space of the i^{th} porosity network. Since we are considering linear poroelasticity, a thermodynamic energy density property $U = \frac{1}{2}(\sigma_{kk}\varepsilon + \sum_{i=1}^{N} p_i\zeta_i)$ can be defined for this material. The continuity of mixed second partial derivatives of U requires the coefficient matrix in Equation (2-1) to be symmetric i.e. $a_{ij} = a_{ij}$. Thus, in order to characterize an *N*-porosity linear poroelastic continuum, only $\frac{(N+1)(N+2)}{2}$ independent coefficients a_{ij} are required to be determined from the intrinsic properties attributed

to the individual networks. Following some simple linear algebra, equation (2-1) can be rewritten in the following form:

$$\begin{pmatrix} \sigma \\ \zeta_1 \\ \vdots \\ \zeta_N \end{pmatrix} = \begin{pmatrix} K & -\alpha_1 & \dots & -\alpha_N \\ \alpha_1 & \frac{1}{M_{11}} & \cdots & \frac{1}{M_{1N}} \\ \vdots & \vdots & \ddots & \vdots \\ \alpha_N & \frac{1}{M_{1N}} & \cdots & \frac{1}{M_{NN}} \end{pmatrix} \cdot \begin{pmatrix} \varepsilon \\ p_1 \\ \vdots \\ p_N \end{pmatrix} \tag{2-2}$$

with a more familiar coefficient matrix, whose elements are functions of a_{ij} in equation (2-1), as follows:

$$\begin{pmatrix} \sigma \\ \zeta_1 \\ \vdots \\ \zeta_N \end{pmatrix} =$$

$$\frac{1}{a_{11}} \begin{pmatrix} 1 & a_{12} & \dots & a_{1N} \\ -a_{12} & -{a_{12}}^2 + a_{11}a_{22} & \cdots & -a_{12}a_{1N} + a_{11}a_{25} \\ \vdots & \vdots & \ddots & \vdots \\ -a_{1N} & -a_{12}a_{1N} + a_{11}a_{22} & \cdots & -a_{12}a_{1N} + a_{11}a_{(N+1)(N+1)} \end{pmatrix} \cdot \tag{2-3}$$

$$\begin{pmatrix} \varepsilon \\ p_1 \\ \vdots \\ p_N \end{pmatrix}$$

The total N parameters α_{1i} appearing in the first row of the coefficient matrix in Equation (2-3) are defined as the effective Biot-Willis coefficients of primary and secondary porosities in the mixture. M_1 to M_1 are the corresponding effective Biot's Moduli, while the effect of excess pore pressure of one network on the fluid content increment of the other is represented by inter-porosity modulus M_{ij}. We notice that Equation (2-2) defines the *effective* properties of a multi-porosity substance (e.g. α_i, M_{ij}), as opposed to the intrinsic property $\bar{\alpha}_i, \overline{M}_{ij}$.

The objective of this chapter is to investigate the possibility of finding effective material properties a_{ij} of a multiple-porosity poroelastic mixture from the intrinsic properties of its porous components, $\overline{K}_i, \bar{B}_i, \bar{\alpha}_i$. This objective inherently incorporates the assumption that the individual components are *Gassmann materials*, That is to say, the response of each poroelastic component to deformation follows Equation (1-1) as rewritten below :

$$\begin{pmatrix} \varepsilon_i \\ \zeta_i \end{pmatrix} = \frac{1}{\overline{K}} \begin{pmatrix} 1 & \bar{\alpha}_i \\ \bar{\alpha}_i & \bar{\alpha}_i / \bar{B}_i \end{pmatrix} \begin{pmatrix} \sigma_i \\ p_i \end{pmatrix}, \quad i = 1, \dots, N \tag{2-4}$$

The effective material properties a_{ij}, however, seem to be functions of not only the intrinsic properties of the components, but also the type of joints which bond these porous components together. On the basis of a *self-similar expansion* thought experiment, Berryman (2002) derived expressions for a_{ij} in terms of intrinsic properties $\overline{K}_i, \bar{B}_i, \bar{\alpha}_i$ $(i = 1,2)$ of a dual-porosity mixture. Here, we re-examine Berryman's methods for dual-porosity materials, and will extend the analysis to the multiple-porosity case.

2.1. Properties Coefficients of Dual-Porosity Material

Figure 8 shows the schematic of a dual-porosity matrix undergoing some *thought experiment* which incorporates adjustments of the external confining pressure σ and the two pore pressures p_1 and p_2, as well as the combinations of opening or closure of drainage vents w_1 and w_2. Also, a selection of the dashed red lines or solid black lines respectively implies pervious or impervious boundaries at the interface of the two components at the micromechanics level of investigation.

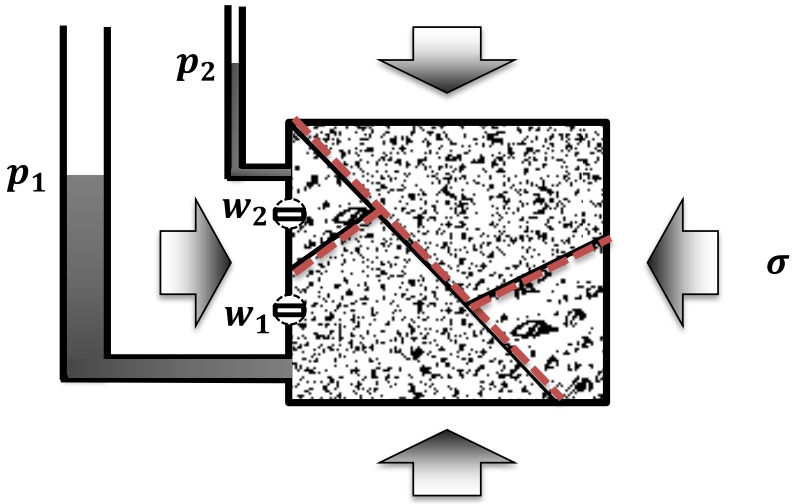

Figure 8. Schematics of the dual-porosity model at microscopic level, with illustrations of the two imaginary vents w_1 and w_2 along with the pervious (dashed red) or impervious (solid black) boundaries between the porous constituents.

The classical undrained compression test, for instance, can be obtained by setting $p_1 = p_2 = p$ and $\sigma \neq 0$ when both vents w_1 , w_2 are closed and the boundaries of the constituents are pervious. The schematic of this experiment in accord with definitions introduced with Figure 8 is illustrated in Figure 9.

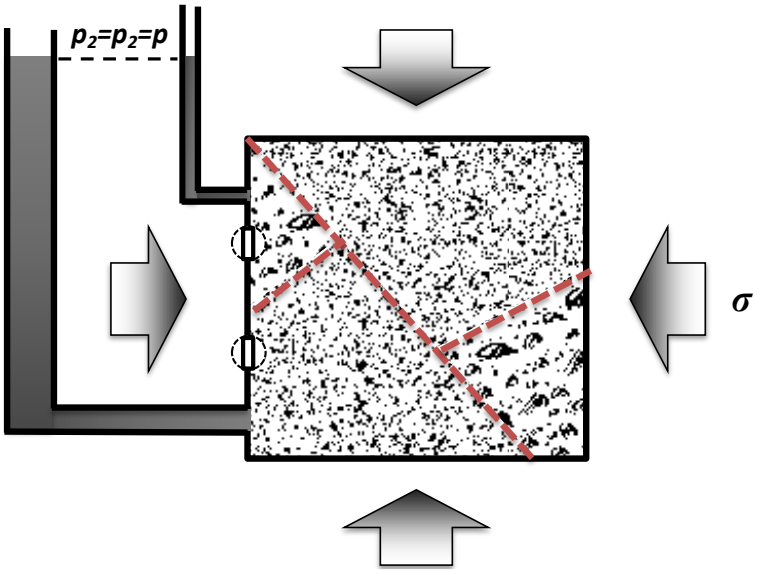

Figure 9. Schematics of the undrained confining test.

From Equations (2-1) and (2-4), a system of algebraic equations can be written for a thought experiment, between material property coefficients of constituents (1) and (2), as well as the whole matrix. Some of the variables in these equations might be considered as input (e.g. σ in the undrained test). The rest might be unknowns which together with $\frac{(N+1)(N+2)}{2} = 6$ coefficients a_{ij} are to be determined by derived algebraic equations. Table 2 lists some of these experiments, along with their corresponding equations.

Table 2. The thought experiments of dual-porosity matrix.

Test	Input parameters	Equations
Drained Confining	$\sigma \neq 0$ $p_1=p_2=0$ w_1, w_2 *open*	Constituents: $\epsilon_i = -\frac{1}{K_i}\sigma_i\,,\ \ i=1,2$ $\zeta_i = -\frac{\alpha_i}{K_i}\sigma_i\,,\ \ i=1,2$ Matrix: $\epsilon = -a_{11}\cdot\sigma$ $v_1\zeta_1 = a_{12}\cdot\sigma$ $v_2\zeta_2 = a_{13}\cdot\sigma$ Compatibility $v_1\epsilon_1 + v_2\epsilon_2 = \epsilon$
Long-time Undrained Confining (Pervious inter-porosity interface)	$\sigma \neq 0$ $p_1=p_2=p$ w_1, w_2 *Closed*	Constituents: $\epsilon_i = -\frac{1}{K_i}\sigma_i - \frac{\alpha_i}{K_i}p,\ \ i=1,2$ $\zeta_i = -\frac{\alpha_i}{K_i}\sigma_i + \frac{\alpha_i}{K_iB_i}p\,,\ \ i=1,2$ Matrix: $\epsilon = a_{11}\cdot\sigma - (a_{12}+a_{12})\,p$ $v_1\zeta_1 = a_{12}\cdot\sigma + (a_{22}+a_{23})\,p$ $v_2\zeta_2 = a_{13}\cdot\sigma + (a_{23}+a_{33})\,p$ Compatibility $\epsilon = v_1\epsilon_1 + v_2\epsilon_2$ $\zeta = v_1\zeta_1 + v_2\zeta_2 = 0$
Instantaneous Undrained confining (Impervious inter-porosity interface)	$\sigma \neq 0$ $p_1 \neq p_2$ $\zeta_1 = \zeta_1 = 0$ w_1, w_2 *Closed*	Constituents: $\epsilon_i = -\frac{1}{K_i}\sigma_i - \frac{\alpha_i}{K_i}p_i,\ \ i=1,2$ $0 = -\frac{\alpha_i}{K_i}\sigma_i + \frac{\alpha_i}{K_iB_i}p\,,\ \ i=1,2$ Matrix: $\epsilon = a_{11}\cdot\sigma - a_{12}\,p_1 - a_{13}p_2$ $v_1\zeta_1 = a_{12}\cdot\sigma + a_{22}\,p_1 + a_{23}p_2$ $v_2\zeta_2 = a_{13}\cdot\sigma + a_{23}\,p_1 + a_{33}p_2$ Compatibility $\epsilon = v_1\epsilon_1 + v_2\epsilon_2$
Unconfined pressure and fluid injection in both constituent with impervious boundary	$\sigma \neq 0$ $p_1 \neq p_2 \neq 0$ w_1, w_2 *Closed*	Constituents: $\epsilon_i = -\frac{1}{K_i}\sigma_i - \frac{\alpha_i}{K_i}p_i,\ \ i=1,2$ $\zeta_i = -\frac{\alpha_i}{K_i}\sigma_i + \frac{\alpha_i}{K_iB_i}p_i\,,\ \ i=1,2$ Matrix: $\epsilon = a_{11}\cdot\sigma - a_{12}\,p_1 - a_{13}p_2$ $v_1\zeta_1 = a_{12}\cdot\sigma + a_{22}\,p_1 + a_{23}p_2$ $v_2\zeta_2 = a_{13}\cdot\sigma + a_{23}\,p_1 + a_{33}p_2$ Compatibility $\epsilon = v_1\epsilon_1 + v_2\epsilon_2$ $\zeta = v_1\zeta_1 + v_2\zeta_2 = 0$

It should be noted that, however, not necessarily would all these experiments generate linearly independent equations. Therefore, the problem of finding coefficients a_{ij} might not come to a closure, merely by using equations written through these tests. In fact, it can be proved that the last experiment in Table A-1 can be considered as the general case of such experiments. That is to say, the equations generated by all other experiments may be written as linear combinations of those generated by the last one. This experiment will be the focus of study through the rest of this chapter.

After some rearrangement of the terms and expressions, solution of the corresponding poroelastic constitutive equations, as given in the last row of Table 2, yields:

$$\sigma_1 = -\frac{a_{12}K_1}{v_1\alpha_1}\sigma + \left(\frac{1}{B_1} - \frac{a_{22}K_1}{v_1\alpha_1}\right)p_1 - \frac{a_{23}K_1}{v_1\alpha_1}p_2 \tag{2-5}$$

$$\sigma_2 = -\frac{a_{13}K_2}{v_2\alpha_2}\sigma - \frac{a_{23}K_2}{v_2\alpha_1}p_1 + \left(\frac{1}{B_2} - \frac{a_{33}K_2}{v_2\alpha_2}\right)p_2 \tag{2-6}$$

$$\left(a_{11} + \frac{a_{12}}{\alpha_1} + \frac{a_{13}}{\alpha_2}\right)\sigma + \left[a_{12} + \frac{a_{22}}{\alpha_1} + \frac{v_1(1 - B_1\alpha_1)}{B_1K_1}\right]p_1 - \left[a_{13} + \frac{a_{33}}{\alpha_2} + \frac{v_2(1 - B_2\alpha_2)}{B_2K_2}\right]p_2 = 0 \tag{2-7}$$

Since σ, p_1, p_1 are selected arbitrarily, their coefficients in equation (2-7) should vanish. Therefore, three of the required equations can be found using this equation. In order to find more equations, we consider the condition of microscopic equilibrium of a material element encompassing the constituents' interface, as shown in Figure 10.

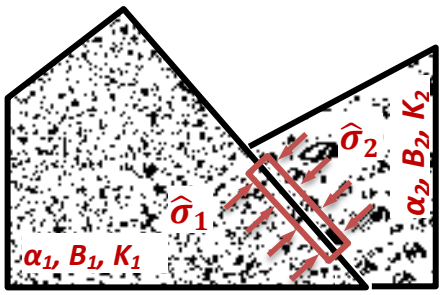

Figure 10. Static equilibrium of a material element encompassing the constituents interface.

We can choose the aspect ratio of this material element large enough to have the effect of shear stress components on its smaller sides diminished. Therefore, in order for this element to be statically in equilibrium, we must have $\hat{\sigma}_1 = \hat{\sigma}_2$. This condition provides us with 3 more equations incorporating the coefficients a_{ij} through Equations (2-5) and (2-6). These equations, along with the ones which were found previously, are listed below:

$$\begin{cases} a_{11} + \dfrac{a_{12}}{\alpha_1} + \dfrac{a_{13}}{\alpha_2} = 0 \\ a_{12} + \dfrac{a_{22}}{\alpha_1} = -\dfrac{v_1(1 - B_1\alpha_1)}{B_1 K_1} \\ a_{13} + \dfrac{a_{33}}{\alpha_2} = -\dfrac{v_2(1 - B_2\alpha_2)}{B_2 K_2} \\ \dfrac{a_{12}K_1}{v_1\alpha_1} - \dfrac{a_{13}K_2}{v_2\alpha_2} = 0 \\ \dfrac{a_{22}K_1}{v_1\alpha_1} - \dfrac{a_{23}K_2}{v_2\alpha_1} = \dfrac{1}{B_1} \\ \dfrac{a_{33}K_2}{v_2\alpha_2} - \dfrac{a_{23}K_1}{v_1\alpha_1} = \dfrac{1}{B_2} \end{cases} \tag{2-8}$$

The solution of system of Equations (2-8) gives:

$$\begin{cases} a_{11} = \dfrac{1}{K} \\ a_{12} = -\dfrac{v_1\alpha_1}{K_1}\left[K\left(\dfrac{v_1}{K_1}+\dfrac{v_2}{K_2}\right)\right]^{-1} \\ a_{12} = -\dfrac{v_2\alpha_2}{K_2}\left[K\left(\dfrac{v_1}{K_1}+\dfrac{v_2}{K_2}\right)\right]^{-1} \\ a_{22} = \dfrac{v_1\alpha_1}{B_1K_1} - \left[\dfrac{v_1\alpha_1K_2}{(v_1K_2+v_2K_1)^2}\right]^2\left(\dfrac{1}{K}-\dfrac{v_1}{K_1}-\dfrac{v_2}{K_2}\right) \\ a_{33} = \dfrac{v_2\alpha_2}{B_2K_2} - \left[\dfrac{v_2\alpha_2K_1}{(v_1K_2+v_2K_1)^2}\right]^2\left(\dfrac{1}{K}-\dfrac{v_1}{K_1}-\dfrac{v_2}{K_2}\right) \\ a_{23} = \dfrac{v_1v_2\alpha_1\alpha_2K_1K_2}{(v_1K_2+v_2K_1)^2}\left(\dfrac{1}{K}-\dfrac{v_1}{K_1}-\dfrac{v_2}{K_2}\right) \end{cases} \tag{2-9}$$

Equation (2-9) still involves the unknown bulk modulus of mixture. In order to find it, we notice the compatibility relation, $v_1\epsilon_1 + v_2\epsilon_2 = \epsilon$, for a drained confining experiment on a mixture sample. Replacing ε_1 , ε_2 and ε with $\frac{\sigma}{K_1}$, $\frac{\sigma}{K_2}$ and $\frac{\sigma}{K}$ respectively, one obtains: $\frac{1}{K} = \frac{v_1}{K_1} + \frac{v_2}{K_2}$, Substitution of this result in Equation (2-9) gives:

$$\begin{aligned} a_{11} &= \frac{1}{K} = \frac{v_1}{K_1} + \frac{v_2}{K_2}, \\ a_{12} &= -\frac{v_1\alpha_1}{K_1} \\ a_{12} &= -\frac{v_2\alpha_2}{K_2} \\ a_{22} &= \frac{v_1\alpha_1}{B_1K_1} \\ a_{33} &= \frac{v_2\alpha_2}{B_2K_2} \\ a_{23} &= 0 \end{aligned} \tag{2-10}$$

These equations complete the poroelastic characterization of a dual-porosity mixture. It should be noted that they are identical with derivations of Berryman (2002) and Berryman and Pride (2002), if the effective bulk modulus is taken as the harmonic average of the constituents' compressiblities.

2.2. Properties Coefficients of Multiple-Porosity Material

The procedure for finding poroelastic coefficients of a multiple-porosity material follows and extends the formulations of section 2.1.

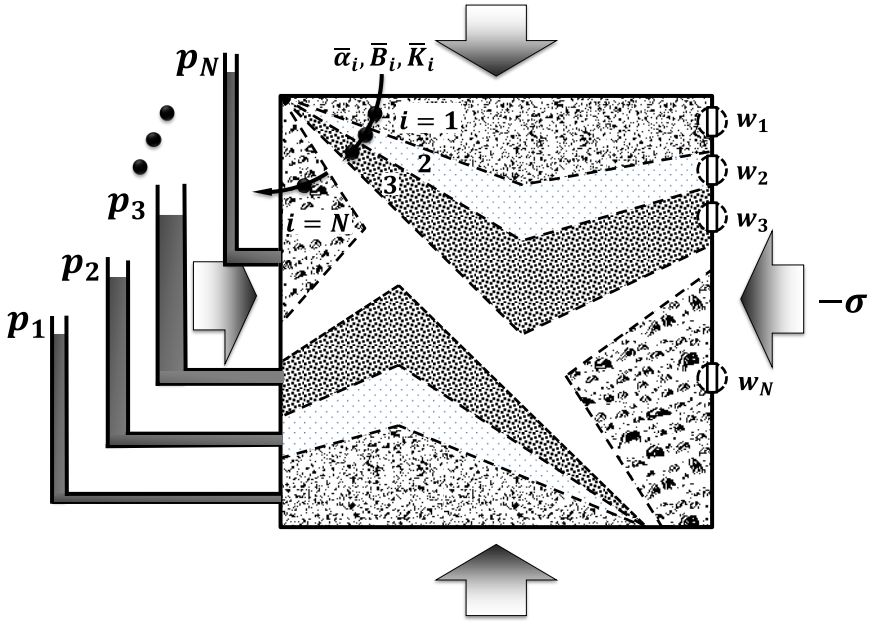

Figure 11. Schematic of the multiple-porosity model at microscopic level, with illustrations of *N* imaginary vents $w_1,\ldots,w_N$.

The constitutive relations for individual components of the composite for a thought experiment that corresponds to the last row of Table 2 can be written as:

$$\epsilon_i = -\frac{1}{K_i}\sigma_i - \frac{\alpha_i}{K_i}p_i, \quad i = 1, \ldots, n \tag{2-11}$$

$$\zeta_i = -\frac{\alpha_i}{K_i}\sigma_i + \frac{\alpha_i}{K_i B_i}p_i\,, \quad i = 1, \ldots, n \tag{2-12}$$

Similarly, the following equations can be written for the bulk material:

$$\epsilon = a_{11}\sigma - \sum_{k=2}^{n} a_{1k}\, p_i \tag{2-13}$$

$$v_{(i-1)}\zeta_{(i-1)} = a_{i1}\sigma - \sum_{k=2}^{n} a_{ik}\, p_{(i-1)}\,, \quad i = 2, \ldots, n+1 \tag{2-14}$$

The geometrical compatibility can be stated as follows:

$$\sum_{k=1}^{n} v_k \, \epsilon_k = \epsilon \tag{2-15}$$

Substitution of Equations (2-15) and (2-11) in Equation (2-13) yields:

$$\left(a_{11} - \sum_{k=1}^{n} \frac{v_k}{K_k}\right)\sigma + \sum_{i=2}^{n+1} \left(a_{1i} + \frac{v_i \alpha_i}{K_i}\right) \cdot p_{(i-1)} \tag{2-16}$$

Again, the condition of the static equilibrium of components $\sigma_i = \sigma$, as shown in Figure 10, is used here. Since σ, p_i are selected arbitrarily, their coefficients in equation (2-16) should vanish. That would determine the coefficients a_{1i} as follows:

$$a_{11} = \sum_{k=1}^{n} \frac{v_k}{K_k} \tag{2-17}$$

$$a_{1i} = -\frac{v_i \alpha_i}{K_i}, i = 1, \dots, n+1 \tag{2-18}$$

We may proceed with Equation (2-14), which in effect returns:

$$\left(a_{1i} + \frac{v_i \alpha_i}{K_i}\right)\sigma + \left(a_{ii} - \frac{v_i \alpha_i}{B_i K_i}\right) \cdot p_i + \sum_{k=2}^{n,k \neq i} a_{ik} \cdot p_i = 0 \tag{2-19}$$

Again, Since σ, p_i are selected arbitrarily, their coefficients in Equation (2-19) should vanish. The first term reproduces Equation (2-18), while the second and third terms yield:

$$a_{ij} = 0, \ \ (i > 2, i \neq j) \tag{2-20}$$

$$a_{ii} = \frac{v_i \alpha_i}{B_i K_i}, \qquad i = 2, \dots, n+1 \tag{2-21}$$

Equations (2-17), (2-18), (2-20) and (2-21) complete the information required to determine the mechanical properties coefficients for a multiple-porosity homogenous poroelastic material as follows:

$$\begin{pmatrix} \varepsilon \\ \zeta_1 \\ \vdots \\ \zeta_N \end{pmatrix} = \begin{pmatrix} \sum_{k=1}^{n} \frac{v_k}{K_k} & -\frac{v_1\alpha_1}{K_1} & \cdots & -\frac{v_N\alpha_N}{K_N} \\ -\frac{v_1\alpha_1}{K_1} & \frac{v_1\alpha_1}{B_1K_1} & \cdots & 0 \\ \vdots & \vdots & \ddots & \vdots \\ -\frac{v_N\alpha_N}{K_N} & 0 & \cdots & \frac{v_N\alpha_N}{B_NK_N} \end{pmatrix} \cdot \begin{pmatrix} \sigma \\ p_1 \\ \vdots \\ p_N \end{pmatrix} \tag{2-22}$$

The elements of the coefficient matrix in Equation (2-22) may be interpreted through correspondence with single-porosity poroelastic properties as follows:

a_{11} is the mixture's effective bulk modulus, which in this case is derived as the harmonic average of the components' bulk moduli. This result has been obtained and examined by Berryman (2002). The reminder elements in first row of coefficient matrix represent the generalized Biot-Willis coefficients. It should be noted that none of these elements represent the effective Biot-Willis coefficient of the system. In order to find such property, we examine the undrained thought experiment, which corresponds to the second row of Table 1.1. We can define the overall undrained bulk modulus of a multi-porosity system as:

$$\frac{1}{K_u} = \frac{\partial e}{\partial \sigma}\Big|_{\zeta=0} = \frac{\partial e}{\partial \sigma} + \frac{\partial e}{\partial p}\frac{\partial e}{\partial \sigma}\Big|_{\zeta=0} = a_{11} + \left(\sum_{j=2}^{n+1} a_{1j}\right) \cdot B \tag{2-23}$$

Where, *B* is the overall Skempton's pore pressure coefficient. Equation (2-23) can be rearranged to give the overall Biot-Willis coefficient as:

$$\alpha = \left(\frac{1 - K/K_u}{B}\right) = -\sum_{j=2}^{n+1} a_{1j} \tag{2-24}$$

We notice that all other off-diagonal elements are zero. Derivations of Berryman (2002) on the basis of mixture's theory do not identically coincide with this result. However, he has confirmed that although non-vanishing, their magnitude would be practically insignificant:

> "There are fairly common practices in which this term [i.e. off diagonal terms, $a_{ij},\ i \neq 1, j$] may either vanish identically or be very small in practice" (Berryman & Pride, 2002).

In retrospect results of this study demonstrate that once a consistent poroelastic model is chosen for both the mixture and its individual components, these terms should vanish identically in order to maintain the microscopic static equilibrium of the mixture's constituents, and at the same time satisfy the corresponding constitutive relations.

Chapter 3: multiple-porosity/multiple-permeability poroelasticity

The multiple-porosity/multiple-permeability equations for homogenous fluid saturated and linearly elastic isotropic continua are derived in this chapter. These equations incorporate the effects of transient fluid flow in pore space of the medium, accounting for its inter-porosity fluid exchange effects, as well as the coupling with solid skeleton's deformation. A step-by-step approach, based on physical intuition and illustrative conceptualization is taken for clarity in the subsequent presentations, where the classical elastic and single-porosity poroelastic formulations are briefly reviewed, and then generalized to the poroelasticity of dual, as well as multiple-porosity and permeability media.

Later, these derivations are employed to find analytical solutions to fundamental consolidation-type, two-dimensional, generalize plane-strain and transient problems of multiple-porosity/multiple-permeability poroelasticity.

3.1. Conceptual presentations and constitutive modeling

Hooke's law, in its original form, describes the linear relationship between external load and deformation of an elastic body in one-dimension (Figure 12).

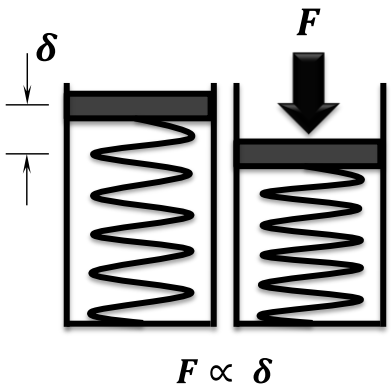

Figure 12. Hooke's law.

In three dimensions, Hooke's law for a linear isotropic and homogenous body of solid is written as follows (Boresi & Chong 2000):

$$\sigma_{ij} = 2G\varepsilon_{ij} + \lambda\varepsilon\delta_{ij} \quad (3\text{-}1)$$

where δ_{ij} denotes the Kronecker delta function. $\sigma_{ij}, \varepsilon_{ij}$ respectively stand for the stress and strain tensors, and $\varepsilon = \varepsilon_{11} + \varepsilon_{22} + \varepsilon_{33}$ is the volumetric strain. Shear modulus G and λ are Lamé's constants, a valid permutation of the two elastic constants required in 3D characterization of an isotropic elastic solid.

Terzaghi's consolidation theory (1943) incorporates the transient effects of pore fluid pressure in elastic skeleton's deformations of soil. His experiment is schematically shown in Figure 13, where a compressive load *F* is suddenly applied on a constrained sample of soil. The excess pore pressure rises to $p(0^+) = F/A$ at t=0$^+$, and until its complete dissipation, gradually transfers the stress to the soil skeleton, which is represented by a spring in Figure 13.

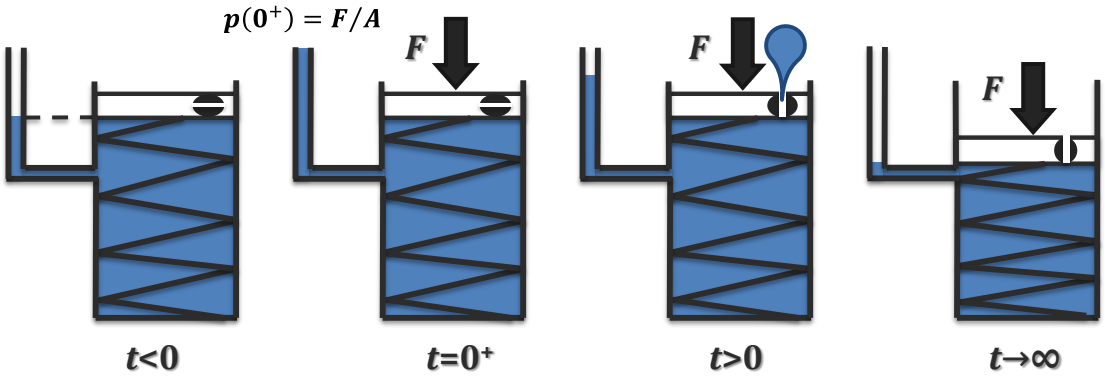

Figure 13. Schematic of one-dimensional and constrained consolidation. Adopted from Wang (2000).

Because of the constituents' incompressibility assumption, the consolidation theory is not capable of giving estimates for the initial deformations of a granular

medium. Figure 14 offers an upgrade to illustrations of Figure 13 in that it incorporates the combined effects of fluid and solid grains compressibilities. As shown in Equation (1-1), volumetric deformations of an isotropic, porous, fluid saturated and linearly elastic material can be demonstrated by three parameters. Figure 14 shows that the initial deformation of the skeleton can be conceptually represented by parallel configuration of two springs with constants determined by the solid skeleton's *drained* bulk modulus and the pore fluid's effects.

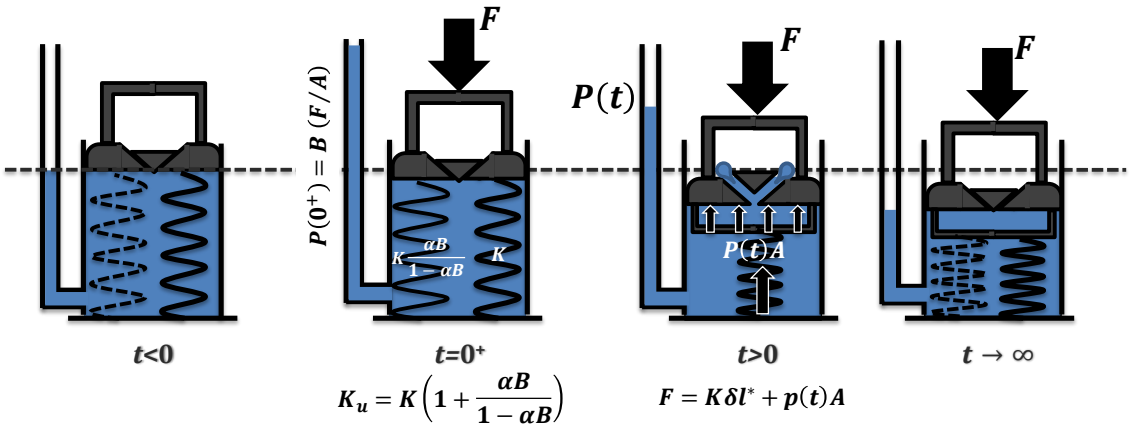

Figure 14. Conceptual representation of poroelastic deformation.

We notice that when $\alpha = B = 1$, Biot's theory of poroelasticity renders Terzaghi's consolidation theory. The quasi-static state of equilibrium in the setup corresponding to $t > 0$, can in effect, be regarded as the constitutive relation of the setup. In the three dimensional case, This relation can be written as (Biot 1941,1955):

$$\sigma_{ij} = 2G\varepsilon_{ij} + [\lambda\varepsilon - \alpha p]\delta_{ij} \qquad (3\text{-}2)$$

where the minus sign for αp implies a tensile-positive convention for the stresses. Introduction of Kronecker delta function δ_{ij} in Equation (3-2) implies the fact that the pore fluid pressure does not affect the solid skeleton's shear deformations.

Equation (3-2), together with Equation (1-1) completes the required constitutive relations for the general three-dimensional deformation of a homogenous, isotropic, and linearly poroelastic medium.

The abstract methodology taken in Figure 14 for demonstration of transient poroelastic deformations can be extended to the dual-porosity/dual-permeability case. Figure 15 portrays such generalization, in a setup comprising a series of two springs, which represent the effective drained bulk modulus of the matrix. This property has been derived in term a_{11} of Equation (2-10). Besides, the two containers in each segment of Figure 15 denote two porosity networks with distinct fluid deliverability properties. These properties are represented by difference in geometry of the needle valve within the pressurizing piston and the magnitude of the weight on top of it. The two porous networks respond differently to a sudden compressive force at $t = 0^+$, owing to their different compressibilities. As the time goes on ($t > 0$), these containers allow the fluid not only to drain from the top needle valves, but also to exchange through their inter-connecting Poiseuille tube. Usually, a more compressible pore structure is also more permeable than a less compressible pore structure. Therefore, the direction of fluid exchange between the porosity networks might switch during the drainage process. Once the load is completely transferred to the solid skeleton, the weight on top closes the valves, and the system returns to a new state of equilibrium.

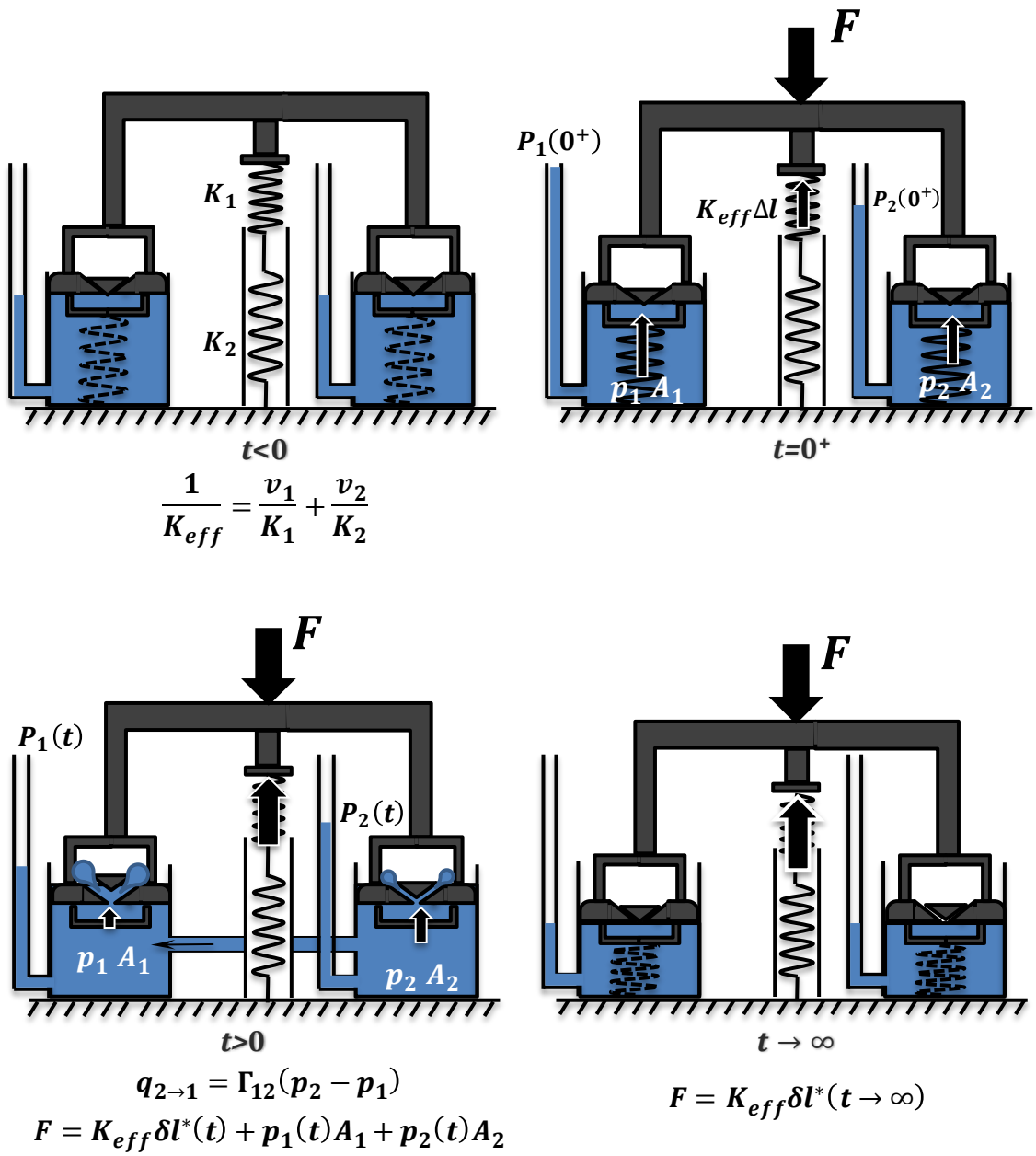

Figure 15. Conceptual representation of transient dual-porosity/dual-permeability poroelastic deformation.

We notice the quasi-static state of equilibrium in the segment of Figure 15 which corresponds to $t > 0$. The constitutive relation for a dual-poroelastic material can be accordingly written as:

$$\sigma_{ij} = 2G\varepsilon_{ij} + [\lambda\varepsilon - (\alpha_1 p_1 + \alpha_2 p_2)]\delta_{ij} \quad (3\text{-}3)$$

Equation (3-3), together with Equation (1-2), completes the required constitutive relations for the general three-dimensional deformation of a dual-poroelastic medium.

The sequence of models for the hierarchy of deforming poroelastic media can be further generalized to represent a multiple-porosity/multiple-permeability material. Figure 16 portrays a setup, comprising a series of *N* springs, which represent the effective drained bulk modulus of the matrix. This property has been derived in Equation (2-17), which later appeared as a_{11} in matrix demonstration of effective joint properties, in Equation (3-15). Further, N containers denote N porosity networks with distinct fluid deliverability characteristics as represented by difference in geometry of the needle valve within the pressurizing piston, as well as the magnitude of weight, on top of it. The N porous networks respond differently to a sudden compressive force at $t = 0^+$, owing to their different compressibilities. As the time goes on, these containers allow for not only the fluid to drainage from the top valves, but also its exchange through their inter-connecting Poiseuille tubes. It should be noted that in this case, a combinatory of $\binom{N}{2} = \frac{N(N+1)}{2}$ exchange properties Γ_{ij} can be considered for the system.

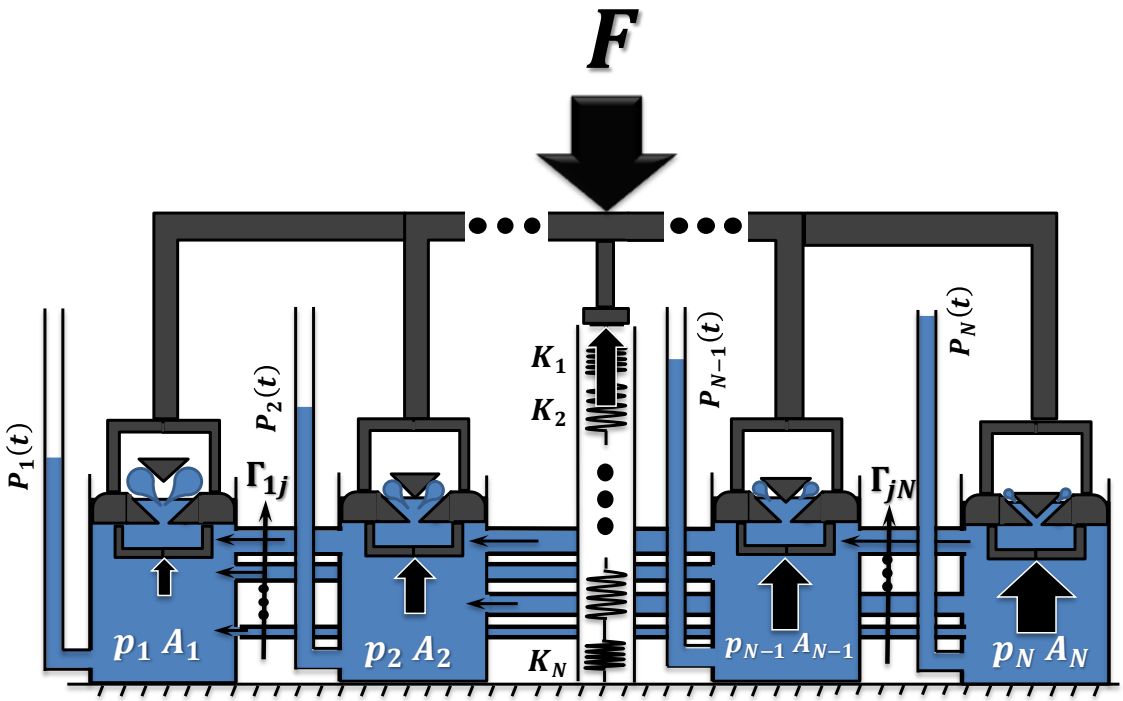

Figure 16. Conceptual representation of multiple-porosity/multiple-permeability poroelastic deformation.

We notice the condition of force balance in Figure 16. A natural extension to corresponding constitutive relation of dual-porosity poroelasticity can be written as:

$$\sigma_{ij} = 2G\varepsilon_{ij} + [\lambda\varepsilon - (\alpha_1 p_1 + \alpha_2 p_2 + \cdots + \alpha_N p_N)]\delta_{ij} \qquad (3\text{-}4)$$

Equation (3-4), together with Equation (2-22), completes the required constitutive relations for the general three-dimensional deformation of a multiply-poroelastic medium.

3.2. Field equations

The governing equations are herein outlined in a mixed formulation, that is the volumetric strain ε and the excess pore pressure *p* are considered as the independent

variables in the equilibrium and diffusion equations. The continuity of the fluid phase of porous matrix can be formulated through the following equation:

$$\frac{\partial \zeta_i}{\partial t} + \nabla . \vec{q}_i = \sum_{j=1}^{N} \Gamma_{ij}(p_j - p_i) \quad i = 1, \dots, N \tag{3-5}$$

where the terms on the right hand sides of equation (3-5) corresponds to the sum of all inter-porosity flows from porosity network j to i. These fluxes are assumed to be proportional to their pore-pressure contrast with a not necessarily symmetric proportionality coefficients matrix. However, without loss of generality the assumption of symmetry $\Gamma_{ij} = \Gamma_{ji}$ is implied through the derivations of this study. Equation (3-5), together with Darcy's law for each porosity network $\vec{q}_i = -\kappa_i \nabla p_i, \ i = 1, \dots, N$, gives:

$$\frac{\partial \zeta_i}{\partial t} - \kappa \nabla^2 p_i = \sum_{j=1}^{N} \Gamma_{ij}(p_j - p_i) \quad i = 1, \dots, N \tag{3-6}$$

where $\kappa_i = v_i k_i / \mu_i$ are the hydraulic conductivities of their corresponding porosity network. Substituting the second to $(N+1)^{th}$ row of the constitutive relations of matrix Equation (2-2) yields:

$$\alpha_i \frac{\partial \varepsilon_i}{\partial t} + \sum_{j=1}^{N} \frac{1}{M_{ij}} \frac{\partial p_i}{\partial t} = \kappa_i \nabla^2 p_i + \sum_{j=1}^{N} \Gamma_{ij}(p_j - p_i) \quad i = 1, \dots, N \tag{3-7}$$

The static equilibrium of a (poro)elastic medium can be mathematically shown by the following equation (Wang 2000):

$$\frac{\partial \sigma_{ij}}{\partial x_j} = F_i \quad i, j = 1, \dots, 3 \tag{3-8}$$

Further, under the condition of small displacements of material points, the strain tensor ε_{ij} in a continuum is obtained from kinematics of deformations as:

$$\varepsilon_{ij} = \frac{1}{2}\left(\frac{\partial u_i}{\partial x_j} + \frac{\partial u_j}{\partial x_i}\right) \tag{3-9}$$

When combined with Equation (3-9), the constitutive relation presented in Equation (3-4) can be substituted in Equation (3-8) to give:

$$G\nabla^2\mathbf{u} + (\lambda + G)\nabla\varepsilon = \sum_{i=1}^{N} \alpha_i \nabla p_i - \mathbf{F} \tag{3-10}$$

where, $\mathbf{u}$ is the displacement vector and $\mathbf{F} = 0$ is the body force. Equation (3-10) can be regarded as the governing field equation for elastic equilibrium of a multiple-porosity/multiple-permeability material.

3.3. Transient two-dimensional problems

The two-dimensional Mandel's problem investigates consolidation of a finite rectangular strip when confined and loaded from the top and bottom (Mandel 1955; Abousleiman *et al*. 1996). The industry practices of Mandel-type problems are common. Uniaxial and triaxial testing of porous rock specimens (Dickey *et al*. 1968; Abousleiman & Cui 1998) or investigations of sudden stress relief of a long core removed from subsurface wellbore (Wang 2000) are examples of its laboratory applications. Further, it has been shown that if its boundary conditions are properly selected, a Mandel-type problem with hollow axisymmetric geometry can be used to analyze the compaction of producing reservoirs (Nguyen & Abousleiman 2009).

The problem of a sphere of porous fluid saturated elastic material loaded on the surface, from which the pore fluid can freely drain by a constant uniform pressure, is known as Cryer's problem in the poromechanics literature (Cryer 1963), which is the spherically symmetric counterpart to the well-known Mandel's problem. It has been

shown through analytical solutions (Cryer 1962) and laboratory experiments (Gibson *et al*. 1963) that the pore fluid pressure in the interior of the sphere jumps by an amount when the surface traction is applied and then continues to increase for some time before decaying. Being associated with poroelastic coupling, this phenomenon is called the Mandel-Cryer effect in poromechanics books (Wang 2000).

Mehrabian and Abousleiman (2009) solved an alternative to this problem, where fluid is injected inside a poroelastic inclusion, which itself is embedded within a poroelastic matrix with different mechanical and flow properties (Figure 17). It is shown in their publication that under certain conditions governed by the stiffness contrast between the inclusion and surrounding matrix, the pore pressure decreases for some time within both the inclusion and matrix before starting to rise (Figure 18). Resembling the Mandel-Cryer effect, this phenomenon is also attributed to poroelastic coupling and is known as *dilative intake* effect, due to the imbibing action of dilating pore space at areas remote enough from the injection site.

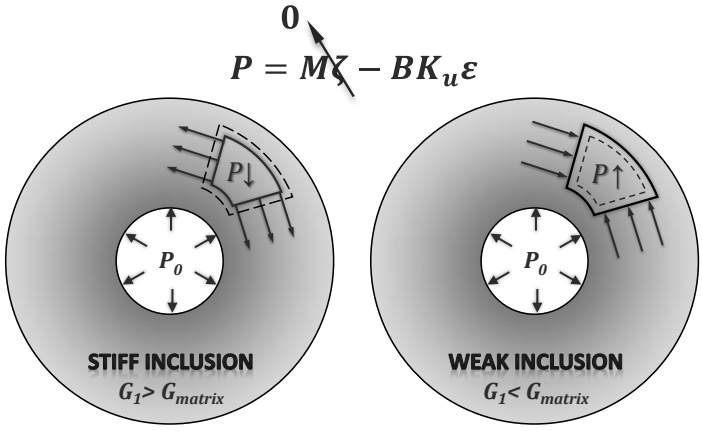

Figure 17. Dilative intake effect, after Mehrabian and Abousleiman (2009); An anomalous poroelastic behavior, where a negative pore pressure builds up within the dilating material elements of a stiff inclusion, subjected to internal fluid injection (left). Alternatively, the material elements within a weak inclusion contract, and therefore would not exhibit such anomaly in pore pressure perturbations (right).

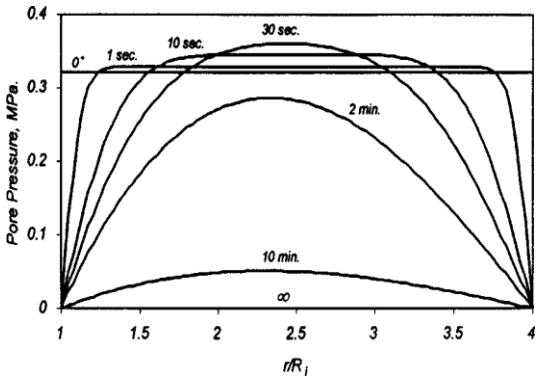

a- Mandel-Cryer effect, Abousleiman and Kanj (2004): Pressure raise overriding the load at early times.

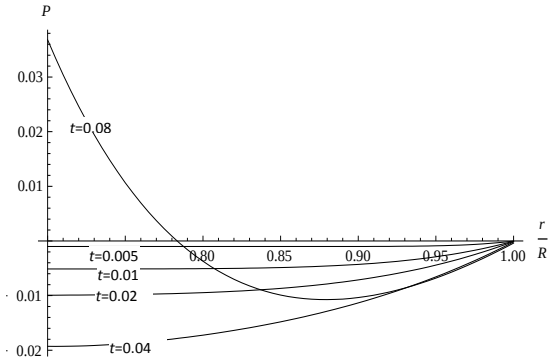

b- Dilative intake effect: Pressure drop during early injection times inside a freely dilating poroelastic sphere.

Figure 18. Comparison of the poroelastic coupling effects.

Analytical solutions to Mandel-type problems with extension of Biot's theory of poromechanics to dual-porosity/dual-permeability continua have been developed in (Nguyen & Abousleiman 2005, 2010; Nguyen 2010). Using a similar methodology and in line with formulations of sections 3.1 and 3.2, these solutions are here extended to the case of multiple-porosity/multiple-permeability media. Table 3 displays the rectangular, cylindrical and spherical variations of these consolidation-type poroelastic problems with associated boundary conditions. An integrated approach is taken here, that is the formulations are casted in one generalized form, from which the solution related to each geometry can be extracted by simple permutation of the fundamental functions of the associated Sturm-Liouville problem.

Table 3. Geometry, boundary conditions and solution functions of the consolidation-type poroelastic problems of multiple poroelasticity.

Problem	Geometry and boundary conditions	PD operator and solution functions
Mandel (1953)	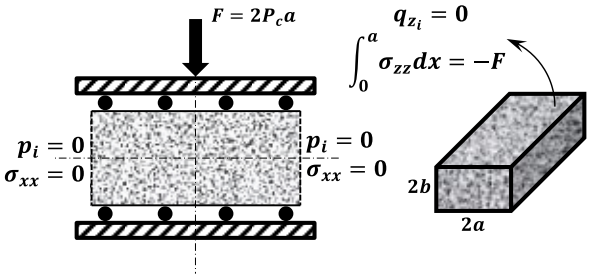	$\mathcal{L} = \frac{\partial}{\partial x^2}$ $\mathcal{F}_1(x) = \cosh x$ $\mathcal{F}_2(x) = \sinh x$
Axisymmetric Mandel (Cui and Abosuleiman 1998)	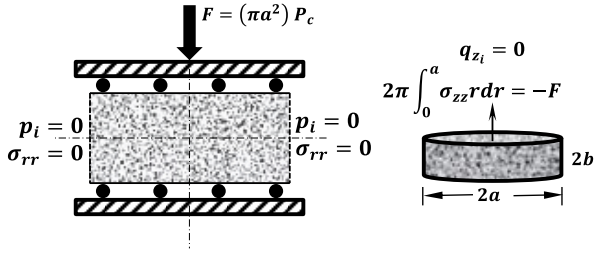	$\mathcal{L} = \frac{1}{r}\left[\frac{\partial}{\partial r}\left(r\frac{\partial}{\partial r}\right)\right]$ $\mathcal{F}_1(r) = \mathrm{I}_0(r)$ $\mathcal{F}_2(r) = \mathrm{K}_0(r)$
Cryer (1962)	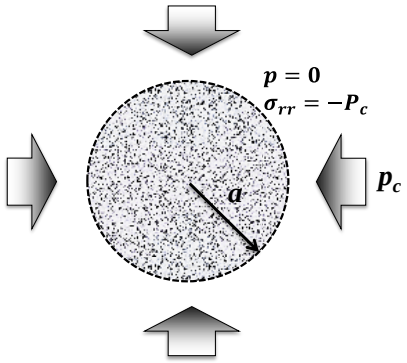	$\mathcal{L} = \frac{1}{r^2}\left[\frac{\partial}{\partial r}\left(r^2\frac{\partial}{\partial r}\right)\right]$ $\mathcal{F}_1(r) = \frac{\sinh r}{r}$ $\mathcal{F}_2(r) = \frac{\cosh r}{r}$

We start with the condition of symmetry in the problems described in Table 3. The displacement field in all cases features a radial distribution, which is an irotational field. This condition implies that $\nabla \times \vec{u} = 0$. However, for an irrotational displacement field, it can be easily proved that $\nabla^2 \mathbf{u} = \nabla \varepsilon$. With this condition, Equation (3-10) simplifies to:

$$\nabla\varepsilon = \sum_{i=1}^{N} c_{mi}\nabla p_i \tag{3-1}$$

which after integration gives:

$$\varepsilon = \sum_{i=1}^{N} c_{mi}p_i + f(t) \tag{3-2}$$

Where the new constants c_{m_i} are defined as:

$$c_{m_i} = \frac{\alpha_i(1-2\nu)}{2G(1-\nu)} \tag{3-3}$$

Substitution of Equation (3-2) into Equation (3-7) yields:

$$\left\{\mathbf{S}\frac{\partial}{\partial t} - \boldsymbol{\kappa}\,\boldsymbol{\mathcal{L}} + \boldsymbol{\Gamma}\right\}\cdot\mathbf{p} = -\boldsymbol{\alpha}f'(t) \tag{3-4}$$

where the operator $\boldsymbol{\mathcal{L}}$ corresponding to each problem's geometry is defined in Table 3. The symmetric matrices of generalized specific storage **S** (S_{ij}=S_{ji}) and hydraulic conductivity **κ**, Biot-willis coefficient vector **α,** as well as the pore pressure vector **p** are defined as:

$$\mathbf{S} = \begin{pmatrix} \frac{1}{M_1} + \alpha_1 c_{m1} & \frac{1}{M_{12}} + \alpha_1 c_{m2} & \cdots & \frac{1}{M_{1N}} + \alpha_1 c_{mN} \\ \frac{1}{M_{12}} + \alpha_2 c_{m1} & \frac{1}{M_{22}} + \alpha_2 c_{m2} & \cdots & \frac{1}{M_{2N}} + \alpha_2 c_{mN} \\ \vdots & \vdots & \ddots & \vdots \\ \frac{1}{M_{1N}} + \alpha_N c_{m1} & \frac{1}{M_{2N}} + \alpha_N c_{mN} & \cdots & \frac{1}{M_{NN}} + \alpha_N c_{mN} \end{pmatrix} \tag{3-5}$$

$$\boldsymbol{\kappa} = \begin{pmatrix} \kappa_1 & 0 & 0 \\ 0 & \ddots & 0 \\ 0 & 0 & \kappa_N \end{pmatrix} \tag{3-6}$$

$$\boldsymbol{\Gamma} = \begin{pmatrix} \sum_{j=1}^{N} \Gamma_{1j} & -\Gamma_{12} & \dots & -\Gamma_{1N} \\ -\Gamma_{12} & \sum_{j=1}^{N} \Gamma_{2j} & \cdots & -\Gamma_{2N} \\ \vdots & \vdots & \ddots & \vdots \\ -\Gamma_{1N} & -\Gamma_{2N} & \cdots & \sum_{j=1}^{N} \Gamma_{Nj} \end{pmatrix} \tag{3-7}$$

$$\boldsymbol{\alpha} = \begin{pmatrix} \alpha_1 \\ \vdots \\ \alpha_N \end{pmatrix} \tag{3-8}$$

$$\mathbf{p} = \begin{pmatrix} p_1 \\ \vdots \\ p_N \end{pmatrix} \tag{3-9}$$

Introducing the following dimensionless quantities:

$\kappa_i = (\sum_{i=1}^{N} \kappa_i)\kappa_i^*$,

$\Gamma_{ij} = \frac{(\sum_{i=1}^{N} \kappa_i)}{R^2} \Gamma_{ij}^*$,

$r = Rr^*$,

$S_{ij} = (\sum_{i=1}^{N} S_{ii}) S_{ij}^*$,

$t = \frac{R^2(\sum_{i=1}^{N} S_{ii})}{(\sum_{i=1}^{N} \kappa_i)} t^*$,

$p_i = \frac{1}{(\sum_{i=1}^{N} S_{ii})} {p_i}^*$,

Equation (3-4) converts to

$$\left\{ \boldsymbol{\kappa}^* \mathcal{L}^* - \mathbf{S}^* \frac{\partial}{\partial t^*} - \boldsymbol{\Gamma}^* \right\} \mathbf{p}^* = \boldsymbol{\alpha} f'(t^*) \tag{3-10}$$

where the asterisks are associated with new dimensionless parameters as follows:

$$\mathbf{S}^* = \begin{pmatrix} S_1^* & S_{12}^* & \dots & S_{1N}^* \\ S_{12}^* & S_2^* & \cdots & S_{2N}^* \\ \vdots & \vdots & \ddots & \vdots \\ S_{1N}^* & S_{2N}^* & \cdots & 1 - \sum_{j=1}^{N-1} S_j^* \end{pmatrix} \tag{3-11}$$

$$\boldsymbol{\kappa}^* = \begin{pmatrix} \kappa_1^* & 0 & \dots & 0 \\ 0 & \kappa_2^* & \cdots & 0 \\ \vdots & \vdots & \ddots & \vdots \\ 0 & 0 & \cdots & 1 - \sum_{j=1}^{N-1} \kappa_j^* \end{pmatrix} \tag{3-12}$$

$$\boldsymbol{\Gamma}^* = \frac{R^2}{(\sum_{i=1}^{N} \kappa_i)} \boldsymbol{\Gamma} \tag{3-13}$$

Laplace transformation of equation (3-10) on the time variable *t* result in the following equation:

$$\left\{ \boldsymbol{\kappa} \frac{1}{r^2} \boldsymbol{\mathcal{L}} - (s\mathbf{S} + \boldsymbol{\Gamma}) \right\} \cdot \mathbf{p} = \boldsymbol{\alpha} s \tilde{f} \tag{3-14}$$

where the asterisks associated with dimensionless parameters are dropped for simplicity in notation. *s* denotes the transformed variable in Laplace space and the tilde ~ on top identifies a transformed function. The solution of equation (3-14) is found from theory of system of ODEs and can be stated in the following form (Edwards and Penny 1996):

$$\tilde{\mathbf{p}}(r) = \begin{pmatrix} \chi_{11} & \chi_{12} & \cdots & \chi_{1N} \\ \chi_{21} & \chi_{22} & \cdots & \chi_{2N} \\ \vdots & \vdots & \ddots & \vdots \\ \chi_{N1} & \chi_{N1} & \cdots & \chi_{NN} \end{pmatrix}$$

$$\cdot \left\{ \begin{pmatrix} A_1(s)\, \mathcal{F}_1\left(r\sqrt{\lambda_1}\right) \\ \vdots \\ A_N(s)\, \mathcal{F}_1\left(r\sqrt{\lambda_N}\right) \end{pmatrix} + \begin{pmatrix} B_1(s)\, \mathcal{F}_2\left(r\sqrt{\lambda_1}\right) \\ \vdots \\ B_N(s)\, \mathcal{F}_2\left(r\sqrt{\lambda_N}\right) \end{pmatrix} \right\} \qquad (3\text{-}15)$$

$$+ \begin{pmatrix} \psi_1 \\ \vdots \\ \psi_N \end{pmatrix} \tilde{f}$$

where, symbol r is used as a general term corresponding to radial dimension in spherical and cylindrical coordinates, or x in rectangular coordinates system. Functions $\mathcal{F}_1$ and $\mathcal{F}_2$ are defined in Table 3, corresponding to each geometry. $A_1(s)$ to $A_N(s)$ and $B_1(s)$ to $B_N(s)$ in equation (3-15) are arbitrary functions of integration. λ_1 , $\boldsymbol{\chi}_i = (\chi_{1i} = 1, \chi_{2i}, \ldots, \chi_{Ni})^T$ respectively stand for the i^{th} eigenvalue and eigenvector of the characteristic matrix $\mathbf{M} = \boldsymbol{\kappa}^{-1}(s\mathbf{S} + \boldsymbol{\Gamma})$ of the system of ODEs in Equation (3-14), and $\boldsymbol{\Psi} = (\psi_1, .., \psi_N)^T = -s(s\mathbf{S} + \boldsymbol{\Gamma})^{-1} \cdot \boldsymbol{\alpha}$ is its particular solution vector.

The condition of symmetry at the center point (or center axis) of problem geometries requires $B_i(s) = 0$. However, it should be noted that this condition does not hold when an inner boundary corresponding to a concentric cavity is added to the geometry of consideration. These problems will be addressed Chapter 5 while using the hollow spherical and cylindrical geometrical models in simulation of some applied geomechanics problems.

The solution can be followed with the condition of free pressure at the boundary corresponding to $r = 1$

$$p_i(1,t) = 0 \tag{3-16}$$

Substitution in Equation (3-15) gives:

$$\begin{pmatrix} A_1(s)\,\mathcal{F}_1\left(r\sqrt{\lambda_1}\right) \\ \vdots \\ A_N(s)\,\mathcal{F}_1\left(r\sqrt{\lambda_N}\right) \end{pmatrix} = -\begin{pmatrix} \chi_{11} & \chi_{12} & \cdots & \chi_{1N} \\ \chi_{21} & \chi_{22} & \cdots & \chi_{2N} \\ \vdots & \vdots & \ddots & \vdots \\ \chi_{N1} & \chi_{N1} & \cdots & \chi_{NN} \end{pmatrix}^{-1} \cdot \begin{pmatrix} \psi_1 \\ \vdots \\ \psi_N \end{pmatrix} \tilde{f} \tag{3-17}$$

Or,

$$A_i(s) = -\tilde{f}\,\frac{\mathrm{Det}[\mathbf{X}_{\psi,i}]}{\mathrm{Det}[\mathbf{X}]\cdot\mathcal{F}_1\left(\sqrt{\lambda_i}\right)} \tag{3-18}$$

Det in Equation (3-18) denotes the determinant of a matrix whose elements are eigenvectors $\boldsymbol{\chi}_i$. $\mathbf{X}_{\psi,i}$ is defined by replacing the i^{th} column of the eigenvectors matrix $\mathbf{X} = \left[\boldsymbol{\chi}_\mathbf{1}^\mathbf{T}, \boldsymbol{\chi}_\mathbf{2}^\mathbf{T}, \ldots, \boldsymbol{\chi}_\mathbf{N}^\mathbf{T}\right]$ with $\boldsymbol{\Psi}$. Substituting back into Equation (3-15) gives:

$$\tilde{p}_i(r) = \tilde{f}\left[\psi_i - \frac{1}{\mathrm{Det}[\mathbf{X}]}\sum_{j=1}^{N}\frac{\chi_{ij}\mathrm{Det}[\mathbf{X}_{\psi,j}]\,\mathcal{F}_1\left(r\sqrt{\lambda_j}\right)}{\mathcal{F}_1\left(\sqrt{\lambda_j}\right)}\right] \tag{3-19}$$

the constitutive relations of a multi-poroelastic material are rewritten below from Equation (3-4):

$$\frac{\sigma_{ij}}{2G} = \varepsilon_{ij} + \left(\frac{\nu}{1-2\nu}\,\varepsilon - \gamma\sum_{i=1}^{N}\alpha_i p_i\right)\delta_{ij} \tag{3-20}$$

where the second are Lamé constant λ is replaced by its equivalent expression in terms of shear modulus G and Poisoon's ratio ν. $\gamma = (2G\sum_{i=1}^{N} S_i)^{-1}$ is a factor for rescaling the pressure terms in terms to be consistent with non-dimensionalization of

σ_{ij}. Equations (3-19) and (3-1) can be introduced into Equation (3-20) to give expressions for stress tensor, as follows:

$$\frac{\tilde{\sigma}_{ij}}{2G} = \varepsilon_{ij} - \left[\frac{\gamma(1-2\nu)}{(1-\nu)}\sum_{i=1}^{N}\alpha_i\tilde{p}_i - \tilde{f}\left(\frac{\nu}{1-2\nu}\right)\right]\delta_{ij} \tag{3-21}$$

Thus far, the three consolidation-type problems are reduced to finding the arbitrary function $f(t)$. The condition of normal stress at confined surface provides us with the required information for this purpose. Details of the procedure in finding $\tilde{f}(s)$ from the stress boundary condition at confined surface will not be addressed here, and interested reader is referred to Appendix A. The final expressions for pressure, stress and displacement are presented below:

$$\frac{\tilde{p}_i(r)}{\gamma P_c} = \frac{-\,\mathrm{Det}[\mathbf{X}]\;\psi_i + \sum_{j=1}^{N}\left\{\chi_{ij}\mathrm{Det}[\mathbf{X}_{\psi,j}]\dfrac{\mathcal{F}_1\left(r\sqrt{\lambda_j}\right)}{\mathcal{F}_1\left(\sqrt{\lambda_j}\right)}\right\}}{s\left\{\mathrm{Det}[\mathbf{X}]\,\psi + m\sum_{i=1}^{N}\left[\beta_i\mathrm{Det}[\mathbf{X}_{\psi,i}]\dfrac{\int_0^1\mathcal{F}_1\left(r\sqrt{\lambda_i}\right)r^n dr}{\mathcal{F}_1\left(\sqrt{\lambda_i}\right)}\right]\right\}} \tag{3-22}$$

$$\frac{\tilde{\sigma}_{zz}(r)}{P_c} = -\frac{\mathrm{Det}[\mathbf{X}]\,\psi + \sum_{i=1}^{N}\beta_i\mathrm{Det}[\mathbf{X}_{\psi,i}]\mathcal{g}(r;\lambda_i)}{s\left\{\mathrm{Det}[\mathbf{X}]\,\psi + m\sum_{i=1}^{N}\left[\beta_i\mathrm{Det}[\mathbf{X}_{\psi,i}]\dfrac{\int_0^1\mathcal{F}_1\left(r\sqrt{\lambda_i}\right)r^n dr}{\mathcal{F}_1\left(\sqrt{\lambda_i}\right)}\right]\right\}} \tag{3-23}$$

$$\frac{2G\tilde{u}_z(b)}{P_c b} = -\frac{\mathrm{Det}[\mathbf{X}]\;\psi' + \sum_{i=1}^{N}\left\{\beta_i\mathrm{Det}[\mathbf{X}_{\psi,i}]h(\lambda_i)\right\}}{s\left\{\mathrm{Det}[\mathbf{X}]\,\psi + m\sum_{i=1}^{N}\left[\beta_i\mathrm{Det}[\mathbf{X}_{\psi,i}]\dfrac{\int_0^1\mathcal{F}_1\left(r\sqrt{\lambda_i}\right)r^n dr}{\mathcal{F}_1\left(\sqrt{\lambda_i}\right)}\right]\right\}} \tag{3-24}$$

Table 4. Functions and parameters corresponding to Equations (3-22), (3-23) and (3-24).

Problem	Operator and solution functions	$g(r;\lambda_i)$	$h(\lambda_i)$	ψ	ψ'	m	n
Mandel	$\mathcal{L}=\frac{\partial}{\partial x^2}$ $\mathcal{F}_1(x)=\cosh x$	$\frac{\cosh(r\sqrt{\lambda_i})}{\cosh(\sqrt{\lambda_i})}$	0	$1+2a_1-\frac{\sum_{j=1}^{N} c_{mj}\psi_j}{\sum_{j=1}^{N} S_j}$	1	1	0
Symmetric Mandel	$\mathcal{L}=\frac{1}{r}\left[\frac{\partial}{\partial r}\left(r\frac{\partial}{\partial r}\right)\right]$ $\mathcal{F}_1(r)=\mathrm{I}_0(r)$	$\frac{\mathrm{I}_0(r\sqrt{\lambda_i})+\frac{2\mathrm{I}_1(\sqrt{\lambda_i})}{\sqrt{\lambda_i}}}{\mathrm{I}_0(\sqrt{\lambda_i})}$	$\frac{\mathrm{I}_1(\sqrt{\lambda_i})}{\mathrm{I}_0(\sqrt{\lambda_i})}$	$1+3a_1-2\frac{\sum_{i=1}^{N} c_{mi}\psi_i}{\sum_{i=1}^{N} S_i}$	$1+2a_1-\frac{\sum_{j=1}^{N} c_{mj}\psi_j}{\sum_{j=1}^{N} S_j}$	4	1
Cryer	$\mathcal{L}=\frac{1}{r^2}\left[\frac{\partial}{\partial r}\left(r^2\frac{\partial}{\partial r}\right)\right]$ $\mathcal{F}_1(r)=\frac{\sinh r}{r}$	$\frac{2}{r^3}\left[\frac{r\sqrt{\lambda_i}\tanh(r\sqrt{\lambda_i})-1}{\lambda_i}\right]$	$g(1;\lambda_i)$	$\frac{1}{3}+a_1-\frac{2}{3}\frac{\sum_{j=1}^{N} c_{mi}\psi_j}{\sum_{j=1}^{N} S_i}$	$\frac{1}{3}\left(1+\frac{\sum_{j=1}^{N} c_{mj}\psi_j}{\sum_{j=1}^{N} S_i}\right)$	2	2

3.3.1. Inversion of Laplace transforms

Once the solution is found in transformed space, the inverse Laplace transformation can be employed to find expressions of the result functions in time domain. Due the complex form of the solution expressions, in this study the numerical algorithm due to Stehfest (Cheng *et al*. 1994) has been employed to perform the inverse transforms. The Stehfest formula is defined as:

$$f(t)=\frac{\ln 2}{t}\sum_{n=1}^{N} X_n\cdot\tilde{f}\left(\frac{n\ln 2}{t}\right) \tag{3-25}$$

with the coefficient X_n given by

$$X_n=(-1)^{n+\frac{N}{2}}\sum_{j=\mathrm{Floor}\left[\frac{n+1}{2}\right]}^{\min\left(n,\frac{N}{2}\right)}\frac{j^{N/2}(2j)!}{\left(\frac{N}{2}-j\right)!\,(j-1)!\,(n-j)!\,(2j-n)!} \tag{3-26}$$

The convergence of Stehfest algorithm to the exact solution might not monotonically improve with increasing N. In fact, the numerical solution may deteriorate and eventually blow up for large N. This type of behavior is similar to an

asymptotic expansion series, in that it is highly efficient and accurate when a modest number of terms are used, but diverges as $N \to \infty$. For engineering purposes, Cheng & Abousleiman (1994) suggest the range $6 < N < 20$. Appendix B discusses this matter in more details, by comparing the numerical inversion results with exact time-domain solution of a single-porosity Cryer's problem.

3.3.2. Initial $(t = 0^+)$ solution

In this section, explicit formulas for the pore pressure buildup in consolidation problems of multiple poroelasticity will be obtained. We only present the derivations for Mandel's problem. However, the procedure would be similar for other geometries.

Fom the equilibrium equation in x-direction we have (See Appendix A):

$$\sigma_{xx} = 0 \tag{3-27}$$

Since the initial pressure rise is uniform across the sample, substituted of the constitutive relation in Equaiton (3-4) into Equation (3-27) gives:

$$\varepsilon_{xx} = -\frac{\nu}{1-2\nu}\varepsilon + \sum_{i=1}^{N} \alpha_i p_i^{0^+} \tag{3-28}$$

Since $\varepsilon_{zz} = \varepsilon - \varepsilon_{xx}$, substitution of Equation (3-28) into equilibrium equation in z-direction yields:

$$\left(\frac{1-\nu}{1-2\nu}\right)\varepsilon = \boldsymbol{\alpha}^{\mathbf{T}} \cdot \mathbf{p}^{0^+} \tag{3-29}$$

Where the vectors $\boldsymbol{\alpha}^{\mathbf{T}} = (\alpha_1 \dots \alpha_N)$ and $\mathbf{p}^{0^+} = \left(p_1^{0^+} \dots p_N^{0^+}\right)^{\mathbf{T}}$ are defined, accordingly. We also notice that $\zeta(0^+) = 0$. Therefore, the last N rows of Equation (2-2) provides us with N linear Equations in terms of $p_i^{0^+}$ and ε, as follows:

$$\boldsymbol{\alpha}\varepsilon + \mathbf{S}_{\boldsymbol{\varepsilon}} \cdot \mathbf{p}^{0^+} = 0 \tag{3-30}$$

where $S_{\varepsilon_{ij}} = \frac{1}{M_{ij}}$ is known as the *constrained storage coefficient* in poroemchanics literature (Wang, 2000). Solution of Equations (3-29) and (3-30) for ε gives:

$$\varepsilon = \frac{P_c}{\left[\left(\frac{1}{1-2\nu}\right) - 2\boldsymbol{\alpha}^{\mathbf{T}} \cdot \mathbf{S}_{\boldsymbol{\varepsilon}}{}^{-\mathbf{1}} \cdot \boldsymbol{\alpha}\right]} \tag{3-31}$$

Thereafter, the pressures are found as:

$$\mathbf{p}^{0^+} = \left(\mathbf{S}_{\boldsymbol{\varepsilon}}{}^{-\mathbf{1}} \cdot \boldsymbol{\alpha}\right)\varepsilon \tag{3-32}$$

Since the cross Biot's moduli $M_{ij}, i \neq j$ are usually much smaller than M_{ii}, the order of pressure buildup rise in porosity networks would be consistent with the order compliance their corresponding constituents in the model, that is, p^{0^+} in the "softest" constituent would be the largest, and so on.

3.3.3. Results

The obtained solution is used to simulate the response of triple-porosity shale comprising matrix pores and two fracture networks: the natural micro-fractures and macro-fractures which may have been induced by tectonic activities or hydraulic fracturing. A schematic model of such a triple porosity matrix is shown in Figure 19.

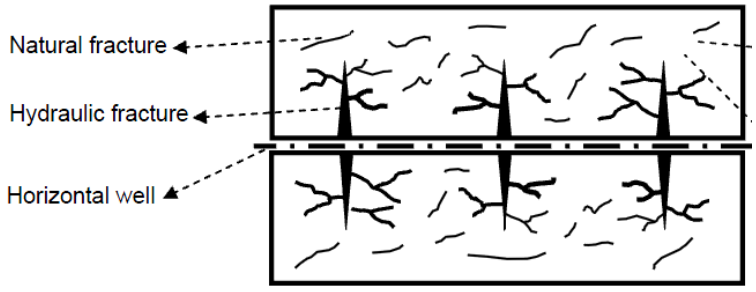

Figure 19. schematic of a tripl-porosity block of shale.

The set of physical properties from GOM shale with some modifications are adopted from Nguyen and Abousleiman (2010) and extended to account for the tertiary porous network, which in this example, represents shale's natural micro-fractures. These data are presented in Table 3.1. In addition, the assumed inter-porosity coefficients based on correlations from the individual network's permeability and void ratio are given in table 3.3. It is assumed that the secondary porosity in this case plays the role of a mediator, that is the fluid exchange between the matrix and larger fractures can take place only through the secondary porosity of micro-fractures.

The fluid Bulk modulus and viscosity are $K_f = 1744\,\mathrm{GPa}$, and $\mu = 1\,\mathrm{cp}$, respectively. For comparison purposes, the results for all considered problems are presented together to highlight the effect of their geometry in the rock response to confining pressure. For this purpose and in accord with laboratory condition of related test setup it is assumed that the $a = 3\mathrm{cm}$ in the geometries presented in Table 3.

Table 5. The intrinsic properties of a GOM shale

Problem	Bulk Modulus	Poisson's ration	Void ratio	porosity	permeability
Matrix	$\bar{K}_1 = 1\ \mathrm{GPa}$	$\bar{\nu}_1 = 0.22$	$v_1 = 97\%$	$\phi_1 = 14\%$	$\bar{k}_1 = 5\ n\mathrm{d}$
Micro-Fracture	$\bar{K}_2 = 55\mathrm{MPa}$	$\bar{\nu}_2 = 0.22$	$v_2 = 2\%$	$\phi_2 = 95\%$	$\bar{k}_2 = 50\mu\mathrm{d}$
Macro-Fracture	$\bar{K}_3 = 22.5\mathrm{MPa}$	$\bar{\nu}_3 = 0.22$	$v_3 = 1\%$	$\phi_3 = 95\%$	$\bar{k}_3 = 5\mathrm{md}$
Grain	$K_s = 27\mathrm{GPa}$	-	-	-	-

Table 6. The inter-porosity exchange coefficients (MPa.s)$^{-1}$

	Matrix	Micro-Frac	Macro-Frac
Matrix	-	$1.67(10^{-10})$	0
Micro-Fracture	$1.67(10^{-10})$	-	$1.67(10^{-12})$
Macro-Fracture	0	$1.67(10^{-12})$	-

We notice that if the void ratio of either higher-permeablity porosity network is allowed to vanish, the multiple-porosity/multiple-permeability solution should render the corresponding lower-porosity-level response of the material. For example, Letting $v_2 = v_3 = 0$ in Table 5 should recover the single-porosity solution related to the shale matrix, only. This result can be obtained by applying the following replacements and substitutions in Equations (3-22) to (3-24):

$N \to 1; \quad \mathbf{S} = S; \quad \mathbf{\Gamma} = 0; \quad \boldsymbol{\kappa} = \kappa; \quad \mathbf{X} \to 1; \quad \lambda \to s; \quad \mathbf{\Psi} \to -\alpha$

The results are shown in Figure 20 and Figure 21, where the corresponding Mandel-Cryer effect is captured in all plots. The solution exhibits a single time scale $t_0 = {a^2}/{c}$, where $c = {k}/{\mu S}$. Also, we notice that:

$$\left({p_{\max}}/{p_0^+}\right)_{\mathrm{s}} > \left({p_{\max}}/{p_0^+}\right)_{\mathrm{c}} > \left({p_{\max}}/{p_0^+}\right)_{\mathrm{r}} \tag{3-33}$$

where s, c and r denote the spherical, cylindrical and rectangular geometries, respectively. This is a reasonable observation, because of the similar relation that holds between the ratios of flux surface to enclosed volume from which the fluid flow takes place, in the three geometries:

$$\left({A}/{V}\right)_{\mathrm{s}} = \frac{3}{a} > \left({A}/{V}\right)_{\mathrm{c}} = \frac{2}{a} > \left({A}/{V}\right)_{\mathrm{r}} = \frac{1}{a} \tag{3-34}$$

For the same reason, we observe that the pressure profile corresponding to Cryer's problem dissipates first, and the one corresponding to rectangular Mandel's problem dissipates last, while the plot for axisymmetric solution traces in between.

The initial pressures, on the other hand, from derivations of section 3.3.1 compare as follows:

$$(p_0^+)_{\mathrm{s}} = B > (p_0^+)_{\mathrm{r}} = \frac{B(1+\nu_u)}{3} > (p_0^+)_{\mathrm{c}} = \frac{B}{3} \tag{3-35}$$

This result is reasonable as well, as the confining stress σ_i in each dimension builds up an initial pressure rise of $p_{0\,i}^+ = \left({}^{B}/_{3}\right)\varepsilon_i$. We notice the presumed condition of plain strain in rectangular Mandel's problem, which implies that $\sigma_{yy} = -\nu_u \sigma_{xx}$. Therefore, the initial pressure build-up would correspondingly be found as the expression shown in relation (3-35).

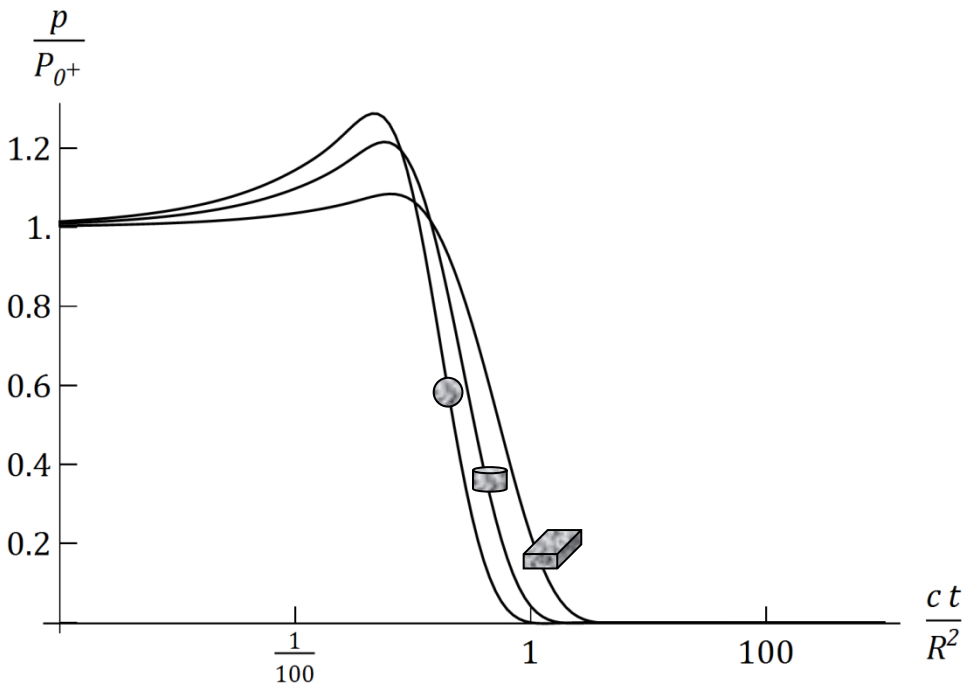

Figure 20. Transient pore pressure at the corresponding geometry's axis or point of symmetry for the single-porosity shale matrix.

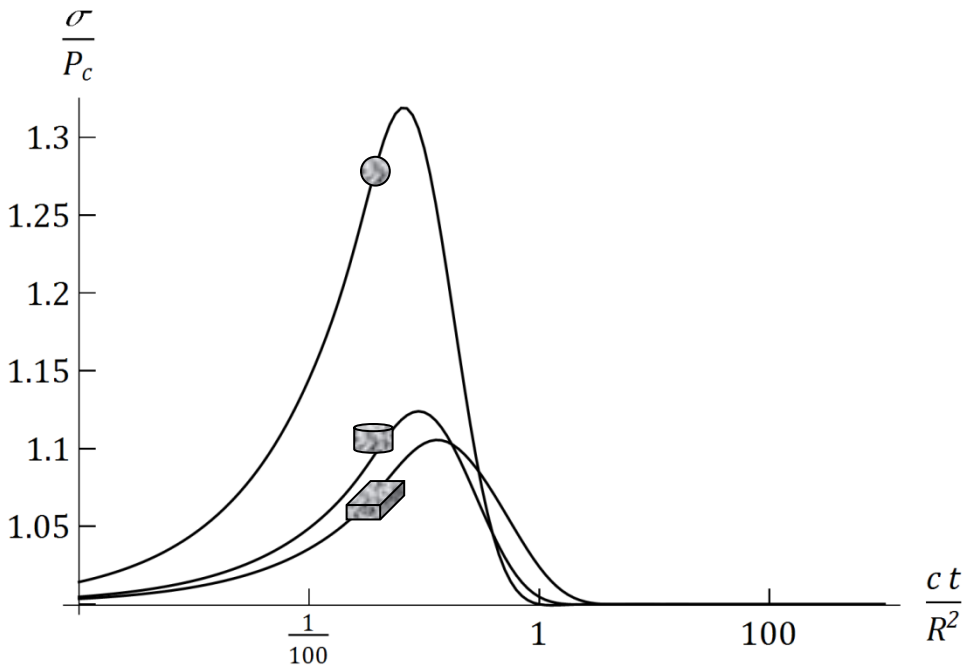

Figure 21. Transient total vertical stress at the corresponding geometry's axis or point of symmetry for the single-porosity shale matrix.

We may relax the condition of single-porosity flow by allowing $v_3 = 3\%$, as shown in Table 5, while still assuming that $v_2 = 0$. In such a case, a dual-porosity/dual-permeability solution for response of the rock recovers. This result can be obtained by applying the following replacements and substitutions in Equations (3-22) to (3-24):

$$N \to 2; \quad \mathbf{S} \to \begin{pmatrix} S_{11} & S_{12} \\ S_{12} & S_{22} \end{pmatrix}; \quad \mathbf{\Gamma} \to \Gamma_{12} \begin{pmatrix} 1 & -1 \\ -1 & 1 \end{pmatrix}; \quad \boldsymbol{\kappa} \to \begin{pmatrix} \kappa_1 & 0 \\ 0 & \kappa_2 \end{pmatrix}; \quad \mathbf{\Psi} \to -\begin{pmatrix} \alpha_1 \\ \alpha_2 \end{pmatrix}$$

Figure 22 compares the results extracted from current multiple-poroelastic solution to those obtained by digitizing the plots of Nguyen (2010), where Slightly different values were used for the input parameters (i.e. $\Gamma_{12} = 0.01$, $v_2 = 0.01$). It shows an identical match between the two solutions.

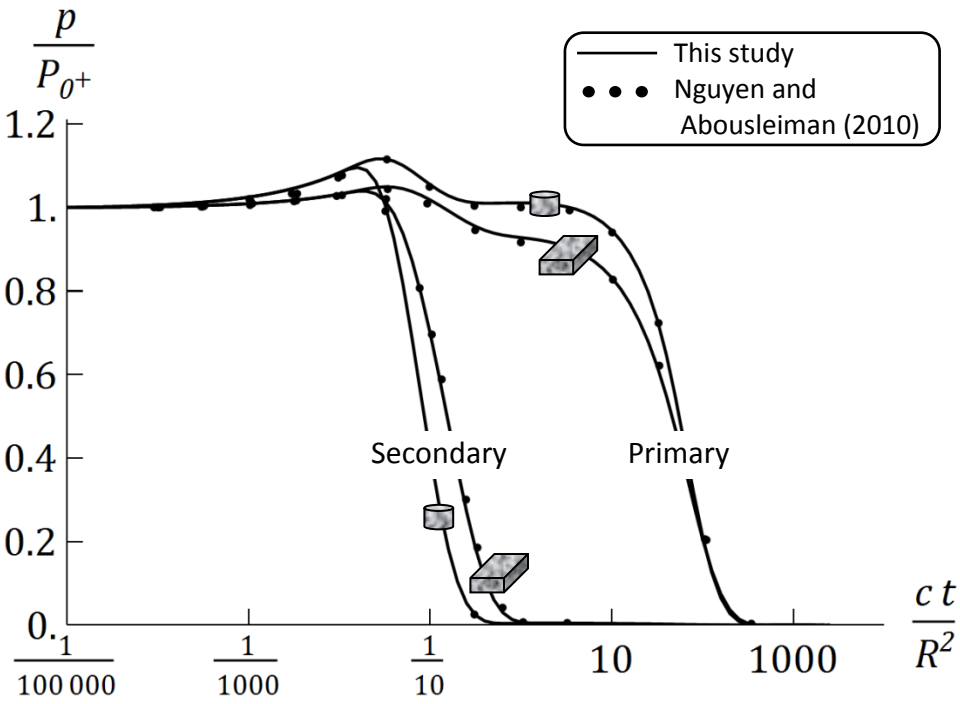

Figure 22. Comparison of the published dual-porosity/dual-permeability solution (Nguyen and Abousleiman, 2010), with the special case corresponding to $N = 2$ in the multiple-porosity/multiple-permeability solution presented in this study.

Results for the parameters used in Table 5 are shown in Figure 20 and Figure 21, where the solution exhibits a dual-time scale behavior. However, unlike the single-porosity case, these time scales are attributed to the eigenvalues of the characteristic equation of solution PDEs, and are themselves time-dependent variables. Also, we notice that the behavioral pattern of the rock's response corresponding to higher permeability network would, in general, affect and interact with the ones corresponding to lower permeability. This observation is due to the coupled deformation processes, as well as the inter-porosity fluid exchange effects. For this reason, the curves corresponding to the shale matrix's pressure (primary porosity) in Figure 23 exhibit a dual Mandel-Cryer effect.

The order of maximum relative pressure, dissipation rate and absolute value of the initial pressure rise of the three geometries for the dual-poroelastic solution follows the presentations related to the single porosity case. In this new case, however, the initial pressure both in fracture $p_{2_{0^+}}$ and matrix $p_{1_{0^+}}$ would be less than the initial pressure rise of the single porosity solution. This is a reasonable observation, due to larger compressibility of the dual-porosity mixture skeleton than the single porosity matrix.

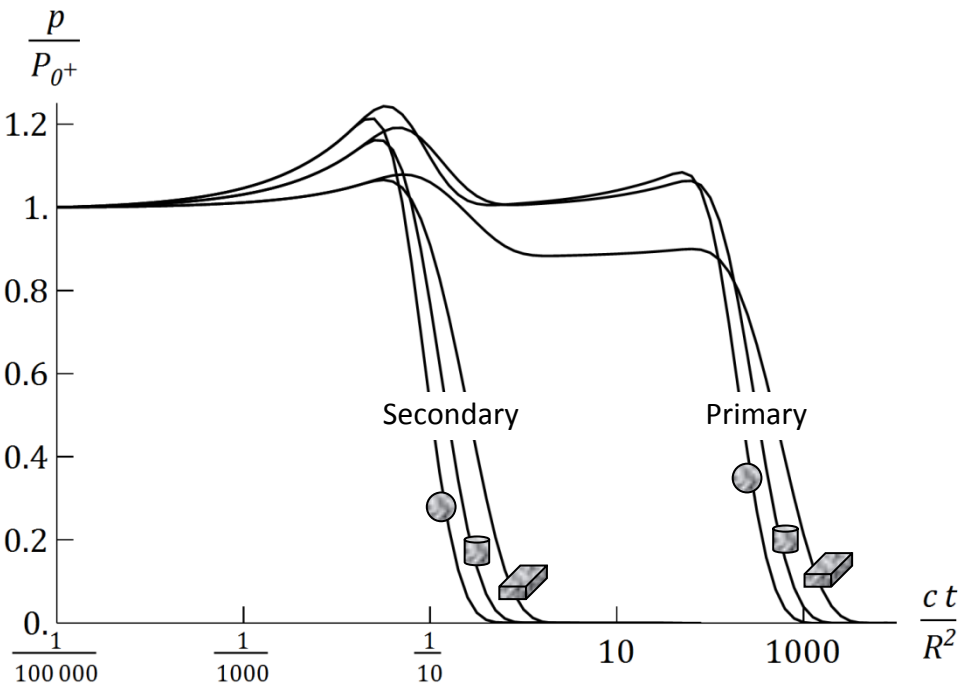

Figure 23. Dual-porosity/Dual-permeability solution simulating the dual-pressure response of fractured shale's pore pressure at the corresponding geometry's axis or point of symmetry.

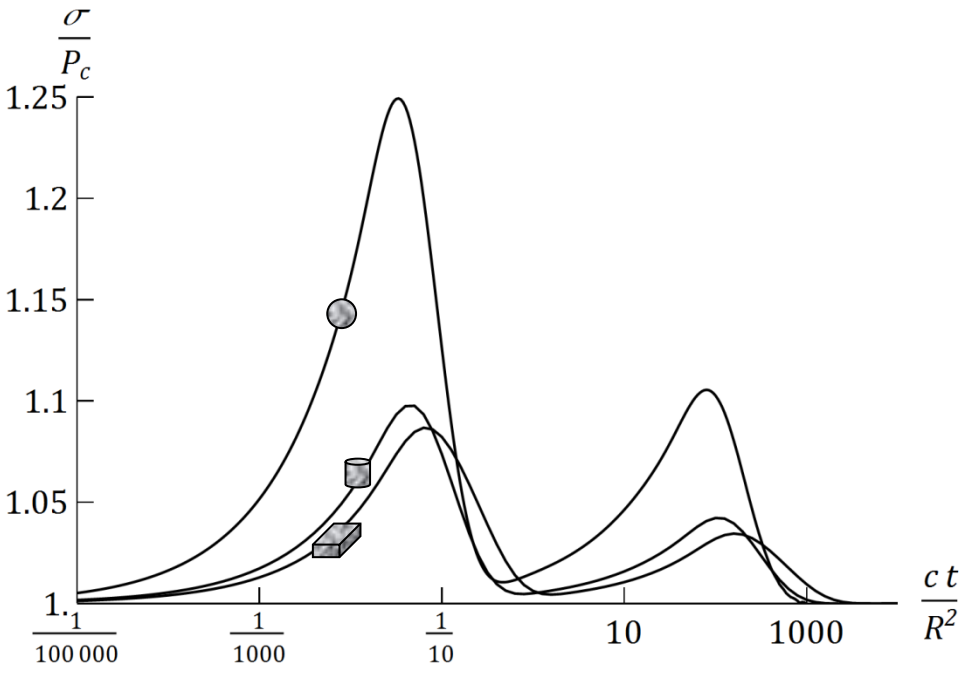

Figure 24. Dual-porosity/Dual-permeability solution simulating the response of fractured shale's vertical stress at the corresponding geometry's axis or point of symmetry.

We may further relax the condition of dual-porosity flow by allowing $v_3 = 1\%$ and $v_2 = 2\%$ as shown in Table 5. In such a case, a triple-porosity/triple-permeability solution for response of the rock recovers. This result can be obtained by applying the following replacements and substitutions in Equations (3-22) to (3-24):

$$N \to 3; \quad \mathbf{S} \to \begin{pmatrix} S_{11} & S_{12} & S_{13} \\ S_{12} & S_{22} & S_{23} \\ S_{13} & S_{23} & S_{33} \end{pmatrix}; \quad \mathbf{\Gamma} \to \begin{pmatrix} \Gamma_{12}+\Gamma_{13} & -\Gamma_{12} & -\Gamma_{13} \\ -\Gamma_{12} & \Gamma_{12}+\Gamma_{23} & -\Gamma_{23} \\ -\Gamma_{13} & -\Gamma_{23} & \Gamma_{13}+\Gamma_{23} \end{pmatrix};$$

$$\boldsymbol{\kappa} \to \begin{pmatrix} \kappa_1 & 0 & 0 \\ 0 & \kappa_2 & 0 \\ 0 & 0 & \kappa_3 \end{pmatrix}; \quad \mathbf{\Psi} \to -\begin{pmatrix} \alpha_1 \\ \alpha_2 \\ \alpha_3 \end{pmatrix}$$

Results are shown in Figure 25 and Figure 26, where the solution exhibits a triple-time scale behavior. The order of maximum relative pressure, dissipation rate and absolute value of the initial pressure rise of the three geometries for the triple-poroelastic solution follows the presentations related to the single and dual-porosity case. In this new case, however, the initial pressure in both fractures $p_{2_{0^+}}, p_{3_{0^+}}$ and matrix $p_{1_{0^+}}$ would be less than the initial pressure rise of the dual-porosity solution. This is a reasonable observation, due to larger compressibility of the triple-porosity mixture skeleton than the dual-porosity matrix.

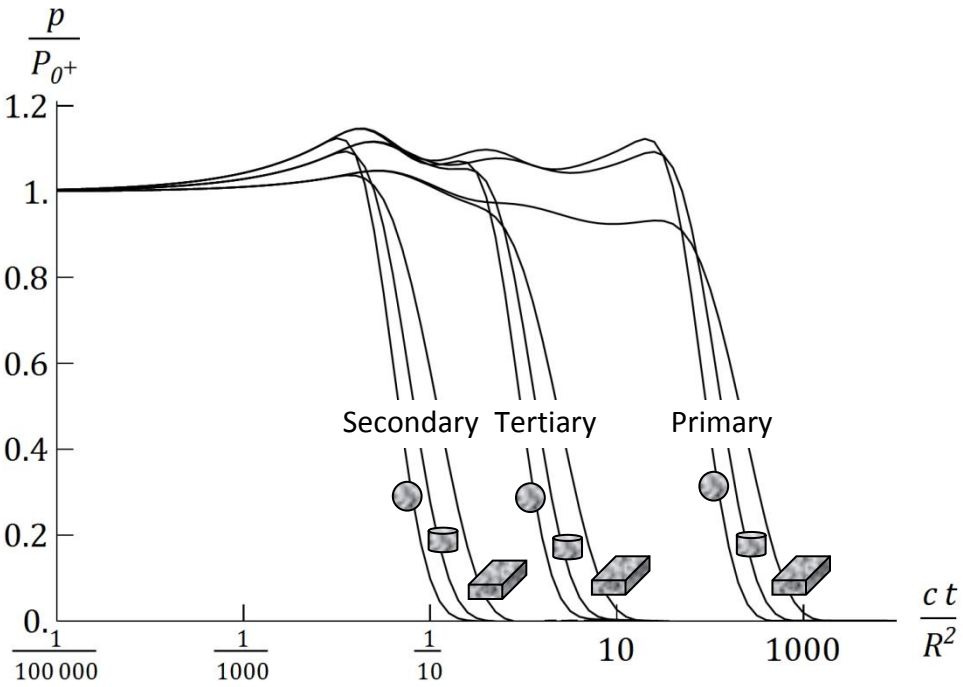

Figure 25. Triple-porosity/triple-permeability solution simulating the triple-response of fractured shale's pore pressure at the corresponding geometry's axis or point of symmetry.

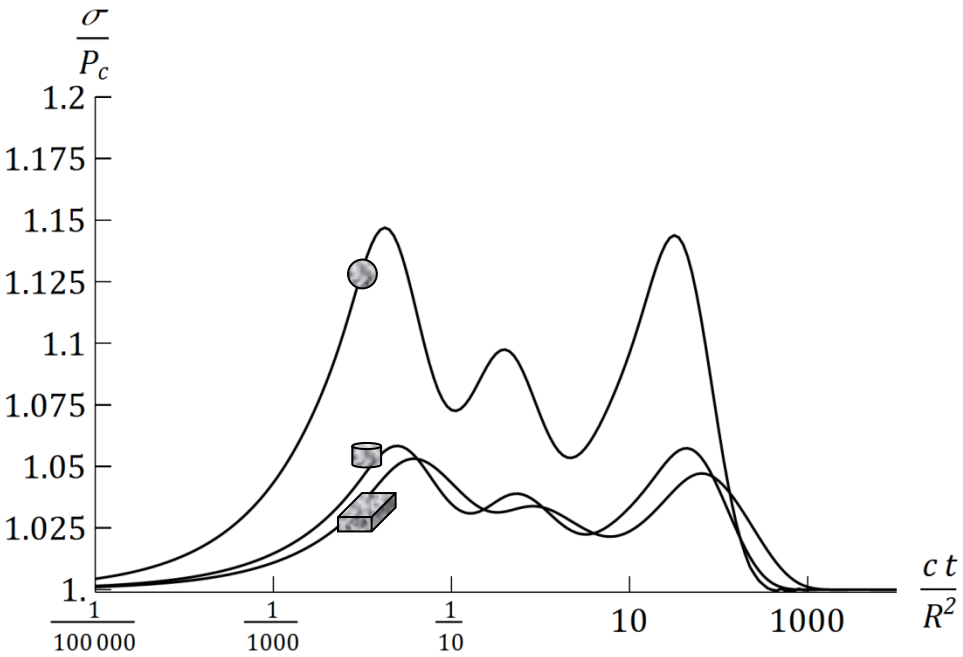

Figure 26. Triple-porosity/triple-permeability solution simulating the response of fractured shale's vertical stress at the corresponding geometry's axis or point of symmetry.

3.4. Concluding remarks

Illustrative and elaborate presentations of this chapter attempted to explore the fundamental concepts underlying constitutive modeling of multiple-porosity/multiple-permeability theory. Application of this constitutive model to the corresponding generalized plane-strain or Quasi-1D problems indicate that the hierarchy of porosity levels is self-multiplicative, in that the associated coupled flow-deformation phenomena in the case of single-porosity poroelasticity would reproduce and proliferate when upgraded to higher numbers of porosity networks.

Chapter 4: Applications

Field applications of the solutions presented in Chapter 3 are the subject matter of this Chapter. For this purpose, variations of the multiple-porosity/multiple-permeability Cryer's and axisymmetric Mandel's problems are developed to account for additional boundary conditions due to a concentric cavity within their geometry. The former applies to investigation of the sealing capacity and integrity of cap rocks during CO_2 geo-sequestration operations, while the latter is used to derive formulas for compaction and porosity reduction estimates of multiple-porosity depleting reservoirs.

4.1. Geomechanics of CO_2 Sequestration

Carbon Capture and Sequestration (CCS) is currently the focus of engineering research and practice in environmental considerations such as global climate warming. CO_2 geo-sequestration is especially prevalent because of its high storage capacity and economic feasibility. Examples of currently-active CCS field projects are Sleipner in the North Sea, and In Salah in Algeria.

Due to their large potential storage volume and their common occurrence, saline aquifers are found to be good candidates for CO_2 storage. Figure 27-a shows a schematic sketch of CO_2 injection in a saline aquifer. In Figure 27-b the Sleipner CCS project in Norway is presented, where CO_2 from west Sleipner gas field is separated from natural gas and then injected 800m below the seabed in North sea into Utsira, a saline formation.

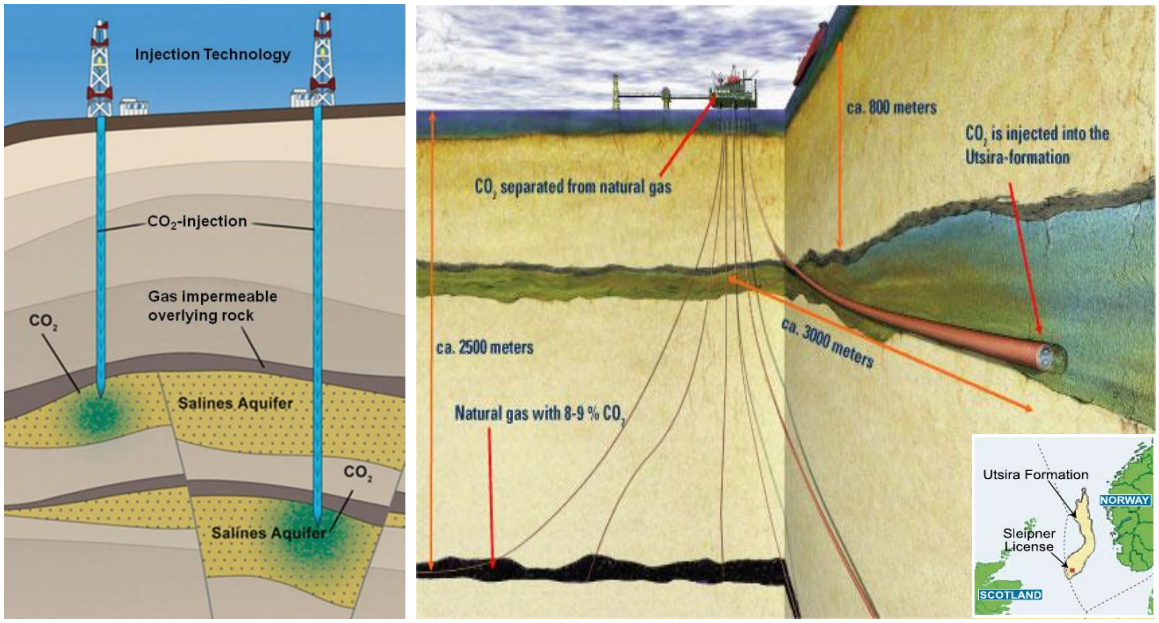

(a) (b)

Figure 27. (a) schematic of CO_2 injection into saline aquifers, and (b) Illustrative sketch of Sleipner stratigraphy, along with its associated CO_2 geo-sequestration project. Copy from KAUST-TUM special partnership annual project report (2012).

Conversely, potential risks such as seismic reactivation of the area around injection sites, in addition to environmental and ecological issues regarding long-term CO_2 leakage from the storage unit to atmosphere or groundwater, are the counter-beneficial factors of Carbon dioxide geo-sequestration. Since the storage reservoir is in principle supposed to preserve the injected fluid for unlimited period of time, the possibility of fluid leakage from it is should be assessed prior to proceeding with related injection operations.

Depending on the time-scale being considered, the CO_2 trapping mechanisms can be different. Residual, solubility, mineral and structural trappings are known measures for assessing a formation sealing capacity (Benson & Cole 2008).

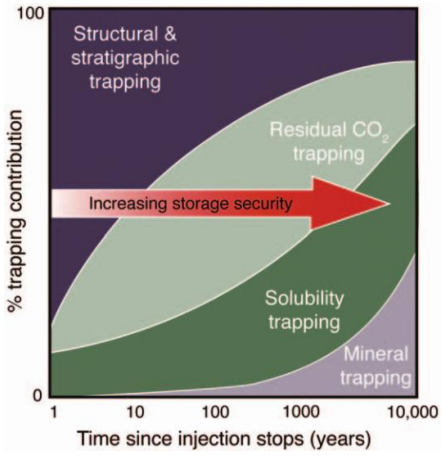

Figure 28. Evolution of trapping mechanisms with time. Copy from Benson and Cole, (2008)

The structural trapping refers to the sealing capacity and integrity of overlaying caprocks, which possibly exhibits the shortest time-scale of influence. The caprock may fail through a variety of mechanisms causing CO_2 to migrate through high permeability zones in the caprock or through faults and fractures, which extend into it.

The formulations presented in Chapter 3 enable us to investigate the sealing capacity and integrity of naturally micro-fractured caprock in Carbon dioxide geo-sequestration. The following spherically symmetric model is suggested for simulation of the caprock deformation due to the injected CO_2 pressure:

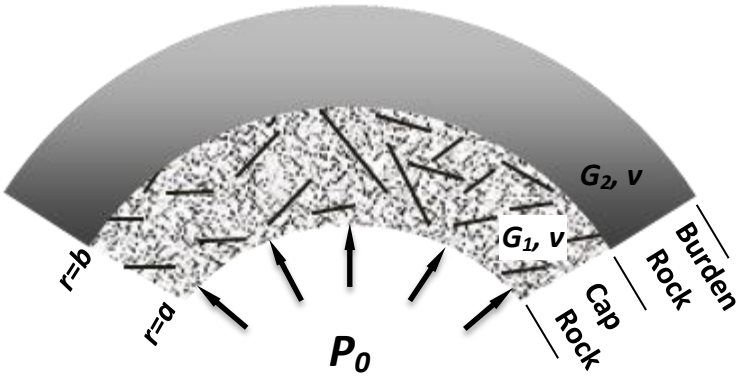

Figure 29. Spherical model of fractured caprock and overburden.

The solution domain includes caprock within a radial range of $a^* < r^* < 1$, where $r^* = r/R$ is the dimensionless radius. The burden rock may have different mechanical moduli than the caprock and engages with deformations of its outer boundary. This problem is treated through the solution of dual-poroelastic hollow sphere which follow the formulations of chapter 3. The complete solution to this new problem, along with its arbitrary functions of integration is presented in Appendix C. The numerical data used to generate results of this study are extracted from GOM shale properties presented in Table 5, with the following modifications: In order to represent a "sealing rock", the matrix and fracture permeabilities are assumed to be smaller values as: $k_1 = 1n\mathrm{d}$ and $k_2 = 1\mu\mathrm{d}$. Also inter-porosity flow coefficient $\Gamma_{12} = 1.67 \times 10^{-21}(\mathrm{MP}a)^{-1}$ is selected in a way to be consistent with relative low permeability of the mixture. Also, the volume fraction of fracture is assumed to be $v_2 = 1\%$. The pore fluid is CO_2 at super-critical phase condition, with $\mu = 0.04c\mathrm{P}$ and $K_f = 55MPa$ (Kemmere & Meyer 2006). The outer radius of the caprock's curvature is taken $b = 1000\ ft$.

The temporal pore pressure profiles at the boundary between the burden rock and caprock are shown in Figure 30. The parameter $\gamma = G_2/G_1$ significantly affects these pressure transients. We notice the *dilative intake* effect (Mehrabian & Abousleiman, 2009), an anomalous range of negative pore pressures at early times for $\gamma < 1$. A special case of this phenomenon according to $\gamma = 0$ is known as *reverse water-level* effect (Wang 2000) or *Noordberdgum* effect (Verruijt 1969) in hydrogeological literature. Further discussions on this subject are given in Chapter 3.

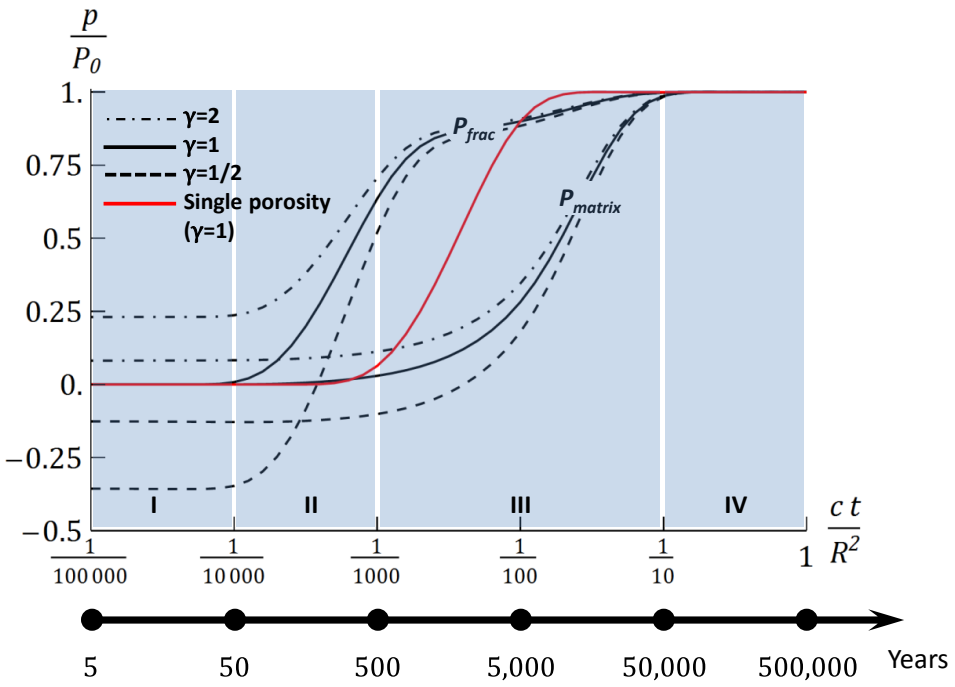

Figure 30. Caprock's Pore pressure at r=1 vs. time, with identification of four zones of investigation, corresponding to: (I) Dilative intake effect, (II) Reacting fractures with a silent matrix, (III) Dual response of fracture and matrix, and (IV) steady-state condition.

Zone (II) in Figure 30 exhibits a unique feature of multiple-porosity media's behavior. Although the caprock's matrix can still be considered a "good seal" within its associated range of time, introducing smallest volumes of fracture network to the matrix might provide the trapped fluid with effective pathways, through which it can seep out of the storage reservoir. Therefore, within the time scale of decades, Carbon dioxide will migrate all the way through the caprock thickness, generating large pressures at its boundary, which in effect, might bring about its appearance at the ground's surface. It should be noted that these fractures can be either pre-existing within the shale matrix, or induced by the CO_2 injection operations.

On this note, the remainder of this section is devoted to the failure analysis of the caprock after CO_2 injection. The effective mean stress and effective Von Mises stress are defined as follows:

$$\sigma_m' = \frac{\sigma_{kk}'}{3} = \frac{\sigma_1' + \sigma_2' + \sigma_3'}{3} \tag{4-1}$$

$$\sigma_v' = \sqrt{\frac{(\sigma_1' - \sigma_2')^2 + (\sigma_1' - \sigma_3')^2 + (\sigma_2' - \sigma_3')^2}{2}} \tag{4-2}$$

where, $\sigma_{ij}{}' = \sigma_{ij} + (\alpha_1 p_1 + \alpha_2 p_2)\delta_{ij}$ is the effective stress of a dual-porosity material and indices $i = 1,2,3$ denote principal stresses. From the first row of Equation (1-2) we obtain $\sigma_m' = K\varepsilon$. Moreover, from the spherical symmetry of the state of stress in the problem $\sigma_v' = |\sigma_{rr}' - \sigma_{\theta\theta}'|$. The plot of effective Von Mises vs. effective mean stress for values of parameter $\gamma = \frac{1}{2}, 1, 2$ is shown in Figure 31, in which both axes are scaled by the injected CO_2 pressure. The blue and red lines track the stress paths of the sphere's inner and outer boundaries, respectively. Variations of the state of effective stress in $\sigma_v' - \sigma_m'$ plane are not as significant at *r=a,* due to the early establishment of a steady pore pressure in that region. Conversely, the stress state of outer boundary is a strong function of time, due to pore pressure diffusion processes, as well as flow-deformation coupling effects.

A considerably more stable state of stress is predicted at for $\gamma = 2$, owing to the confining behavior of the stiffer burden rocks. However, with reduction of this parameter the failure envelopes expand and shift to the right. Since the horizontal axis readings return $K\varepsilon$, this shift indicates dilation of the caprock, which would be a reasonable conclusion because of a less stiff outer boundary of the caprock.

Therefore, local rock failure is more probable during the early stages of fluid leakage from the reservoir, especially at regions close to the outer boundary of the caprock.

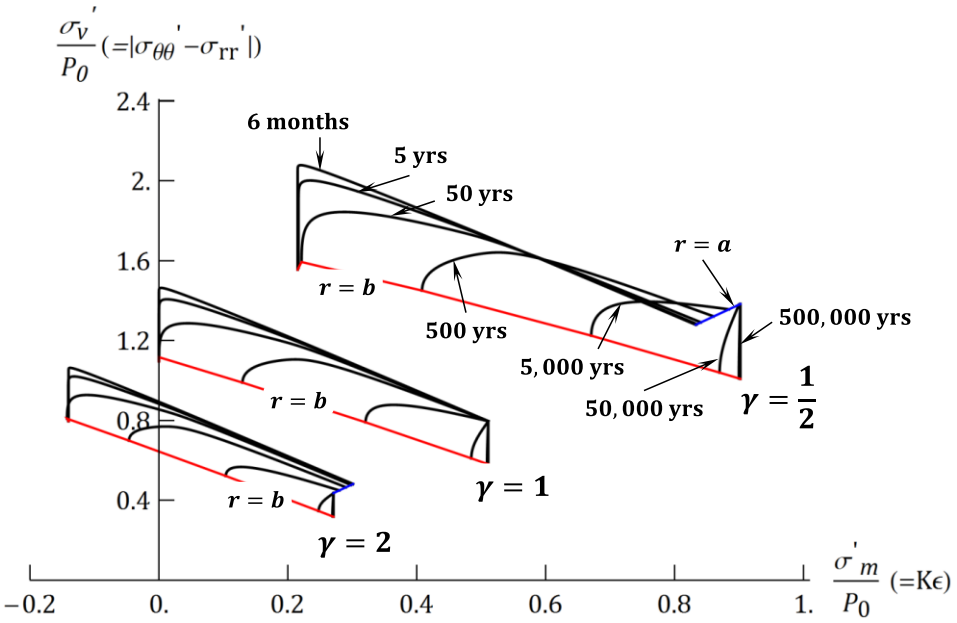

Figure 31. stress-state plane defined by the effective Von Mises and mean stresses.

4.2. Compaction of multiple-porosity/multiple-permeability depleting reservoirs

Compaction supplies the driving energy of hydrocarbon flow in some “volatile” and ”soft-rock” reservoirs. Nevertheless, it is recognized responsible for a variety of operational, structural and environmental problems in oil-fields. The associated land subsidence (Ekifosk in Norway and Wilmington-California), along with subsequent damage to surface facilities, pipelines, etc., casing deformation and well failure, fault reactivation and microsisemic activities, as well as the decreased productivity due to the reservoir’s reduced porosity and permeability, are examples of such problems (Settari 2002).

The classic Geertsma’s problem (1973), provides a solution for subsidence and compaction above a disk shape reservoir, undergoing a uniform pressure loss Δp.

Later, Segall (1992) derived elastostatic Green's functions due to a pressure source within a flat, circular ring. These functions can be used to find the stress or strain functions within a homogenous and isotropic half space incorporating any axisymmetric distribution of pressure field.

In geomechanical studies of reservoir, the compaction-induced loss of productivity should be treated as a fully-coupled flow and deformation problem, incorporating a mechanistically viable model of reservoir and burden rocks. Despite much effort which have been placed in developing efficient and accurate numerical schemes (Kim *et al.* 2011) for the coupled flow-deformation problem of depleting reservoirs, analytical solutions to the related problems mostly follow an uncoupled approach, where the pressure field is found from flow equations, first, and then substituted in the elastic equilibrium equations (Settari *et al*. 2005). The uncoupled approach, however, might produce errors tending to underestimate the compaction and porosity/permeability reduction. Naturally fractured reservoirs, in particular, are sometimes prone to huge loss of production due to reduced pore space of their embedded fractures.

In this section, an idealization of reservoir geomechanics is adopted from earlier dual-poroelastic model of Nguyen and Abousleiman (2009) is improved to the case of a multiple-porosity/multiple permeability reservoir rock. This model is shown in Figure 32.

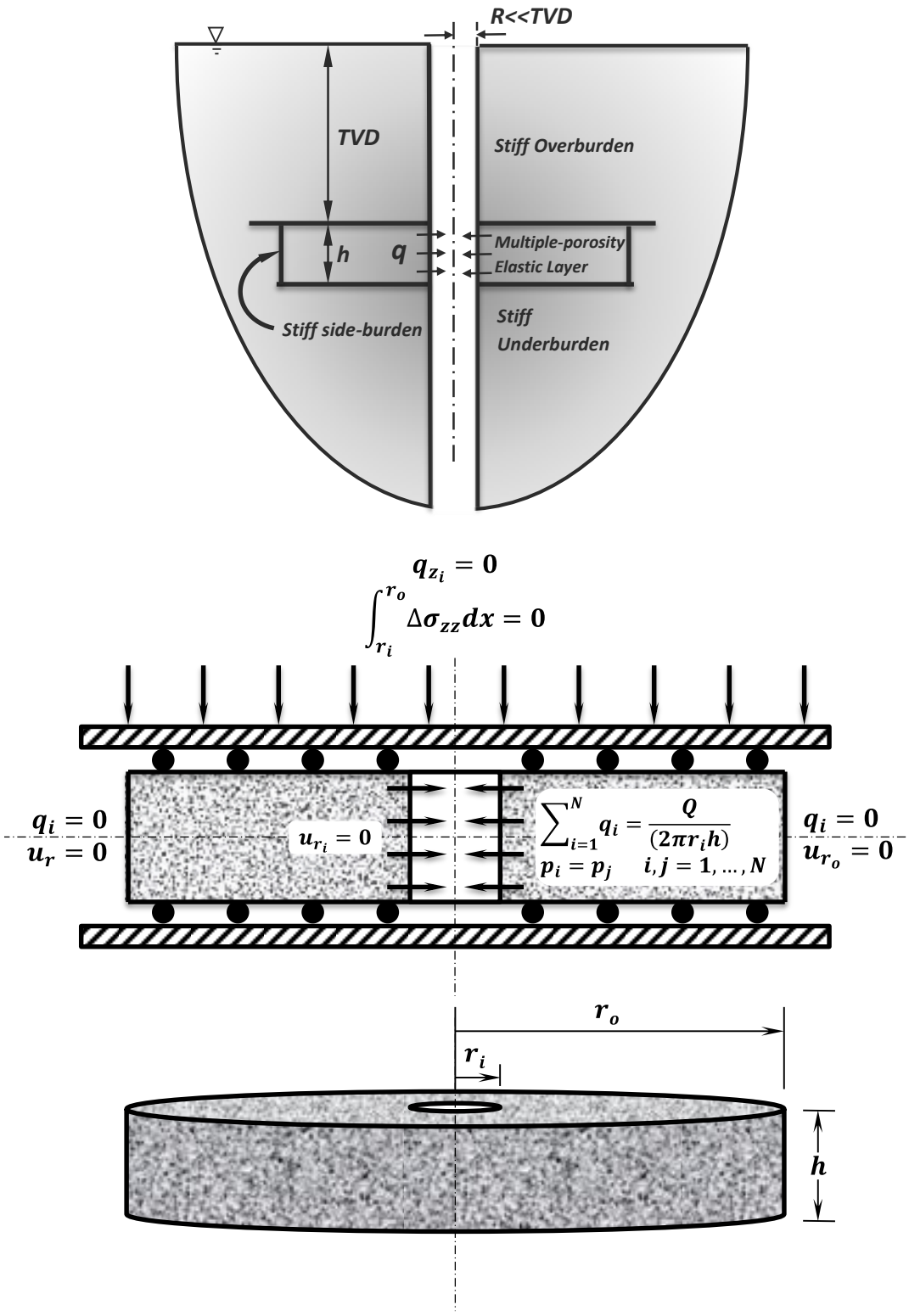

Figure 32. An idealized hollow-cylindrical geomechanics model of N-porosity/N-permeability reservoir, along with the associated $(2N+2)$ boundary conditions, adopted from Nguyen and Abousleiman (2009).

As shown in Figure 32, the flow and elastic boundary conditions are adapted to the model geometry in such a way that it maintains an axisymmetric quasi-1D consolidation, so that after deformation, any horizontal plane within the solution domain remains horizontal. This condition is imposed on the problem by allowing the shear interaction between the reservoir and burden rocks to vanish, which in general is not a valid assumption. However, plane strain models of reservoir geomechanics have been shown to be able to mimic certain behaviors of real reservoirs in deformation, and can be used as first estimate to the problem's solution. The flow boundary conditions presented in Figure 32 provide $2N$ equations for $2N$ arbitrary functions of expressions for N pressures corresponding to N porosity networks, as well as 2 extra arbitrary functions for fixed displacements at inner and outer boundaries of hollow-cylinder i.e. $u_r(r_i) = u_r(r_o) = 0$. Details related to the complete analytical solution to this problem are presented in Appendix D.

A quadruple-porosity network within a vuggy carbonate rock is considered for the numerical example which follows along this section. These porosity networks correspond to matrix and two fracture systems with different scales of size and flow conductivity, as well as a quaternary non-connected porosity due to presence of vugs within the matrix. Although they are not inter-connected, these vugs are assumed to exchange fluid with other porosity networks through the inter-porosity flow processes.

The required data of analysis are taken from (Nguyen & Abousleiman, 2009) corresponding the Ghawar field in Saudi Arabia, a predominantly carbonate reservoir with widespread dolomization and anhydrite pore-filling material. However, a number

of physical properties, such as fracture volume fraction and its assumed compressibility were missing within their publication. Moreover, the properties related to tertiary and quaternary porosities need be reasonably generated, because of the more number of distinct porosity networks considered in this study. Table 7 lists these properties.

Table 7. The intrinsic properties of the quadruple-porosity reservoir rock

Problem	Bulk Modulus	Poisson's ration	Void ratio	porosity	permeability
Matrix	$\bar{K}_1 = 11\ \mathrm{GPa}$	$\bar{\nu}_1 = 0.30$	$v_1 = 85\%$	$\phi_1 = 10\%$	$\bar{k}_1 = 1\ \mathrm{md}$
Macro-Fracture	$\bar{K}_2 = \bar{K}_1/20$	$\bar{\nu}_2 = 0.30$	$v_2 = 9\%$	$\phi_2 = 90\%$	$\bar{k}_2 = 500\mathrm{md}$
Micro-Fracture	$\bar{K}_3 = \bar{K}_1/10$	$\bar{\nu}_3 = 0.30$	$v_3 = 3\%$	$\phi_3 = 63\%$	$\bar{k}_3 = 50\mu\mathrm{d}$
Vugs	$\bar{K}_4 = \bar{K}_1/10$	$\bar{\nu}_4 = 0.30$	$v_3 = 3\%$	$\phi_4 = 50\%$	$\bar{k}_4 = 0$
Grain	$K_s = 27\mathrm{GPa}$	-	-	-	-

The inter-porosity exchange properties are presented in Table 8, as shown below:

Table 8. The inter-porosity exchange coefficients (Pa.s)$^{-1}$

	Matrix	Macro-Frac	Micro-Frac	
Matrix	-	10^{-15}	10^{-14}	10^{-14}
Macro-Fracture	10^{-15}	-	10^{-17}	10^{-17}
Micro-Fracture	10^{-14}	10^{-14}	-	10^{-14}
Vug	10^{-14}	10^{-17}	10^{-14}	-

Other physical quantities used in this analysis are Q=10,000 STB/Day, well radius $r_w = r_i = 4''$, reservoir formation thickness $h = 200ft$, Moreover, it is assumed that the reservoir outer boundary $r_o \gg r_i$, in such a way that the reservoir is infinite acting. This assumption condenses the solution in Appendix D to the case, in which only modified Bessel function of 2nd kind are enough in expressing the field variables.

Results are shown in Figure 34, where plots of dimensionless pressure drop $\Delta p^* = \frac{(p \sum S_i)}{Q^*}$ vs. dimensionless time $t^* = \frac{t}{t_0}$ is sketched. The time scale $t_0 = \frac{R^2 \sum S}{\sum \kappa}$,

and $Q^* = \frac{Q}{(2V_w/t_0)}$, where $V_w = \pi {r_i}^2 h$ stands for the wellbore volume. A little elaboration on the matter of condensing the original quadruple-porosity model of rock to lower-level porosity models is needed here: At each row of graphs and pie charts in Figure 34, *m* colored curves corresponding to *m* porosity networks is shown. This row can be considered as a special case of the next row, by grouping selected porosity networks of higher level together.

Figure 33 shows the hierarchy of this analysis with indication of the lumped porosities at each level. On the lower segment of this figure, the problem of finding the intrinsic properties of the lumped porosity network is addressed, where its volume fraction, void ratio and effective permeability and bulk modulus should be found in terms of the same properties of the two corresponding porosities at higher hierarchical level. This task can be completed through the solution of following equations:

$$v_i^{m+1} + v_{i+1}^{m+1} = v_i^m \tag{4-3}$$

$$v_i^m \phi_i^m = v_i^{m+1} \phi_i^{m+1} + v_{i+1}^{m+1} \phi_{i+1}^{m+1} \tag{4-4}$$

$$\frac{v_i^m}{\bar{K}_i^m} = \frac{v_i^{m+1}}{\bar{K}_i^{m+1}} + \frac{v_i^{m+1}}{\bar{K}_i^{m+1}} \tag{4-5}$$

$$v_i^m \bar{k}_i^m = v_i^{m+1} \bar{k}_i^{m+1} + v_{i+1}^{m+1} \bar{k}_{i+1}^{m+1} \tag{4-6}$$

Equations (4-3) to (4-6) ensure that the mixture's effective porosity, void ratio, permeability and bulk modulus do not change when downgraded to a lower number of porosity networks.

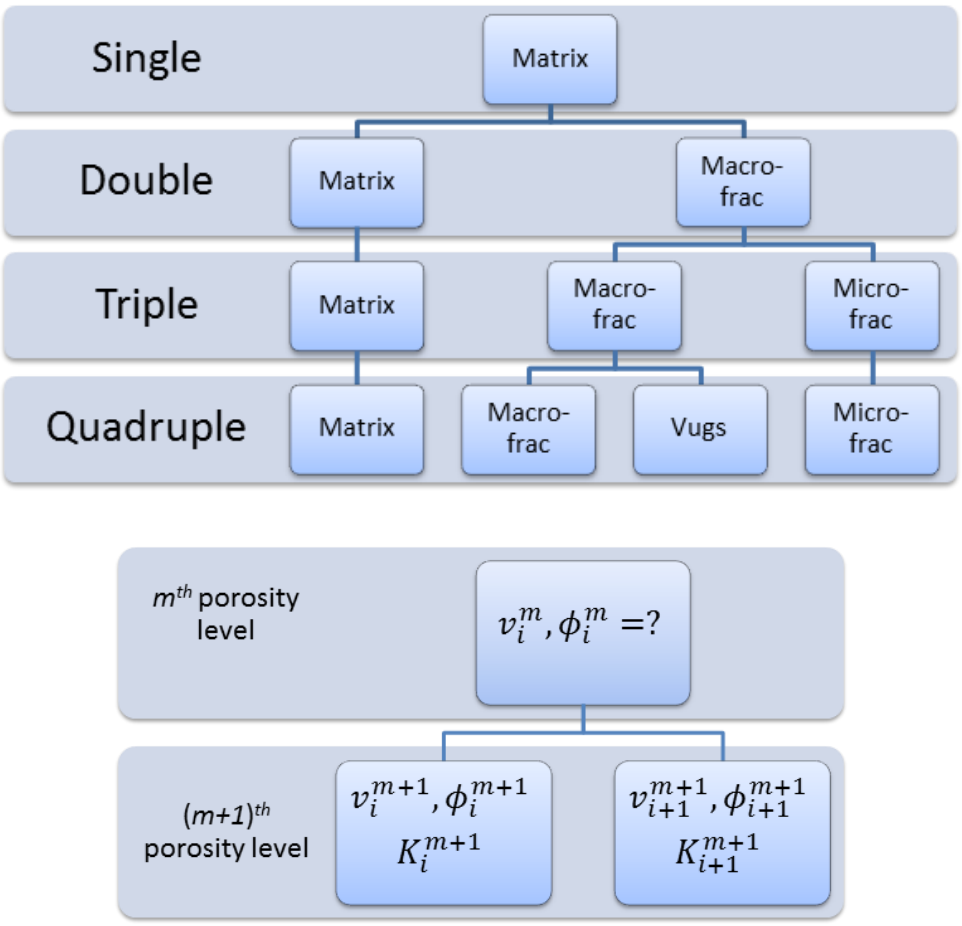

Figure 33. Hierarchy of porosity-levels in the analysis (top), and the problem of finding the intrinsic properties of the lumped porosity networks (bottom).

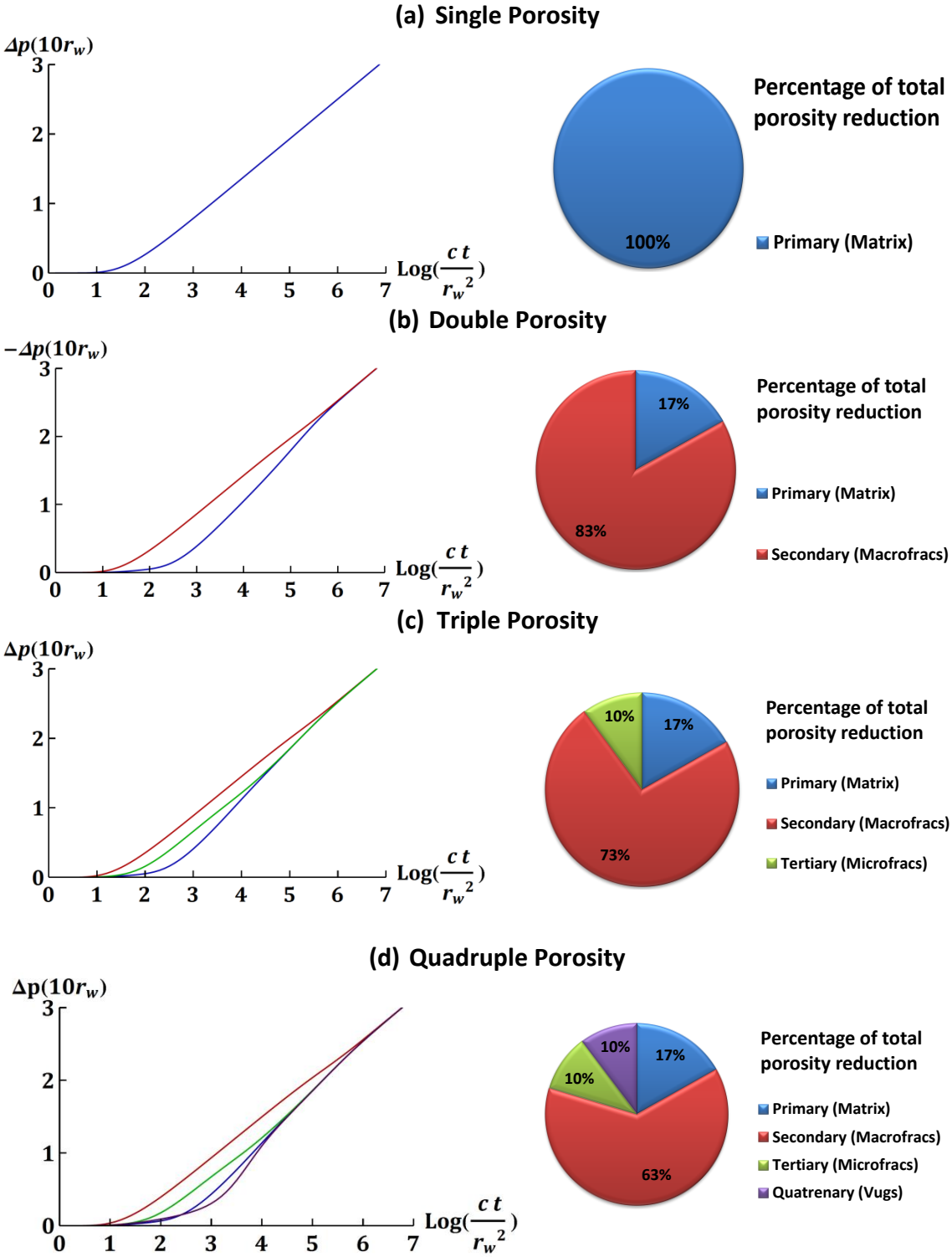

Figure 34. The pressure transients at $r = 10r_w$ (Left), and the porosity reduction ratio of multiple-porosity reservoir rocks (Right).

The pie charts in Figure 34 indicate that the contribution of the rock's matrix in supplying the driving energy to conduct fluid towards the wellbore does not decrease by increasing the number of considered porosity networks above $N = 2$. This observation is due to the fact that the effective properties are forced to remain constant through the hierarchy of suggested multiple-porosity model. Therefore, if the effective properties of the mixture are properly chosen, the lumped model is capable of returning accurate results regarding the pressure and compaction of reservoir and pseudo-steady state condition of depletion.

We also notice the Vugs response to the wellbore flow, which is the latest compared to the matrix and fractures. This is a reasonable observation since they are assumed to be not inter-connected, and therefore, only the pressure gradient with respect to other porosity networks may withdraw the trapped fluid from their pore space. However, once these gradients are established, vugs can be as effective in supplying the energy required for hydrocarbon flow, as an individual inter-connected fracture network. This conclusion is probably due to their relative high storage and assumed weak intrinsic mechanical properties. These findings indicate that in highly vuggy carbonate reservoirs, proper estimations of the vugs storage and their inter-exchange flow properties is crucial in evaluation and management of the reservoir's productivity index.

Figure 35 shows the total percentage of porosity reduction at each level of the reservoir's multiple-porosity modeling. It shows a significant contrast between the predictions given by the geomechanical model, and those obtained by solving the

uncoupled flow equations. However, when effective properties are used in flow equation, the models which incorporate lower number of porosity networks return excellent results compare to those predicted by models with higher number of porosity networks.

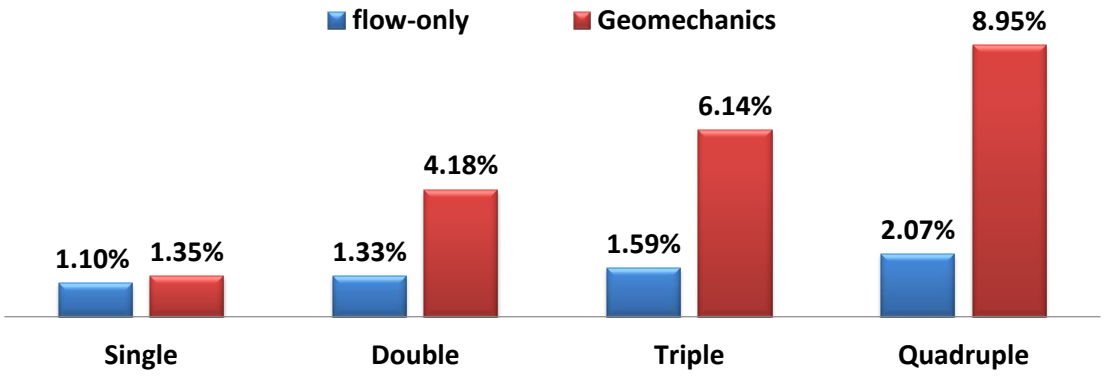

Figure 35. Percentage of porosity reduction, around wellbore after 2 years of production at $Q = 10,000$ STB/Day, when the original (intrinsic) properties of the constutents are used in the analysis.

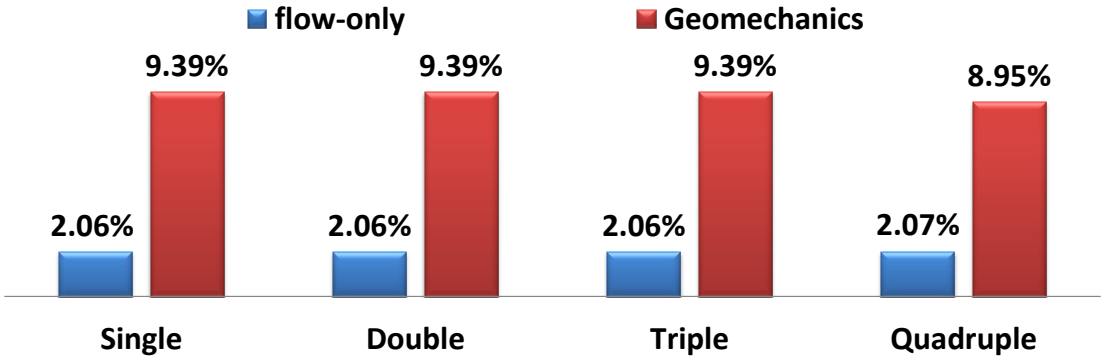

Figure 36. Percentage of porosity reduction, around wellbore after 2 years of production at $Q = 10,000$ STB/Day, when the effective properties of constituents in lower-level porosity models are used in the analysis.

4.3. Concluding remarks

This chapter presented two field applications of multiple-porosity and multiple-permeability poroelasticity theory that was developed earlier within this dissertation.

The transient pore pressure profiles due to a dual-porosity model of naturally fractured shale with hollow cylindrical geometry were obtained to investigate the caprock sealing capacity in maintaining the goe-sequestred CO_2 trap within the underlying saline aquifer. Also, properly selected combinations of normal and deviatory stress functions were used to represent the temporal variations of the state of stress within the caprock. Findings indicated that CO_2 diffusion into the caprock's pore space would increase both the mean and deviatory stresses with time. This result would, in effect, increase the chances of its failure.

A multiple-porosity/multiple-permeability model of compacting vuggy, dual fractured carbonate reservoir, under generalized plane strain condition of elastic deformation was developed further along this chapter. Results of the model solution were used to study the effect of increasing the number of the considered distinct porosity networks in the pore pressure profiles and compaction of the reservoir.

Chapter 5: Conclusions

This study finds in Biot's theory of poroelasticity a complete and consistent extension to the general case of homogeneous and isotropic multiple-porosity and multiple-permeability continua. The sequence of chapters within this dissertation introduced this extension; theoretically characterized a material identified with it; and formulated its constitutive model. Next, analytical solutions to a number of classical 2D problems of poroelasticity are upgraded to the case of this new theory. Lastly, a few related petroleum-industry applications of variations of these problems are addressed and analyzed.

Illustrative and elaborate presentations of chapters 2 and 3 attempted to explore the fundamental concepts underlying constitutive modeling of this theory. The overall approach in doing so is induction from the established constitutive relations of single and dual-porosity poroelasticity. However, deductive proof and reasoning is provided in cases where derivation of terms and equations were required. This approach led to a set of consistent constitutive relations for the case of multiple-porosity/multiple-permeability poroelasticity. Using this theory, a class of generalized plane-strain problems were solved and analyzed, farther along Chapter 3. Results of these solutions indicate that the hierarchy of porosity levels is self-multiplicative, in that the associated coupled flow-deformation phenomena in the case of single-porosity poroelasticity would reproduce and proliferate when upgraded to higher numbers of porosity networks.

The examples of Chapter 4 indicated the applicability of multi-poroelastic model in real-field petroleum-industry-related problems. The general conclusion is that neglecting or over-simplifying the complex effect of distinguishable pore structures within the rock matrix might produce errors which often tend to underestimate either the flow or deformation aspects of its response to the application of external stresses or pore pressure. In some other cases, on the other hand, such as evaluation of the porosity reduction and pore pressure of depleting reservoirs, findings of this study indicated that proper and consistent selection of effective properties of *lumped porosity models* can return practically accurate results.

4.1 Recommendations

Multiple-porosity/multiple-permeability poroelastic theory is developed on a dual-physics modeling basis, in that it considers mechanical deformations of the solid skeleton and pore fluid, as well as fluid flow and exchange through and between the distinguishable networks of porosity within a porous material. A natural extension would be its upgrade to a multi-physics theory, especially when it comes to a broader perspective of the exchange phenomena within the medium's pore structures. The mass and ions transfers associated with electrical (electrokinetic effects) and chemical (osmosis effects) activities of the fluid saturating the pore space, as well as the solid grains (adsorption and desorption effects), are good examples of these exchange phenomena.

As far as rheological modeling concerns, current theory of multi-poroelasticity considers a linearly elastic matrix. Hence, it can be improved to account for the effects

of viscous creep, or nonlinearities associated with plasticity or large deformations. This would be a pronounced improvement in the field of rocks mechanics, and more particularly in biomechanics, since soft tissues usually exhibit a nonlinear stress-strain behavior.

As per constitutive modeling, homogeneity and isotropy of substance were other fundamental assumptions throughout this dissertation. Relaxing either of the two would open gates to new and more challenging classes of problems which would indeed be capable of treating more realistic cases, such as transverse anisotropy of rocks or the effects of contrast in material properties between reservoir and burden rocks.

The analytical solutions presented throughout this dissertation were set in such a way that no shear deformation or stress would develop along the coordinate system which was selected in accord with the geometry and boundary conditions of the problem. This simplifying condition would not generally be the case, and in fact, can be relaxed to encounter a real 3D poroelastic problem. The consolidating reservoir problem in Chapter 4 is a good example, as in general, shear interactions between the reservoir and burden rocks are not negligible.

References

Abousleiman, Y., Cheng, A. D., Cui, L., Detournay, E., & Roegiers, J. C. (1996). Mandel's problem revisited. *Geotechnique*, *46*(2), 187-195.

Abousleiman, Y., & Cui, L. (1998). Poroelastic solutions in transversely isotropic media for wellbore and cylinder. *International journal of solids and structures*, *35*(34), 4905-4929.

Abousleiman, Y. N., & Kanj, M. Y. (2004). The generalized Lamé problem-Part II: Applications in poromechanics. *Journal of applied mechanics*, *71*(2), 180-189.

Abousleiman, Y., & Nguyen, V. (2005). PoroMechanics response of inclined wellbore geometry in fractured porous media. *Journal of engineering mechanics*, *131*(11), 1170-1183.

Aifantis, E. C. (1980). On Barenblatt's problem. *International Journal of Engineering Science*, *18*(6), 857-867.

Benalla, M., Cardoso, L., & Cowin, S. C. (2012). Analytical basis for the determination of the lacunar–canalicular permeability of bone using cyclic loading. *Biomechanics and modeling in mechanobiology*, *11*(6), 767-780.

Benson, S. M., & Cole, D. R. (2008). CO2 sequestration in deep sedimentary formations. *Elements*, *4*(5), 325-331.

Barenblatt, G. I., Zheltov, I. P., & Kochina, I. N. (1960). Basic concepts in the theory of seepage of homogeneous liquids in fissured rocks. *J. Appl. Math. Mech*, *24*(5), 1286-1303.

Berryman, J. G., & Wang, H. F. (1995). The elastic coefficients of double-porosity models for fluid transport in jointed rock. *JOURNAL OF GEOPHYSICAL RESEARCH-ALL SERIES-*, *100*, 24-24.

Berryman, J.G. & Berge, P. A. (1996). Critique of explicit schemes for estimating elastic properties of multiphase composites. *Mechanics of Materials*, *22*, 149-164.

Berryman, J. G., & Pride, S. R. (1998). Volume averaging, effective stress rules, and inversion for microstructural response of multicomponent porous media. *International journal of solids and structures*, *35*(34), 4811-4843.

Berryman, J. G. (1999). Origin of Gassmann's equations. *Geophysics*, *64*(5), 1627-1629.

Berryman, J. G. (2002). Extension of poroelastic analysis to double-porosity materials: new technique in microgeomechanics. *Journal of engineering mechanics*, *128*(8), 840-847.

Berryman, J. G., & Pride, S. R. (2002). Models for computing geomechanical constants of double-porosity materials from the constituents' properties. *Journal of geophysical research*, *107*(B3), 2052.

Berryman, J. G. (2006). Illustrations from: http://sepwww.stanford.edu/sep/berryman/porousmedia.html

Biot, M. A. (1941). General theory of three-dimensional consolidation. *Journal of applied physics*, *12*(2), 155-164.

Biot, M. A. (1955). Theory of elasticity and consolidation for a porous anisotropic solid. *Journal of Applied Physics*, *26*(2), 182-185.

Biot, M. A., & Willis, D. G. (1957). The elastic coefficients of the theory of consolidation. *J. appl. Mech*, *24*(594-601), 206.

Boresi, A. P. & Chong, K. P. (2000). Elasticity in engineering mechanics, 2nd Ed., Wiley-Interscience, NY.

Carlson, E., & Mercer, J. (1991). Devonian shale gas production: mechanisms and simple models. *Journal of Petroleum Technology*, *43*(4), 476-482.

Cheng, A. H., Sidauruk, P., & Abousleiman, Y. (1994). Approximate inversion of the Laplace transform. *Mathematica Journal*, *4*(2), 76-82.

Civan, F., Rai, C. S., & Sondergeld, C. H. (2011). Shale-gas permeability and diffusivity inferred by improved formulation of relevant retention and transport mechanisms. *Transport in Porous Media*, *86*(3), 925-944.

Cowin, S. C., Gailani, G., & Benalla, M. (2009). Hierarchical poroelasticity: movement of interstitial fluid between porosity levels in bones. *Philosophical Transactions of the Royal Society A: Mathematical, Physical and Engineering Sciences*, *367*(1902), 3401-3444.

Cryer, C. W. (1963). A comparison of the three-dimensional consolidation theories of Biot and Terzaghi. *The Quarterly Journal of Mechanics and Applied Mathematics*, *16*(4), 401-412.

Cui, L., Cheng, A. D., & Abousleiman, Y. (1997). Poroelastic solution for an inclined borehole. *Journal of applied mechanics*, *64*(1), 32-38.

Dehghanpour, H., & Shirdel, M. (2011, November). A Triple Porosity Model for Shale Gas Reservoirs. In *Canadian Unconventional Resources Conference*.

Dickey, J. W., Ladd, C. C., & Rixner, J. J. (1968). *Research in Earth Physics: Phase Report No. 10: a Plane Strain Shear Device for Testing Clays*. Waterways Experiment Station.

Edwards, C. H., Penny, D., E. (1996). Differential Equations and Boundary Value Problems, Prentice Hall.

Elsworth, D., & Bai, M. (1992). Flow-deformation response of dual-porosity media. *Journal of Geotechnical Engineering*, *118*(1), 107-124.

Geertsma, J. (1973). Land subsidence above compacting oil and gas reservoirs.*Journal of Petroleum Technology*, *25*(6), 734-744.

Gailani, G., & Cowin, S. (2011). Ramp loading in Russian doll poroelasticity. *Journal of the Mechanics and Physics of Solids*, *59*(1), 103-120.

Gibson, R. E., Knight, K., & Taylor, P. W. (1963). A critical experiment to examine theories of three-dimensional consolidation. In *Proceedings from the European Conference on Soil Mechanics and Foundation Engineering, Weisbaden, Germany*.

Hoang, S. K., & Abousleiman, Y. N. (2009). Poroviscoelastic two-dimensional anisotropic solution with application to articular cartilage testing. *Journal of engineering mechanics*, *135*(5), 367-374.

Hudson, J., Civan, F., Michel, G., Devegowda, D., & Sigal, R. (2012, April). Modeling Multiple-Porosity Transport in Gas-Bearing Shale Formations. In *SPE Latin America and Caribbean Petroleum Engineering Conference*.

Kanj, M. Y., & Abousleiman, Y. N. (2004). The generalized Lamé problem-Part I: Coupled poromechanical solutions. *Journal of applied mechanics*, *71*(2), 168-179.

Kemmere, M. F. & Meyer, T. (2006eds.). Supercritical carbon dioxide, Wiley-VCH.

Kim, J., Tchelepi, H., & Juanes, R. (2011). Stability, accuracy, and efficiency of sequential methods for coupled flow and geomechanics. *SPE Journal*, *16*(2), 249-262.

Mandel, J. (1953). Consolidation des sols (étude mathématique). *Géotechnique*, *3*, 287-299.

Mehrabian, A., & Abousleiman, Y. N. (2009). The dilative intake of poroelastic inclusions an alternative to the Mandel–Cryer effect. *Acta Geotechnica*, *4*(4), 249-259.

Nguyen, V., & Abousleiman, Y. (2009, October). Naturally Fractured Reservoir Three-Dimensional Analytical Modeling: Theory and Case Study. In *SPE Annual Technical Conference and Exhibition*.

Nguyen, V. X., & Abousleiman, Y. N. (2010). Poromechanics Solutions to Plane Strain and Axisymmetric Mandel-Type Problems in Dual-Porosity and Dual-Permeability Medium. *Journal of applied mechanics*, *77*(1).

Nguyen, V. X. (2010). Dual-porosity and dual-permeability poromechanics solutions

For problems in laboratory and field applications. PhD dissertation, Norman, Oklahoma.

Nowinski, J. L., & Davis, C. F. (1970). A model of the human skull as a poroelastic spherical shell subjected to a quasistatic load. *Mathematical Biosciences*, *8*(3), 397-416.

Ozkan, E., Raghavan, R., & Apaydin, O. (2010, September). Modeling of fluid transfer from shale matrix to fracture network. In SPE Annual *Technical Conference and Exhibition*.

Segall, P. (1992). Induced stresses due to fluid extraction from axisymmetric reservoirs. *Pure and Applied Geophysics*, *139*(3), 535-560.

Settari, A. T., Bachman, R. C., & Walters, D. A. (2005, October). How To Approximate Effects of Geomechanics in Conventional Reservoir Simulation. In*SPE Annual Technical Conference and Exhibition*.

Settari, A. (2002). Reservoir compaction. *Journal of petroleum technology*,*54*(8), 62-69.

Skempton, A. W. (1954). The pore-pressure coefficients A and B.*Geotechnique*.

Tully, B., & Ventikos, Y. (2011). Cerebral water transport using multiple-network poroelastic theory: application to normal pressure hydrocephalus. *Journal of Fluid Mechanics*, *667*, 188-215.

Vardakis, J. C., Tully, B. J., & Ventikos, Y. (2013). Multicompartmental Poroelasticity as a Platform for the Integrative Modeling of Water Transport in the Brain. *Computer Models in Biomechanics*, 305-316.

Verruijt, A. (1969). Elastic storage of aquifers. *Flow through porous media*, 331-376.

Wang, F., & Reed, R. (2009, October). Pore networks and fluid flow in gas shales. In *SPE Annual Technical Conference and Exhibition*.

Wang, H.F. (2000). Theory of Linear Poroelasticity with Applications to Geomechanics and Hydrogeology. Princeton University Press.

Warren, J. E., & Root, P. J. (1963). The behavior of naturally fractured reservoirs. *Old SPE Journal*, *3*(3), 245-255.

Appendix A: Complete Analytical Solutions to the Mandel-type and Cryer problems of multiple-porosity/multiple-permeability poroelasticity

This appendix completes the analytical solution to the two-dimensional problems addressed in Chapter 3. Its objective is to find the arbitrary function $f(t)$ through the condition of stress at the confined surface, i.e. $\sigma_{zz}(z=b)$ in Mandel-type problems and $\sigma_{rr}(r=1)$ in Cryer's problem.

A.1. Mandel's problem

It is easy to solve the stress equilibrium from Equation (3-8) as:

$$\sigma_{xx} = 0 \tag{A-1}$$

which by substitution from Equations (3-4) and (3-2) gives:

$$\varepsilon_{xx} = \left(\frac{c_{m1}\tilde{p}_1 + c_{m2}\tilde{p}_2}{S_1 + S_2}\right) - \tilde{f}\left(\frac{\nu}{1-2\nu}\right) \tag{A-2}$$

Because of the plane strain state of the problem, $\varepsilon_{zz} = \varepsilon - \varepsilon_{xx}$. That results in:

$$\tilde{\varepsilon}_{zz} = \tilde{f}\left(\frac{1-\nu}{1-2\nu}\right) \tag{A-3}$$

The vertical component of stress is consequently found as:

$$\tilde{\sigma}_{zz}(r) = \tilde{f}\left\{\frac{1}{\mathrm{Det}[\mathbf{X}]}\left[\sum_{i=1}^{N}\beta_i \mathrm{Det}[\mathbf{X}_{\psi,i}]\frac{\cosh\left(r\sqrt{\lambda_i}\right)}{\cosh\left(\sqrt{\lambda_i}\right)}\right] + \psi\right\} \tag{A-4}$$

where

$$\beta_i = \frac{\sum_{j=1}^{N}\chi_{ji}c_{mj}}{\sum_{j=1}^{N}S_j} \tag{A-5}$$

$$\psi = 1 + 2a_1 - \frac{\sum_{j=1}^{N}c_{mj}\psi_j}{\sum_{j=1}^{N}S_j} \tag{A-6}$$

The boundary condition at *z=b* reads:

$$\int_0^1 \tilde{\sigma}_{zz} dx = -\frac{P_c}{s} \tag{A-7}$$

Substitution from Equation (A-4) determines $\tilde{f}$ as follows:

$$\tilde{f} = -\frac{P_c \,\mathrm{Det}[\mathbf{X}]}{s\left[\psi \,\mathrm{Det}[\mathbf{X}] + \sum_{i=1}^{N} \frac{\beta_i \mathrm{Det}[\mathbf{X}_{\psi,i}] \tanh\left(\sqrt{\lambda_i}\right)}{\sqrt{\lambda_i}}\right]} \tag{A-8}$$

The pore pressure and vertical stress and strain would correspondingly be found as:

$$\frac{\tilde{p}_i(r)}{P_c} = \frac{-\,\mathrm{Det}[\mathbf{X}]\ \psi_i + \sum_{j=1}^{N} \chi_{ij} \mathrm{Det}[\mathbf{X}_{\psi,j}] \frac{\cosh\left(r\sqrt{\lambda_j}\right)}{\cosh\left(\sqrt{\lambda_j}\right)}}{2G(S_1+S_2)s\left[\psi \,\mathrm{Det}[\mathbf{X}] + \sum_{i=1}^{N} \frac{\beta_i \mathrm{Det}[\mathbf{X}_{\psi,i}] \tanh\left(\sqrt{\lambda_i}\right)}{\sqrt{\lambda_i}}\right]} \tag{A-9}$$

$$\frac{\tilde{\sigma}(r)}{P_c} = -\frac{\mathrm{Det}[\mathbf{X}]\ \psi + \sum_{i=1}^{N} \beta_i \mathrm{Det}[\mathbf{X}_{\psi,i}] \frac{\cosh\left(r\sqrt{\lambda_i}\right)}{\cosh\left(\sqrt{\lambda_i}\right)}}{s\left[\mathrm{Det}[\mathbf{X}]\,\psi + \sum_{i=1}^{N} \frac{\beta_i \mathrm{Det}[\mathbf{X}_{\psi,i}] \tanh\left(\sqrt{\lambda_i}\right)}{\sqrt{\lambda_i}}\right]} \tag{A-10}$$

$$\frac{2G\tilde{u}_z(b)}{P_c b} = -\frac{\mathrm{Det}[\mathbf{X}]}{s\left[\psi \,\mathrm{Det}[\mathbf{X}] + \sum_{i=1}^{N} \frac{\beta_i \mathrm{Det}[\mathbf{X}_{\psi,i}] \tanh\left(\sqrt{\lambda_i}\right)}{\sqrt{\lambda_i}}\right]} \tag{A-11}$$

A.2. Axisymmetric Mandel's problem

This problem can be solved in a manner similar to the presentations of section A.2, with the exception that here, the variations of the radial hoop stresses along the radial dimension should be considered, as well. Since $= \frac{1}{r}\frac{\partial}{\partial r}\left(r\frac{\partial u_r}{\partial r}\right) + \varepsilon_{zz}$, The radial strain by substitution from Equation (3-4) can be written as:

$$\tilde{\varepsilon}_{rr} = -\frac{1}{r^2}\int\left(\frac{\sum_{i=1}^{N} c_{mi}\tilde{p}_i}{\sum_{i=1}^{N} S_i}\right) r dr + \frac{\tilde{f} - \tilde{\varepsilon}_{zz}}{2} + \frac{\sum_{i=1}^{N} c_{mi}\tilde{p}_i}{\sum_{i=1}^{N} S_i} \tag{A-12}$$

Substitution into Equation (3-4) for radial component of stress gives:

$$\tilde{\sigma}_{rr} = -\frac{1}{r^2}\int\left(\frac{\sum_{i=1}^{N} c_{mi}\tilde{p}_i}{\sum_{i=1}^{N} S_i}\right) r dr + \tilde{f}\left(a_1 + \frac{1}{2}\right) - \frac{\tilde{\varepsilon}_{zz}}{2} \tag{A-13}$$

Solution of Equation (A-11) for $\tilde{\varepsilon}_{zz}$ at the free surface boundary $\sigma_{rr}(1,t) = 0$ determinesε_{zz} as:

$$\tilde{\varepsilon}_{zz} = -\tilde{f}\left[1 + 2a_1 - \frac{\sum_{i=1}^{N} c_{mi}\psi_i}{\sum_{i=1}^{N} S_i} - \frac{2}{\mathrm{Det}[\mathbf{X}]}\sum_{i=1}^{N}\frac{\beta_i \mathrm{Det}[\mathbf{X}_{\psi,i}]\,\mathrm{I}_1\left(\sqrt{\lambda_i}\right)}{\sqrt{\lambda_i}\,\mathrm{I}_0\left(\sqrt{\lambda_i}\right)}\right] \tag{A-14}$$

Likewise, the vertical component of stress σ_{zz} is found from Equations (3-4) and (3-2) as:

$$\tilde{\sigma}_{zz} = -\tilde{f}\left\{\psi' + \frac{1}{\mathrm{Det}[\mathbf{X}]}\sum_{i=1}^{N}\beta_i \mathrm{Det}[\mathbf{X}_{\psi,i}]\left[\frac{\mathrm{I}_0\left(r\sqrt{\lambda_i}\right) + 2\,\mathrm{I}_1\left(\sqrt{\lambda_i}\right)}{\sqrt{\lambda_i}\,\mathrm{I}_0\left(\sqrt{\lambda_i}\right)}\right]\right\} \tag{A-15}$$

Where β_i is introduced in Equation (A-5) and ψ' is defined as:

$$\psi' = 1 + 3a_1 - 2\frac{\sum_{i=1}^{N} c_{mi}\psi_i}{\sum_{i=1}^{N} S_i} \tag{A-16}$$

The following condition should hold at the upper boundary of cylinder:

$$\int_0^1 \tilde{\sigma}_{zz} r dr = -\frac{P_c}{2s} \tag{A-17}$$

Substitution from Equation (A-15) determines $\tilde{f}$ as follows:

$$\tilde{f} = -\frac{P_c \mathrm{Det}[\mathbf{X}]}{s\left\{\psi' \mathrm{Det}[\mathbf{X}] + 4\sum_{i=1}^{N} \frac{\beta_i \mathrm{Det}[\mathbf{X}_{\psi,i}]\, \mathrm{I}_1\left(\sqrt{\lambda_i}\right)}{\sqrt{\lambda_i}\, \mathrm{I}_0\left(\sqrt{\lambda_i}\right)}\right\}} \tag{A-18}$$

The pore pressure and vertical stress and strain would subsequently be found as:

$$\frac{\tilde{p}_i(r)}{P_c} = \frac{-\mathrm{Det}[\mathbf{X}]\ \psi_i + \sum_{j=1}^{N}\left\{\chi_{ij}\mathrm{Det}[\mathbf{X}_{\psi,j}]\frac{\mathrm{I}_0\left(r\sqrt{\lambda_j}\right)}{\mathrm{I}_0\left(\sqrt{\lambda_j}\right)}\right\}}{2G(S_1+S_2)s\left\{\mathrm{Det}[\mathbf{X}]\,\psi' + 4\sum_{i=1}^{N}\left\{\beta_i \mathrm{Det}[\mathbf{X}_{\psi,i}]\frac{\mathrm{I}_1\left(\sqrt{\lambda_i}\right)}{\mathrm{I}_0\left(\sqrt{\lambda_i}\right)}\right\}\right\}} \tag{A-19}$$

$$\frac{\tilde{\sigma}_{zz}(r)}{P_c} = -\frac{\left\{\mathrm{Det}[\mathbf{X}]\,\psi' + \sum_{i=1}^{N}\beta_i \mathrm{Det}[\mathbf{X}_{\psi,i}]\frac{\mathrm{I}_0\left(r\sqrt{\lambda_i}\right) + \frac{2\mathrm{I}_1\left(\sqrt{\lambda_i}\right)}{\sqrt{\lambda_i}}}{\mathrm{I}_0\left(\sqrt{\lambda_i}\right)}\right\}}{s\left\{\mathrm{Det}[\mathbf{X}]\,\psi' + 4\sum_{i=1}^{N}\left\{\beta_i \mathrm{Det}[\mathbf{X}_{\psi,i}]\frac{\mathrm{I}_1\left(\sqrt{\lambda_i}\right)}{\mathrm{I}_0\left(\sqrt{\lambda_i}\right)}\right\}\right\}} \tag{A-20}$$

$$\frac{2G\tilde{u}_z(b)}{P_c b} = -\frac{\mathrm{Det}[\mathbf{X}]\ \psi + 2\sum_{i=1}^{N}\left\{\beta_i \mathrm{Det}[\mathbf{X}_{\psi,i}]\frac{\mathrm{I}_1\left(\sqrt{\lambda_i}\right)}{\mathrm{I}_0\left(\sqrt{\lambda_i}\right)}\right\}}{s\left\{\mathrm{Det}[\mathbf{X}]\,\psi' + 4\sum_{i=1}^{N}\left\{\beta_i \mathrm{Det}[\mathbf{X}_{\psi,i}]\frac{\mathrm{I}_1\left(\sqrt{\lambda_i}\right)}{\mathrm{I}_0\left(\sqrt{\lambda_i}\right)}\right\}\right\}} \tag{A-21}$$

A.3. Cryer's problem

Because of the spherical symmetry, u_r is the single nonzero component of displacement field. Hence, one can write:

$$u_r(r,t) = \frac{1}{r^2}\int_0^r x^2 \varepsilon(x,t)dx \tag{A-22}$$

Substitution from Equation (3-4) gives:

$$\tilde{u}_r(r) = \sum_{i=1}^{N} \frac{\beta_i A_i(s) \mathrm{g}\left(r\sqrt{\lambda_i}\right)}{r^2 \lambda_i} + \psi''' \tilde{f} r \tag{A-23}$$

Where the new function g and parameter ψ''' are defined as:

$$\mathrm{g}(x) = x\cosh x - \sinh x \tag{A-24}$$

$$\psi''' = \frac{1}{3}\left(1 + \frac{\sum_{j=1}^{N} c_{mj}\psi_j}{\sum_{j=1}^{N} S_i}\right) \tag{A-25}$$

The radial component of stress scaled by the parameter $2G$ can be found from the appropriate constitutive equation as shown below:

$$\frac{\sigma_{rr}}{2G} = \frac{\partial u_r}{\partial r} + \frac{\nu}{1-2\nu}\varepsilon - \frac{\sum_{i=1}^{N} \alpha_i p_i}{2G\sum_{j=1}^{N} S_i} \tag{A-26}$$

Substitution of equations (3-2) and (A-23) into equation (A-24) yields:

$$\frac{\sigma_{rr}}{2G} = -\frac{2u_r}{r} + f\frac{(1-\nu)}{(1-2\nu)} \tag{A-27}$$

By substitution from Equation (A-23), the condition of confining normal traction at the sphere's surface $\sigma_{rr}(1,t) = -P_c$ gives:

$$A_i = \frac{P_c}{s} \cdot \frac{\mathrm{Det}\left[\mathbf{X}_{\psi,j}\right]}{\sinh\sqrt{\lambda_i}\left\{\sum_{j=1}^{N}\left\{\frac{2\beta_j^* \mathrm{Det}\left[\mathbf{X}_{\psi,j}\right] g\left(\sqrt{\lambda_j}\right)}{\lambda_j \sinh\sqrt{\lambda_j}}\right\} + \psi^* \mathrm{Det}[\mathbf{X}]\right\}} \tag{A-28}$$

$$\tilde{f} = -\frac{P_c}{s} \cdot \frac{\mathrm{Det}[\mathbf{X}]}{\sum_{j=1}^{N}\left\{\frac{2\beta_j^* \mathrm{Det}\left[\mathbf{X}_{\psi,j}\right] g\left(\sqrt{\lambda_j}\right)}{\lambda_j \sinh\sqrt{\lambda_j}}\right\} + \psi^* \mathrm{Det}[\mathbf{X}]} \tag{A-29}$$

The pressure, stress and displacement terms would correspondingly be found as:

$$\frac{\tilde{p}_i(r)}{P_c} = \frac{-\,\mathrm{Det}[\mathbf{X}]\;\psi_i + \sum_{j=1}^{N}\left\{\chi_{ij}\mathrm{Det}[\mathbf{X}_{\psi,j}]\,\dfrac{\sinh\left(r\sqrt{\lambda_j}\right)}{r\sinh\left(\sqrt{\lambda_j}\right)}\right\}}{2G(S_1+S_2)s\left\{\mathrm{Det}[\mathbf{X}]\,\psi'' + 2\sum_{i=1}^{N}\left\{\beta_i\mathrm{Det}[\mathbf{X}_{\psi,i}]\,\dfrac{\mathrm{g}\left(\sqrt{\lambda_i}\right)}{\lambda_i\sinh\left(\sqrt{\lambda_i}\right)}\right\}\right\}} \tag{A-30}$$

$$\frac{\tilde{\sigma}_{zz}(r)}{P_c} = -\frac{\left\{\mathrm{Det}[\mathbf{X}]\,\psi'' + \dfrac{2}{r^3}\cdot\sum_{i=1}^{N}\beta_i\mathrm{Det}[\mathbf{X}_{\psi,i}]\,\dfrac{\mathrm{g}\left(r\sqrt{\lambda_i}\right)}{\lambda_i\sinh\left(\sqrt{\lambda_i}\right)}\right\}}{s\left\{\mathrm{Det}[\mathbf{X}]\,\psi'' + 2\sum_{i=1}^{N}\left\{\beta_i\mathrm{Det}[\mathbf{X}_{\psi,i}]\,\dfrac{\mathrm{g}\left(\sqrt{\lambda_i}\right)}{\lambda_i\sinh\left(\sqrt{\lambda_i}\right)}\right\}\right\}} \tag{A-31}$$

$$\frac{2G\tilde{u}_r(r)}{P_c} = \frac{-\,\mathrm{Det}[\mathbf{X}]\;\psi'''r + \dfrac{1}{r^2}\cdot\sum_{i=1}^{N}\beta_i\mathrm{Det}[\mathbf{X}_{\psi,i}]\,\dfrac{\mathrm{g}\left(r\sqrt{\lambda_i}\right)}{\lambda_i\sinh\left(\sqrt{\lambda_i}\right)}}{s\left\{\mathrm{Det}[\mathbf{X}]\,\psi'' + 2\sum_{i=1}^{N}\left\{\beta_i\mathrm{Det}[\mathbf{X}_{\psi,i}]\,\dfrac{\mathrm{g}\left(\sqrt{\lambda_i}\right)}{\lambda_i\sinh\left(\sqrt{\lambda_i}\right)}\right\}\right\}} \tag{A-32}$$

Appendix B: Analytical vis-à-vis numerical inversion of Laplace transform

The radial displacement and stress, as well as the pore pressure in the single porosity Cryer's problem can be written in Laplace space as:

$$\tilde{u}_r(r,s) = \frac{BP_c}{\Delta_1(s)}\left[\beta\frac{g\left(r\sqrt{s}\right)}{r^2 s} + (1-\beta)\frac{r\sinh\left(\sqrt{s}\right)}{3}\right] \tag{B-1}$$

$$\tilde{\sigma}_{rr}(r,s) = \frac{P_c}{\Delta_1(s)}\left[-2Bc_m^*\frac{g\left(r\sqrt{s}\right)}{r^3 s} + \sinh\left(\sqrt{s}\right)\right] \tag{B-2}$$

$$\tilde{p}(r,s) = \frac{BP_c}{\Delta_1(s)}\left[\frac{\sinh\left(r\sqrt{s}\right)}{r} - \sinh\left(\sqrt{s}\right)\right] \tag{B-3}$$

in which the denominator $\Delta_1(s)$ reads:

$$\Delta_1(s) = 2Bc_m^* g\left(\sqrt{s}\right) - s\sinh\left(\sqrt{s}\right) \tag{B-4}$$

or equivalently:

$$\Delta_1(s) = a_1\sqrt{s}\cosh\left(\sqrt{s}\right) - (a_1 + s)\sinh\left(\sqrt{s}\right) \tag{B-5}$$

The constants $2Bc_m^*$ and β can be written in terms of drained and undrained Poisson ratios as follows:

$$a_1 = 2Bc_m^* = \frac{6(\nu_u - \nu)}{(1-\nu)(1+\nu_u)} \tag{B-6}$$

$$\beta = \frac{(\nu_u - \nu)}{(1-2\nu)(1-\nu_u)} \tag{B-7}$$

It should be noted that letting ($\nu_u = 0.5, B = 1$) which corresponds to the poroelastic constants of a matrix with incompressible constituents, simplifies equations and (B-1) to (B-3) to equations (4-9) and (4-10) in the Cryer's original paper.

The inverse Laplace transform can be analytically obtained from the following Bromwich integral:

$$Q(r,t) = \int_{\chi-i\infty}^{\chi+i\infty} \tilde{Q}(r,s)e^{st}ds \qquad \text{(B-8)}$$

χ in equation (B-8) is a constant greater than the real part of all singularities of $\tilde{Q}(r,s)$, and the integral can correspondingly be found by summing the residues at all poles of the integrand after completing the large semi-circular contour which encloses the *x*<0 half-space ($s = x + iy$). For the particular field variables being investigated in this problem, the poles on negative real axis are the roots of $\Delta_1(s)$ from equation (B-5), which after the application of some hyperbolic trigonometric identities can be demonstrated as positive roots s_n of the following equation:

$$\Delta(s_n) = a_1\sqrt{s_n}\cos\left(\sqrt{s_n}\right) - (a_1 - s_n)\sin\left(\sqrt{s_n}\right) = 0 \qquad s_n > 0 \qquad \text{(B-9)}$$

A plot of Δ(s) is shown in Figure 37 with positive roots demonstrated on the horizontal axis.

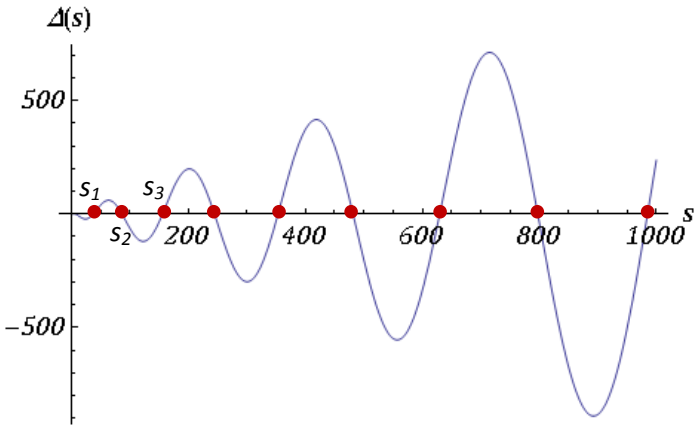

Figure 37. Plot showing the positive roots of Δ(s).

Henceforth, the corresponding time domain expressions for radial displacement and stress as well as the pore pressure can be written as:

$$\frac{2G\tilde{u}_r(r,s)}{P_c} = \sum_{n=1}^{\infty} \frac{\left\{ra_3 \sin\left(\sqrt{s_n}\right) - \frac{a_1}{2r^2 s}\left[r\sqrt{s_n}\cos\left(r\sqrt{s_n}\right) - \sin\left(r\sqrt{s_n}\right)\right]\right\}}{\Delta'(s_n)} \cdot e^{-s_n t} \tag{B-10}$$

$$\frac{\tilde{\sigma}_{rr}(r,s)}{P_c} = \sum_{n=1}^{\infty} \frac{\left\{\sin\left(\sqrt{s_n}\right) + \frac{a_1}{r^3 s}\left[r\sqrt{s_n}\cos\left(r\sqrt{s_n}\right) - \sin\left(r\sqrt{s_n}\right)\right]\right\}}{\Delta'(s_n)} \cdot e^{-s_n t} \tag{B-11}$$

$$\frac{\tilde{p}(r,s)}{BP_c} = \sum_{n=1}^{\infty} \frac{\left\{\frac{\sin\left(r\sqrt{s_n}\right)}{r} - \sin\left(\sqrt{s_n}\right)\right\}}{\Delta'(s_n)} \cdot e^{-s_n t} \tag{B-12}$$

where, new constant a_2 is defined as a consequence of rescaling the external load P_c with $2G$ as follows:

$$a_2 = \frac{1 - 2\nu_u}{1 + \nu_u} \tag{B-13}$$

Although analytically accurate expressions, equations (B-10) to (B-12) would cause computational difficulties and especially for small-time solutions require calculation of excessive number of terms in order to secure the series convergence. For this reason, a numerical method adopted from Stehfest (Cheng *et al*. 1994) is introduced here. The Stehfest formula is defined as:

$$f(t) = \frac{\ln 2}{t} \sum_{n=1}^{N} X_n \cdot \tilde{f}\left(\frac{n \ln 2}{t}\right) \tag{B-14}$$

with the coefficient X_n given by

$$X_n = (-1)^{n+\frac{N}{2}} \sum_{j=\text{Floor}\left[\frac{n+1}{2}\right]}^{\min(n,\frac{N}{2})} \frac{j^{N/2}(2j)!}{\left(\frac{N}{2}-j\right)!\,(j-1)!\,(n-j)!\,(2j-n)!} \qquad \text{(B-15)}$$

The number of terms N in the series is even and a selection of $N > 8$ generally returns satisfactory results.

Fig. 1.2 shows the variations of radial stress and pore pressure scaled by P_c at r=0.5 with time for a set of material properties (v=0.2,v_u=0.4,B=0.9). The dashed curves correspond to the analytical solution, where the well-known Mandel-Cryer effect can be observed via their overshoot within the range of the system's characteristic diffusive time. The solid curves are obtained through Stehfest formula, showing that selection of N = 8 in equation (B-14) would return accurate approximations to the analytical time-domain solution.

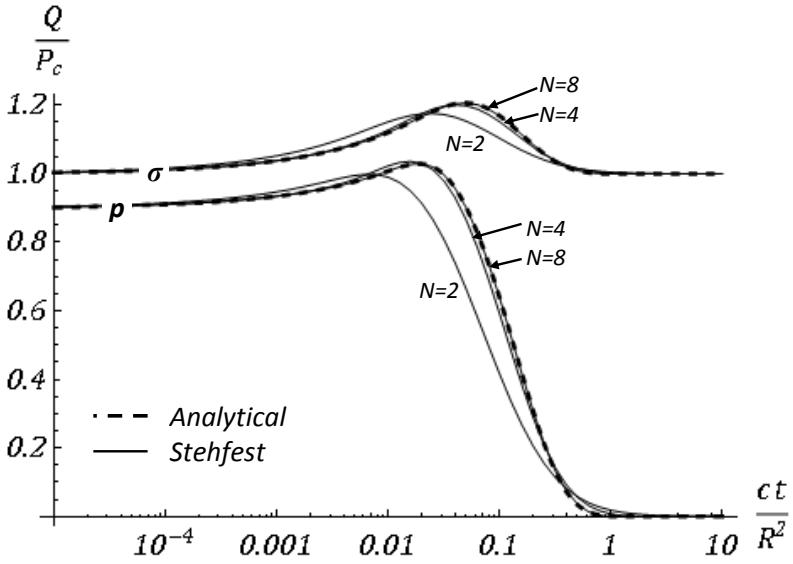

Figure 38. Stress and pore pressure at r=0.5 vs. time.

Appendix C: Dual-Porosity/dual-permeability poroelasticity of an internally pressurized hollow sphere

This Appendix is aimed to treat the problem of a dual-porous/dual-permeable poroelastic hollow sphere, simulating the geomechanics of a spherical shell of caprock which is subjected to internal pressure due to CO_2 injection inside its underlying saline aquifer formation. The boundary conditions adapted to this problem are shown in Figure 39.

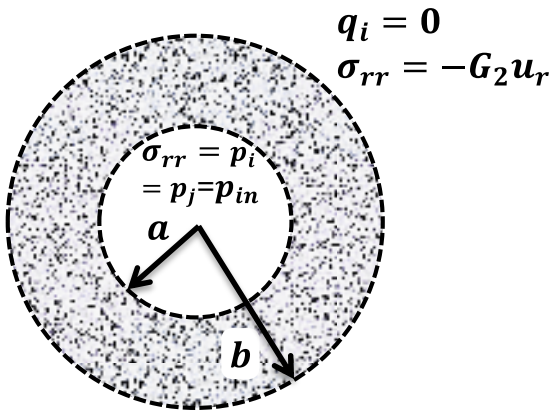

Figure 39. Poroelastic Hollow sphere, adapted to the caprock sealing integrity problem.

The mathematical solution to this problem follows the formulations of Chapter 3. However, because of the presence of a cavity, both Sturm-Liouvill functions of type 1 and 2 should be used here. Therefore, the general solution can be restated in the following form:

$$\tilde{p}_1(r) = \frac{A_1 \sinh\left(r\sqrt{\lambda_1}\right)}{r} + \frac{A_2 \sinh\left(r\sqrt{\lambda_2}\right)}{r} + \frac{B_1 \cosh\left(r\sqrt{\lambda_1}\right)}{r} + \frac{B_2 \cosh\left(r\sqrt{\lambda_2}\right)}{r} + \psi_1 \tilde{f}_1 \quad \text{(C-1)}$$

$$\tilde{p}_2(r) = \frac{A_1\,\chi_1 \sinh\left(r\sqrt{\lambda_1}\right)}{r} + \frac{A_2\,\chi_2\,\sinh\left(r\sqrt{\lambda_2}\right)}{r} + \frac{B_1\chi_1\,\cosh\left(r\sqrt{\lambda_1}\right)}{r} + \frac{B_2\chi_2\,\cosh\left(r\sqrt{\lambda_2}\right)}{r} + \psi_2\tilde{f}_1 \tag{C-2}$$

where, A_1, A_2, B_1, B_2 are the arbitrary functions of the solution. Without loss of generality, it is assumed that $\chi_{11} = \chi_{12} = 1$, while χ_{21}, χ_{22} are replaced by χ_1, χ_2, respectively. The expressions for radial displacement, stress, and the flux of each porosity network can then be written as:

$$\tilde{u}_r(r) = \frac{1}{r^2}\left[\frac{\beta_1 A_1 \mathrm{g}_1\left(r\sqrt{\lambda_1}\right)}{\lambda_1} + \frac{\beta_2 A_2 \mathrm{g}_1\left(r\sqrt{\lambda_2}\right)}{\lambda_2} + \frac{\beta_1 B_1 \mathrm{g}_2\left(r\sqrt{\lambda_1}\right)}{\lambda_1} + \frac{\beta_2 B_2 \mathrm{g}_2\left(r\sqrt{\lambda_2}\right)}{\lambda_2} + \tilde{f}_2\right] + \frac{\tilde{f}_1 r}{3}(1+\psi) \tag{C-3}$$

$$\tilde{\sigma}_r(r) = \tilde{f}_1\psi^* - \frac{2\theta}{r^3}\left[\frac{\beta_1 A_1 \mathrm{g}_1\left(r\sqrt{\lambda_1}\right)}{\lambda_1} + \frac{\beta_2 A_2 \mathrm{g}_1\left(r\sqrt{\lambda_2}\right)}{\lambda_2} + \frac{\beta_1 B_1 \mathrm{g}_2\left(r\sqrt{\lambda_1}\right)}{\lambda_1} + \frac{\beta_2 B_2 \mathrm{g}_2\left(r\sqrt{\lambda_2}\right)}{\lambda_2} + \tilde{f}_2\right] \tag{C-4}$$

$$\tilde{q}_1(r) = -\kappa_1\left[\frac{A_1 \mathrm{g}_1\left(r\sqrt{\lambda_1}\right)}{\lambda_1} + \frac{A_2 \mathrm{g}_1\left(r\sqrt{\lambda_2}\right)}{\lambda_2} + \frac{B_1 \mathrm{g}_2\left(r\sqrt{\lambda_1}\right)}{\lambda_1} + \frac{B_2 \mathrm{g}_2\left(r\sqrt{\lambda_2}\right)}{\lambda_2}\right] \tag{C-5}$$

$$\tilde{q}_2(r) = -\kappa_2\left[\frac{A_1\chi_1 \mathrm{g}_1\left(r\sqrt{\lambda_1}\right)}{\lambda_1} + \frac{A_2\chi_2 \mathrm{g}_1\left(r\sqrt{\lambda_2}\right)}{\lambda_2} + \frac{B_1\chi_1 \mathrm{g}_2\left(r\sqrt{\lambda_1}\right)}{\lambda_1} + \frac{B_2\chi_2 \mathrm{g}_2\left(r\sqrt{\lambda_2}\right)}{\lambda_2}\right] \tag{C-6}$$

where, f_2 is a new function of integration. Parameters $\beta 1, \beta 2, \psi$ are given in equations to, and functions g_1 , g_2 are defined as:

$$g_1(x) = x\cosh x - \sinh x \quad \text{(C-7)}$$

$$g_2(x) = x\sinh x - \cosh x \quad \text{(C-8)}$$

The following conditions hold at the sphere's inner boundaries:

$$\sigma_{rr}(a,t) = -P_{in}H(t) \quad \text{(C-9)}$$

$$p_1(a,t) = P_{in}\,H(t) \quad \text{(C-10)}$$

$$p_2(a,t) = P_{in}H(t) \quad \text{(C-11)}$$

while the impermeability of the outer boundary implies:

$$q_2(1,t) = 0 \quad \text{(C-12)}$$

$$q_2(1,t) = 0 \quad \text{(C-13)}$$

The interaction between the burden and caprocks can be formulated via the following equation, which can be simply deduced form an elastic solution for the deformations of burden rock:

$$\sigma_{rr}(1,t) + 2\gamma u_r(1,t) = 0 \quad \text{(C-14)}$$

where $\gamma = 2\,(S_1 + S_2)\cdot(G_2/G_1)$ is a measure of the contrast between the burden and caprock's contrast in mechanical moduli. The set of equations (C-9) to (C-14) generate a system of six linear algebraic equations which can be solve for the arbitrary function of the solution $A_1, A_2, B_1, B_2, f_1, f_2$ as follows:

$$\tilde{f}_1 = \frac{\delta_2[a^2\lambda_1\lambda_2(\chi_2-\chi_1) + 2\beta_1\lambda_2\theta(\chi_2-1)g_3(\lambda_1) - 2\beta_2\lambda_1\theta(\chi_1-1)\lambda_1 g_3(\lambda_2)]}{s\{\delta_1\lambda_1\lambda_2(\chi_1-\chi_2) + 2\delta_2[\beta_1\lambda_2(\chi_2\psi_1-\psi_2)g_3(\lambda_1) + \beta_2\lambda_1(-\chi_1\psi_1+\psi_2)g_3(\lambda_2)]} \quad \text{(C-15)}$$

$$\tilde{f}_2 = -\frac{a\theta[2\gamma(1+\psi)+3\psi^*]}{2\delta_2}\tilde{f}_1 \tag{C-16}$$

$$A_1 = \frac{a\mathrm{g}_2(\lambda_1)\left[s\tilde{f}_1(-\chi_2\psi_1+\psi_2)+(\chi_2-1)\right]}{s(\chi_1-\chi_2)\left\{\sqrt{\lambda_1}\cosh\left[\sqrt{\lambda_1}(1-a)\right]-\sinh\left[\sqrt{\lambda_1}(1-a)\right]\right\}} \tag{C-17}$$

$$A_2 = \frac{a\mathrm{g}_2(\lambda_2)\left[s\tilde{f}_1(-\chi_1\psi_1+\psi_2)-(\chi_1-1)\right]}{s(\chi_1-\chi_2)\left\{\sqrt{\lambda_2}\cosh\left[\sqrt{\lambda_2}(1-a)\right]-\sinh\left[\sqrt{\lambda_2}(1-a)\right]\right\}} \tag{C-18}$$

$$B_1 = -\frac{\mathrm{g}_1(\lambda_1)}{\mathrm{g}_2(\lambda_1)}A_1 \tag{C-19}$$

$$B_2 = -\frac{\mathrm{g}_1(\lambda_2)}{\mathrm{g}_2(\lambda_2)}A_2 \tag{C-20}$$

Where,

$$\delta_1 = 2\gamma\theta(1+\psi)+3a^3\gamma\psi^*+3(1-a^3)\theta\psi^* \tag{C-21}$$

$$\delta_2 = 3a\theta(\gamma-\theta) \tag{C-22}$$

and the function g_3 is defined as:

$$\mathrm{g}_3(x) = (1-a)+\frac{a(x-1)}{1+\sqrt{x}\coth\left[\sqrt{x}(1-a)\right]} \tag{C-23}$$

Appendix D: Multiple-porosity/multiple-permeability poroelasticity of hollow cylinder

The general boundary conditions of the hollow cylinder problem presented in Table 1, incorporate a Mandel-type confining stress $2P_c$ on the top and presumed flow or pressure at the inner and outer sides of the cylinder, as shown below:

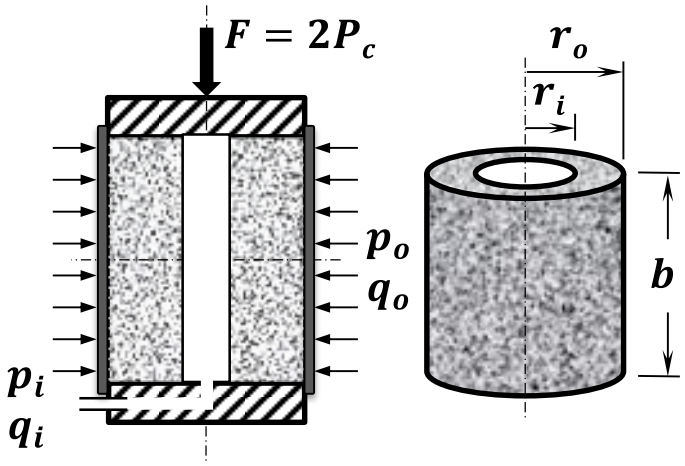

Figure 40. Poroelastic hollow cylinder problem.

Owing to the assumption of linearity in constitutive relations, this problems can be decomposed in two sub-problems, each of which treating either the confining stress or pressure/flow problem, separately. This appendix is aimed to treat the general multi-porosity/multi-permeability of the latter sub-problem with the mixed pressure/flow boundary conditions, as shown below:

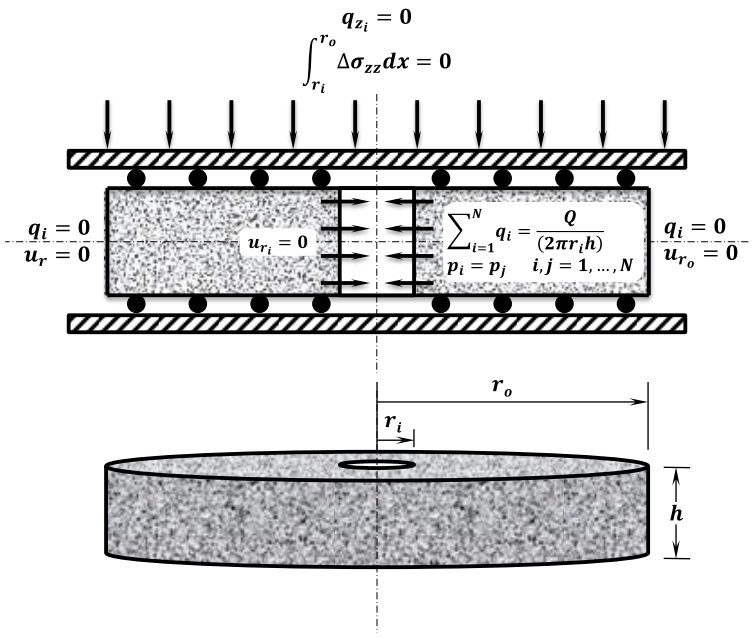

Figure 41. Modified Hollow poroelastic cylinder problem with pressure and flow boundary conditions customized for geomechanical simulation of an axisymmetric reservoir.

It is designed for geomechanical simulation of a compacting reservoir of outer radius r_o undergoing hydrocarbon production from a wellbore of radius $r_w = r_i$ at the center. The methodology taken in Chapter 3 can be used for solving this problem, starting with the general solution of pore pressure given in Equation (3-15), as follows:

$$\tilde{\mathbf{p}}(r) = \begin{pmatrix} \chi_{11} & \chi_{12} & \cdots & \chi_{1N} \\ \chi_{21} & \chi_{22} & \cdots & \chi_{2N} \\ \vdots & \vdots & \ddots & \vdots \\ \chi_{N1} & \chi_{N1} & \cdots & \chi_{NN} \end{pmatrix} \cdot \left\{ \begin{pmatrix} A_1(s)\, I_0\left(r\sqrt{\lambda_1}\right) \\ \vdots \\ A_N(s)\, I_0\left(r\sqrt{\lambda_N}\right) \end{pmatrix} + \begin{pmatrix} B_1(s)\, K_0\left(r\sqrt{\lambda_1}\right) \\ \vdots \\ B_N(s)\, K_0\left(r\sqrt{\lambda_N}\right) \end{pmatrix} \right\} + \begin{pmatrix} \psi_1 \\ \vdots \\ \psi_N \end{pmatrix} \tilde{f}_1 \tag{D-1}$$

where the Sturm-Liouville functions $\mathcal{F}_1, \mathcal{F}_2$ are substituted with modified Bessel functions of 1st and 2nd kind, in accord with the axisymmetric geometry of the solution domain. Solution for the no-flow boundary condition at the outer boundary $r_o{}^* = \frac{r_o}{r_i}$ gives:

$$A_i = B_i \frac{K_1\left(r_0\sqrt{\lambda_i}\right)}{I_1\left(r_0\sqrt{\lambda_i}\right)} \tag{D-2}$$

Where the asterisk associated with dimensionless variable is dropped for simplicity in notation. Further, If the bottomhole wellbore pressure is assumed to be p_w, $(N-1)$ boundary conditions $p_i(1,t) = p_j(1,t) = p_w(t)$, stand for equal pore pressure of distinct porosity networks at the wellbore. These boundary conditions determine B_i as:

$$B_i = \frac{\tilde{p}_w \mathrm{Det}[\mathbf{X}_{1,i}] - \tilde{f}_1 \mathrm{Det}[\mathbf{X}_{\psi,i}]}{\mathrm{Det}[\mathbf{X}] \cdot \mathrm{g}\left(1{:}\sqrt{\lambda_i}\right)} \tag{D-3}$$

where function $\mathrm{g}\left(r{:}\sqrt{\lambda_i}\right)$ is defined as:

$$\mathrm{g}\left(r{:}\sqrt{\lambda_i}\right) = \frac{K_1\left(r_0\sqrt{\lambda_i}\right)}{I_1\left(r_0\sqrt{\lambda_i}\right)} I_0\left(r\sqrt{\lambda_i}\right) + K_0\left(r\sqrt{\lambda_i}\right) \tag{D-4}$$

Det in Equation (D-3) denotes the determinant of a matrix whose elements are eigen-vectors $\boldsymbol{\chi}_i$. $\mathbf{X}_{\psi,i}, \mathbf{X}_{1,i}$ is defined by replacing the i^{th} column of the eigenvectors matrix $\mathbf{X} = \left[\boldsymbol{\chi}_\mathbf{1}^\mathbf{T}, \boldsymbol{\chi}_\mathbf{2}^\mathbf{T}, \dots, \boldsymbol{\chi}_\mathbf{N}^\mathbf{T}\right]$ with $\boldsymbol{\Psi}$ and $[1, \dots, 1]^{\mathrm{T}}$, respectively. Substituting back into Equation (3-15) gives:

$$\tilde{p}_i(r) = \tilde{f}_1 \left\{ \psi_i - \frac{1}{\mathrm{Det}[\mathbf{X}]} \sum_{j=1}^{N} \frac{\chi_{ij} \mathrm{Det}[\mathbf{X}_{\psi,j}]\, \mathrm{g}\left(r : \sqrt{\lambda_j}\right)}{\mathrm{g}\left(1 : \sqrt{\lambda_j}\right)} \right\} + \frac{\tilde{p}_w}{\mathrm{Det}[\mathbf{X}]} \sum_{j=1}^{N} \frac{\chi_{ij} \mathrm{Det}[\mathbf{X}_{1,j}]\, \mathrm{g}\left(r : \sqrt{\lambda_j}\right)}{\mathrm{g}\left(1 : \sqrt{\lambda_j}\right)} \tag{D-5}$$

However, $\tilde{p}_w$ can be found from the flow BC at the wellbore, i.e.:

$$\sum_{i=1}^{N} \kappa_i \cdot \left. \frac{\partial p_i}{\partial r} \right|_{r=1} = Q^* \tag{D-6}$$

$Q^* = \frac{Q}{Q_0}$ is the dimensionless flow rate at the wellbore, where $Q_0 = \frac{2V_w}{t_0}$ in which $V_w = \pi {r_w}^2 h$ is the wellbore volume. Substitution of Equation (D-6) into Equation (D-5) gives:

$$\tilde{p}_w = \frac{Q^* \,\mathrm{Det}[\mathbf{X}] + \tilde{f}_1 \cdot \sum_{j=1}^{N} \frac{\eta_j \mathrm{Det}[\mathbf{X}_{\psi,j}]\, \mathrm{g}'\left(1 : \sqrt{\lambda_j}\right)}{\mathrm{g}\left(1 : \sqrt{\lambda_j}\right)}}{\sum_{j=1}^{N} \frac{\eta_j \mathrm{Det}[\mathbf{X}_{1,j}]\, \mathrm{g}'\left(1 : \sqrt{\lambda_j}\right)}{\mathrm{g}\left(1 : \sqrt{\lambda_j}\right)}} \tag{D-7}$$

where $\eta_j = \sum_{i=1}^{N} \chi_{ij} \kappa_i$. Substitution of Equation (D-7) into Equation (D-5) determines general expression for the pressures $\tilde{p}_i$ as:

$$\tilde{p}_i(r)$$

$$= \tilde{f}_1 \left\{ \psi_i \right.$$

$$+ \frac{1}{\mathrm{Det}[\mathbf{X}]} \left\{ \left\{ \frac{\sum_{j=1}^{N} \frac{\eta_j \mathrm{Det}[\mathbf{X}_{\psi,j}]\, \mathrm{g}'\left(1:\sqrt{\lambda_j}\right)}{\mathrm{g}\left(1:\sqrt{\lambda_j}\right)}}{\sum_{j=1}^{N} \frac{\eta_j \mathrm{Det}[\mathbf{X}_{1,j}]\, \mathrm{g}'\left(1:\sqrt{\lambda_j}\right)}{\mathrm{g}\left(1:\sqrt{\lambda_j}\right)}} \right\} \sum_{j=1}^{N} \frac{\chi_{ij} \mathrm{Det}[\mathbf{X}_{1,j}]\, \mathrm{g}\left(r:\sqrt{\lambda_j}\right)}{\mathrm{g}\left(1:\sqrt{\lambda_j}\right)} \right. \quad \text{(D-8)}$$

$$\left. - \sum_{j=1}^{N} \frac{\chi_{ij} \mathrm{Det}[\mathbf{X}_{\psi,j}]\, \mathrm{g}\left(r:\sqrt{\lambda_j}\right)}{\mathrm{g}\left(1:\sqrt{\lambda_j}\right)} \right\} + \frac{Q^* \sum_{j=1}^{N} \frac{\chi_{ij} \mathrm{Det}[\mathbf{X}_{1,j}]\, \mathrm{g}\left(r:\sqrt{\lambda_j}\right)}{\mathrm{g}\left(1:\sqrt{\lambda_j}\right)}}{\sum_{j=1}^{N} \frac{\eta_j \mathrm{Det}[\mathbf{X}_{1,j}]\, \mathrm{g}'\left(1:\sqrt{\lambda_j}\right)}{\mathrm{g}\left(1:\sqrt{\lambda_j}\right)}}$$

The problem of interest in this Appendix has thus far reduced to finding the arbitrary function $\tilde{f}_1$. For this purpose, We may proceed with the kinematics of displacement in cylindrical coordinates:

$$\tilde{u}_r = \frac{1}{r} \int \tilde{\varepsilon} r dr - \frac{\tilde{\varepsilon}_{zz} r}{2} + \frac{\tilde{f}_2}{r} \quad \text{(D-9)}$$

where $\tilde{f}_2$ is a new arbitrary function of integration. Substitution form Equation (3-2), along with the conditions of fixed displacement at the wellbore casing yields:

$$\tilde{u}_r = \frac{1}{r} \int_1^r \frac{c_{mi} \tilde{p}_i(x)}{\sum_{i=1}^{N} S_i} x dx + \left(\tilde{f}_1 - \tilde{\varepsilon}_{zz}\right) \frac{(r-1)}{2} \quad \text{(D-10)}$$

Further, the condition of fixed displacement at the outer boundary of reservoir yields:

$$\tilde{\varepsilon}_{zz} = \tilde{f}_1 + \frac{2}{r_o(r_o-1)} \int_1^{r_o} \frac{c_{mi} \tilde{p}_i(x)}{\sum_{i=1}^{N} S_i} x dx \quad \text{(D-11)}$$

Lastly, the assumption of constant average normal stress at the top surface of reservoir can provide us with an explicit formula for the arbitrary function $\tilde{f}_1$ as follows:

$$\tilde{f}_1 = \frac{-2}{r_0({r_o}^2 - 1)}\left(\frac{1-\nu}{1-2\nu}\right)^2 \int_1^{r_o} \alpha_i \tilde{p}_i(x) x dx \tag{D-12}$$

Solution of Equation (D-12) for $\tilde{f}_1$ after substitution from Equation (D-8) yields:

$$\tilde{f}_1 = Q^* \frac{\left(\frac{\sum_{j=1}^{N} \frac{\beta_j \mathrm{Det}[\mathbf{X}_{1,j}]\, \bar{\mathrm{g}}\left(\sqrt{\lambda_j}\right)}{\mathrm{g}\left(1:\sqrt{\lambda_j}\right)}}{\sum_{j=1}^{N} \frac{\eta_j \mathrm{Det}[\mathbf{X}_{1,j}]\, \mathrm{g}'\left(1:\sqrt{\lambda_j}\right)}{\mathrm{g}\left(1:\sqrt{\lambda_j}\right)}}\right) \frac{-2}{r_0({r_o}^2 - 1)}\left(\frac{1-\nu}{1-2\nu}\right)^2}{1 + \psi \frac{1}{r_0}\left(\frac{1-\nu}{1-2\nu}\right)^2 + \frac{-2}{r_0({r_o}^2 - 1)}\left(\frac{1-\nu}{1-2\nu}\right)^2 \Theta} \tag{D-13}$$

Where the parameter Θ is defined as:

$$\Theta = \left[\frac{\sum_{j=1}^{N} \frac{\eta_j \mathrm{Det}[\mathbf{X}_{\psi,j}]\, \mathrm{g}'\left(1:\sqrt{\lambda_j}\right)}{\mathrm{g}\left(1:\sqrt{\lambda_j}\right)}}{\sum_{j=1}^{N} \frac{\eta_j \mathrm{Det}[\mathbf{X}_{1,j}]\, \mathrm{g}'\left(1:\sqrt{\lambda_j}\right)}{\mathrm{g}\left(1:\sqrt{\lambda_j}\right)}}\right] \sum_{j=1}^{N} \frac{\beta_j \mathrm{Det}[\mathbf{X}_{1,j}]\, \bar{\mathrm{g}}\left(\sqrt{\lambda_j}\right)}{\mathrm{g}\left(1:\sqrt{\lambda_j}\right)} - \sum_{j=1}^{N} \frac{\beta_j \mathrm{Det}[\mathbf{X}_{\psi,j}]\, \bar{\mathrm{g}}\left(\sqrt{\lambda_j}\right)}{\mathrm{g}\left(1:\sqrt{\lambda_j}\right)} \tag{D-14}$$

Where the function $\bar{\mathrm{g}}\left(\sqrt{\lambda_j}\right)$ and parameters ψ and β_j are defined as:

$$\bar{\mathrm{g}}\left(\sqrt{\lambda_j}\right) = \int_1^{r_o} \mathrm{g}\left(x:\sqrt{\lambda_j}\right) x dx \tag{D-15}$$

$$\psi = \sum_{i=1}^{N} \alpha_i \psi_i \tag{D-16}$$

$$\beta_j = \sum_{i=1}^{N} \alpha_i \chi_{ij} \tag{D-17}$$

Equation (D-13) brings the problem of multi-porosity/multi-permeability poroelastic hollow cylinder into closure.